

Visualisierung der intrazellulären Aufnahme und des
Metabolismus von Lipiden und Lipoproteinen
mittels Raman-Spektroskopie



seit 1558

Dissertation (kumulativ)

zur Erlangung des akademischen Grades
doctor rerum naturalium (Dr. rer. nat.)

vorgelegt dem Rat der Chemisch-Geowissenschaftlichen Fakultät
der Friedrich-Schiller-Universität Jena von

Master of Science (M.Sc.) Clara Cornelia Stiebing,
geboren am 11.08.1987 in Frankfurt am Main

Gutachter:

1. Prof. Dr. Jürgen Popp
Institut für Physikalische Chemie, Friedrich-Schiller-Universität Jena
2. Prof. Dr. Stefan Lorkowski
Institut für Ernährungswissenschaften, Friedrich-Schiller-Universität Jena

Tag der öffentlichen Verteidigung: 19. April 2017

Inhaltsverzeichnis

| | |
|--|-----|
| Abkürzungsverzeichnis | ii |
| Abbildungsverzeichnis | iii |
| 1 Einleitung | 5 |
| 1.1 Motivation – Atherosklerose und die Rolle von Lipiden | 5 |
| 1.2 Stand der Technik – Lipide und Einzelzellanalyse | 9 |
| 1.3 Raman-Spektroskopie | 12 |
| 1.3.1 Spontane und kohärente Raman-Streuung | 12 |
| 1.3.2 Raman-Spektroskopie an Einzelzellen | 16 |
| 1.4 Zielsetzung der Dissertation | 19 |
| 2 Eigene Forschungsergebnisse | 20 |
| 2.1 Aufnahme und Metabolisierung von deuterierter Arachidonsäure durch Makrophagen | 20 |
| 2.2 Untersuchung von lebenden Makrophagen während der Inkubation mit deuterierter Palmitinsäure | 25 |
| 2.3 Aufnahme von deuteriertem Tripalmitin durch Makrophagen über den Lipoproteintransportweg | 30 |
| 3 Zusammenfassung | 35 |
| 4 Summary | 40 |
| 5 Literaturverzeichnis | 44 |
| 6 Publikationen | 51 |
| 6.1 Complexity of fatty acid distribution inside human macrophages on single cell level using Raman micro-spectroscopy [CS1] | 52 |
| 6.2 Real-time Raman and SRS imaging of living human macrophages reveals cell-to-cell heterogeneity and dynamics of lipid uptake [CS2] | 66 |
| 6.3 Raman spectroscopic imaging of human macrophages incubated with triglyceride-enriched oxLDL visualizes translocation of lipids between endocytic vesicles and lipid droplets [CS3] | 77 |
| 6.4 Advantages and limitations of Raman spectroscopy for molecular diagnostics: an update [CS4] | 86 |
| 7 Konferenzbeiträge | 102 |
| Danksagung | 105 |
| Erklärungen | 107 |

Abkürzungsverzeichnis

| | |
|-------|---|
| asLS | asymmetrische Methode der kleinsten Quadrate (engl. <i>asymmetric least squares fitting</i>) |
| ATR | abgeschwächte Totalreflexion (engl. <i>attenuated total reflection</i>) |
| CARS | kohärente Anti-Stokes-Raman-Streuung (engl. <i>coherent anti-Stokes Raman scattering</i>) |
| CCD | ladungsgekoppeltes Bauteil (engl. <i>charge-coupled device</i>) |
| CRS | kohärente Raman-Streuung (engl. <i>coherent Raman scattering</i>) |
| d-TP | Tri(palmitin-d ₃₁) |
| ER | endoplasmatisches Retikulum |
| FLIM | Fluoreszenzlebensdauer-Mikroskopie (engl. <i>fluorescence lifetime imaging microscopy</i>) |
| GC | Gaschromatographie |
| HDL | Lipoprotein hoher Dichte (engl. <i>high-density lipoprotein</i>) |
| HPLC | Hochleistungsflüssigkeitschromatographie (engl. <i>high performance liquid chromatography</i>) |
| IR | Infrarot-Spektroskopie |
| IVUS | intravaskulärer Ultraschall |
| LC | Flüssigkeitschromatographie (engl. <i>liquid chromatography</i>) |
| LDL | Lipoprotein geringer Dichte (engl. <i>low-density lipoprotein</i>) |
| LDLR | LDL-Rezeptor, siehe auch LDL |
| MS | Massenspektrometrie |
| oxLDL | oxidiertes Lipoprotein geringer Dichte |
| ROS | reaktive Sauerstoffspezies (engl. <i>reactive oxygen species</i>) |
| SRS | stimulierte Raman-Streuung |
| VLDL | Lipoprotein sehr geringer Dichte (engl. <i>very-low-density lipoprotein</i>) |

Abbildungsverzeichnis

| | | |
|--------------|---|----|
| Abbildung 1 | Zelluläre Aufnahmewege von Fettsäuren..... | 7 |
| Abbildung 2 | Elastische Rayleigh-Streuung und inelastische Raman-Streuung im Jablonski-Diagramm..... | 12 |
| Abbildung 3 | Kohärente Raman-Streuung im Vergleich zur spontanen Raman-Streuung im Jablonski-Diagramm..... | 14 |
| Abbildung 4 | Beispielspektren der Hauptbestandteile einer Zelle | 16 |
| Abbildung 5 | Übersicht der Forschungsprojekte | 19 |
| Abbildung 6 | Quantifizierung der Aufnahme von Arachidonsäure über die Zeit | 23 |
| Abbildung 7 | Ko-Inkubationsstudie mit zwei Fettsäuretypen | 24 |
| Abbildung 8 | Lebendzellversuche mit Raman-Mikrospektroskopie..... | 27 |
| Abbildung 9 | Lebendzellversuche mit SRS..... | 29 |
| Abbildung 10 | Vergleich von oxLDL und β -Carotin | 31 |
| Abbildung 11 | Zeitliche Übersicht von endozytotischen Vesikeln und Lipidtropfen | 33 |

1 Einleitung

1.1 Motivation – Atherosklerose und die Rolle von Lipiden

Kardiovaskuläre Erkrankungen sind die häufigsten, natürlichen Todesursachen auf der Welt (1). Zu den Risikofaktoren zählen verhaltensbezogene Faktoren, wie zu wenig Bewegung, ungesunde Ernährung sowie Alkohol- und Tabakkonsum. Der Krankheitsprozess entwickelt sich oft schleichend über Jahrzehnte ohne Symptome und wirkt sich erst im höheren Alter aus, im schlimmsten Fall in Form von Herzinfarkt oder Schlaganfall. Durch Veränderungen im Lebensstil können Risiken erfolgreich minimiert und das Fortschreiten der Krankheit verhindert werden. Eine Früherkennung, zu einem Zeitpunkt an dem sich noch keine Symptome äußern, kann die Prognose und Therapie der Patienten deutlich verbessern (2). Über drei Viertel der Todesfälle kommen in Ländern mit mittlerem bis geringem Einkommen vor, da der Zugang zu Gesundheitssystemen zur Früherkennung fehlt. Ein nicht zu vernachlässigender Faktor ist die alternde Gesellschaft, wodurch mehr Fälle akut werden und auch die finanzielle Belastung für das Gesundheitssystem steigt.

Die Atherosklerose ist die prominenteste unter den kardiovaskulären Erkrankung und zählt zu den Hauptursachen für Schlaganfälle und Herzinfarkte (3). Atherosklerotische Ablagerungen innerhalb der Arterienwände können zur Reduzierung des Blutflusses oder zum kompletten Verschluss des Blutgefäßes führen. Der Prozess beginnt durch Fehlfunktionen des Endothels, wodurch sich die Permeabilität der Arterieninnenwand für Zellen und andere Partikel erhöht. Unter anderem werden Monozyten aus der Blutbahn durch Botenstoffe angelockt, die aufgrund einer Verletzung oder Dysfunktion des Endothels ausgesandt werden (4). Im subendothelialen Bereich der Arterienwand differenzieren sie zu adhärenen Makrophagen, welche eine wichtige Rolle in der unspezifischen Immunabwehr des Körpers spielen. Durch Phagozytose nehmen Makrophagen neben Bakterien auch Lipide in Form von Lipoproteinen und Reste abgestorbener Zellen auf. Die Lipide werden in der Zelle verstoffwechselt oder im Zytoplasma als Lipidtropfen gespeichert. Lipidtropfen sind wichtige zelluläre Organellen, über deren Rolle vieles unbekannt ist. Die Hypothese zur Entstehung der Tropfen am endoplasmatischen Retikulum (ER) ist mittlerweile etabliert, die genaue Bildung und das Wachstum ist aber nach wie vor unklar (5).

Es wird angenommen, dass das Fortschreiten der Atherosklerose durch hohe Lipidspiegel im Blutstrom gefördert wird, da bei Überangebot unverhältnismäßig viele Lipidtropfen in Makrophagen gebildet werden. Makrophagen transformieren zu Schaumzellen, wenn das Zytoplasma vollständig mit Lipidtropfen gefüllt ist. Letztendlich führt dies zum Zelltod und die freigesetzten Zellbestandteile können lipidhaltige Plaqueablagerungen im subendothelialen Bereich der Arterienwände bilden. Die Schaumzellbildung von Makrophagen gilt daher als ein frühes Merkmal der Atherosklerose.

Da Lipide hydrophob sind, bedarf es besonderer Transportwege, um diese in der Blutbahn zu transportieren. Lipoproteine sind die Hauptträger von Lipiden im Blutstrom. Sie bestehen aus einer Phospholipidmembran mit eingebetteten Proteinen und einem lipidhaltigen Kern bestehend aus Triglyceriden, Cholesterolestern und Cholesterol. Basierend auf dem Protein- und Lipidanteil werden Lipoproteine aufgrund ihrer Dichte klassifiziert. Lipoproteine sehr geringer Dichte (VLDL, engl. *very-low-density lipoprotein*) werden in der Leber produziert, in die Blutbahn abgegeben und können über Lipasen zu Lipoproteinen geringer Dichte (LDL, engl. *low-density lipoprotein*) umgewandelt werden. Letztere werden vornehmlich durch rezeptorvermittelte Endozytose im Gewebe von Zellen, wie zum Beispiel Makrophagen, aufgenommen und verstoffwechselt. Überschüssiges Cholesterin kann über Lipoproteine hoher Dichte (HDL, engl. *high-density lipoprotein*) wiederum aus den Zellen zurück in die Leber transportiert werden (3). Im Falle einer endothelialen Dysfunktion der Arterienwand kann LDL leicht in den subendothelialen Bereich eindringen und dort durch extrazelluläre Proteine und reaktive Sauerstoffspezies (ROS, engl. *reactive oxygen species*) oxidiert oder enzymatisch modifiziert werden (4). Durch die Modifikation des LDL wird der rezeptorabhängige Aufnahmeweg in Makrophagen verändert. Anstatt an den LDL-Rezeptor (LDLR), bindet oxidiertes LDL (oxLDL) an *scavenger*-Rezeptoren, wie zum Beispiel LOX-1 und CD36 (6). Die Aufnahme erfolgt im Gegensatz zum Aufnahmeweg des nativen LDL über den LDLR unkontrolliert und ohne zellulären Rückkopplungsmechanismus, der Aufnahme und Efflux gleichmäßig steuert. Bei einem Überangebot von oxLDL nehmen Makrophagen somit zunehmend mehr auf, bis letztlich toxische Lipidwerte erreicht werden. Das Zusammenspiel zwischen Makrophagen und oxLDL ist daher ein bedeutender Schritt bei der Entstehung der Atherosklerose.

Neben dem Lipoproteintransportweg können Lipiden auch über Strukturproteine wie Albumin im Blut transportiert werden. Beide Transportwege sind schematisch in Abbildung 1 aufgeführt. Freie Fettsäuren werden an Albumin, das am häufigsten vorkommende Protein im Blut, gebunden. In unmittelbarer Nähe zur Zellmembran wird die Fettsäure freigesetzt und kann durch Transmembranproteine, wie zum Beispiel CD36 und FATPs, oder direkt durch die Lipidmembran in die Zelle gelangen (7). Dort steht die Fettsäure zur Metabolisierung und Speicherung zur Verfügung. Der Transport über LDL ist dagegen, wie oben beschrieben aufgrund der endozytotischen Aufnahme deutlich komplexer. Bindet LDL beziehungsweise oxLDL an einen passenden Rezeptor, werden die Partikel über Abschnürungen in der Zellmembran eingeschlossen und in den entstehenden intrazellulären Vesikeln zersetzt. Letztendlich wird der lipidhaltige Inhalt freigegeben, wobei es sich in der Regel nicht um freie Fettsäuren sondern um Triglyceride oder Cholesterolester handelt. Erst wenn das endozytotische Vesikel abgebaut wurde, können die Lipide in Lipidtropfen abgespeichert werden. Dabei werden die Triglyceride gespalten und während der Inkorporation in die Lipidtropfen neu verestert. Auch unabhängig von Rezeptoren kann LDL, insbesondere aggregierte LDL-Partikel, endozytotisch aufgenommen werden (4). Lipoproteinlipasen, die von Makrophagen exprimiert werden, können ebenfalls eine endozytotische Aufnahme auslösen indem sie eine Verbindung zwischen LDL und Proteoglykanen auf der Zellmembran herstellen (8). Der Mechanismus über die Bildung von endozytotischen Vesikeln bleibt dabei bei allen Aufnahmevarianten bestehen.

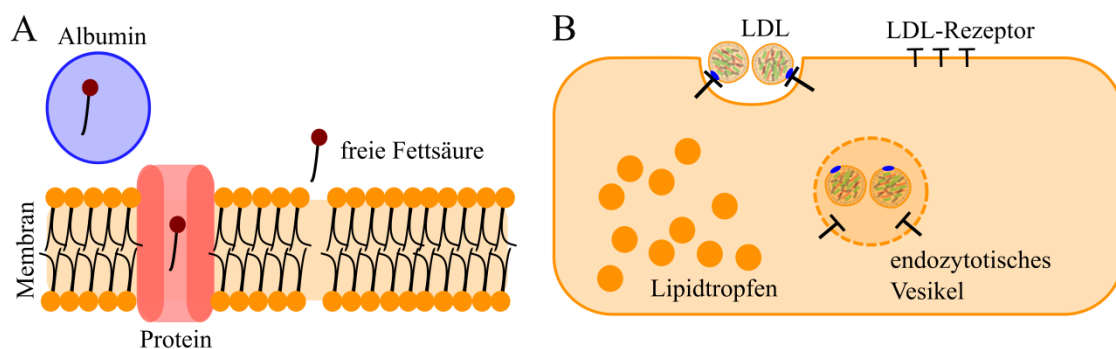


Abbildung 1 Zelluläre Aufnahmewege von Fettsäuren

Schematische Darstellung der (A) Aufnahme von freien Fettsäuren durch Albumin und (B) rezeptorvermittelten Aufnahme von Triglyceriden durch LDL.

Nahezu alle Menschen entwickeln Plaqueablagerungen in den kleinen und mittelgroßen Arterien, allerdings bleiben viele dieser Ablagerungen ungefährlich und brauchen keine klinische Behandlung. Plaques werden gefährlich, wenn sie instabil sind und aufbrechen können, was stark von deren Lipidzusammensetzung abhängt. Da der Lipidmetabolismus von Makrophagen maßgeblich dafür entscheidend ist, muss dieser besser verstanden werden. Ist bekannt, wie einzelne Lipide zu instabilen Plaques führen und welche molekularen Prozesse in der Zelle dazu beitragen, kann die Therapie und Medikation verbessert werden.

In der vorliegenden Arbeit werden Forschungsergebnisse über die Aufnahme und anschließende Metabolisierung von Lipiden in Makrophagen vorgestellt. Die Interaktion zwischen Lipiden und Makrophagen erhält aufgrund ihrer Schlüsselrolle in der Entstehung der Atherosklerose eine hohe Aufmerksamkeit in der Lipidforschung. In den folgenden Abschnitten wird auf den derzeitigen Stand der Technik mit Blick auf Bildgebungsverfahren für Einzelzellmessungen eingegangen. Weiterhin wird eine Einführung in die Raman-Spektroskopie gegeben, die in der vorliegenden Dissertation maßgeblich als Messmethode verwendet wurde.

1.2 Stand der Technik – Lipide und Einzelzellanalyse

Es gibt eine Vielzahl unterschiedlicher optischer und biochemischer Methoden, um biologische Proben hinsichtlich ihrer Lipidzusammensetzung zu untersuchen. In den derzeitigen Standardmethoden steht die Gewinnung von chemischen Lipidinformationen in Konkurrenz mit der orts aufgelösten Darstellung von Lipidkomponenten, besonders auf Einzelzellebene.

Enzymatische Methoden ermöglichen es indirekt die Gesamtkonzentration von Lipiden, wie zum Beispiel das Gesamtcholesterol im Blutplasma, über photometrische Messungen zu bestimmen (9). Um spezifische Informationen über die Lipidzusammensetzung einer Probe zu erhalten, werden standardmäßig chromatographische Verfahren, unterschiedlichste Varianten der Massenspektrometrie sowie deren Kombination angewendet (10, 11). Beide besitzen ein großes Potential das gesamte Lipidprofil von biologischen Proben wie Gewebe, Blut oder Zellen zu untersuchen, bieten aber in der Regel keine orts aufgelöste Darstellung. Zellstudien basieren auf Bulkmessungen kultivierter Zellpopulationen, aus denen die Lipide vorher extrahiert werden müssen. Chromatographie ist ein Verfahren zur Trennung von Probengemischen, welches auf physikalisch-chemischer Wechselwirkung der Probe mit definierten Trägersubstanzen beruht. Die zwei meist verwendeten Methoden in der Lipidforschung sind die Gas- (GC) und Flüssigkeits- (LC, engl. *liquid chromatography*) beziehungsweise Hochleistungsflüssigkeitschromatographie (HPLC, engl. *high performance liquid chromatography*). Eine große Bandbreite unterschiedlicher Anwendungen ist vorhanden, die je nach Fragestellung kleinste Unterschiede in der Struktur von Lipiden feststellen können. So kann die Oxidation, Elongation oder Desaturierung von bestimmten Fettsäuren nachverfolgt werden (12, 13). Massenspektrometrie (MS) trennt Ionen nach ihrer Masse. Dazu muss das zuvor extrahierte Lipidgemisch ionisiert und in die Gasphase überführt werden. Durch ein elektrisches Feld werden die Ionen unterschiedlich schnell beschleunigt und nach ihrem Masse-zu-Ladung-Verhältnis aufgetrennt. Die Triglyceridzusammensetzung von einzelnen Lipidtropfen wurde mithilfe von MS untersucht, wofür aber die vorherige Isolation der Tropfen aus Zellen notwendig war (14).

Häufig werden beide Methoden miteinander verbunden, um eine noch genauere Auftrennung der Lipide zu erreichen. LC-MS und GC-MS sind gängige multimodale Methoden geworden (15, 16). Da die zu untersuchende Substanz aus den biologischen Proben extrahiert werden muss, ist meist eine teils komplexe Probenpräparation notwendig. Außerdem sind Chromatographien und gewöhnliche MS auf Bulkmessungen angewiesen und für Einzelzellstudien nicht anwendbar. Durch die Entwicklung von MS-Bildgebungsverfahren können Gewebeschnitte orts aufgelöst untersucht werden. Einzelzellmessungen sind aber durch die Konzentrationsverteilung der Zielmoleküle und die räumliche Auflösung beschränkt (17, 18).

Eine für Einzelzellmessungen geeignete Methode ist die Fluoreszenzmikroskopie. Dabei wird nach Anregung mit monochromatischem Licht, die Autofluoreszenz von endogenen Fluorophoren wie Kollagen oder von externen Fluorophoren, die zur Markierung bestimmter Zellkomponenten in die Probe eingebracht wurden, detektiert (19). Es gibt nur wenige lipidaffine Marker wie BODIPY oder Nile Red, die es ermöglichen, Lipidtropfen in den Zellen zu visualisieren (20-23). Die Fluorophore sind allerdings meist nicht spezifisch für unterschiedliche Lipide, wie zum Beispiel Fettsäuretypen, und binden unspezifisch an die insgesamt vorhandenen neutralen Lipide in einer Zelle. Somit ist eine Aufschlüsselung der Lipidzusammensetzung von Organellstrukturen nicht möglich. Es gibt eine Reihe von unterschiedlichen, bildgebenden Fluoreszenzmethoden, die sich hauptsächlich in der erreichbaren räumlichen Auflösung unterscheiden (24, 25). Die Fluoreszenzlebensdauer-Mikroskopie (FLIM, engl. *fluorescence lifetime imaging microscopy*) misst die Lebensdauer einer bestimmten Autofluoreszenz nach Anregung teils mehrerer endogener Fluorophore in einer Probe. Vorteilhaft ist, dass keine externen Marker in das System eingebracht werden müssen. Die Methode eignet sich besonders für Gewebemessungen. Durch Implementierung in endoskopische Messgeräte, können atherosklerotische Plaques *in vivo* gemessen werden (26, 27). In Kombination mit Techniken wie intravaskulärer Ultraschall (IVUS), die eine strukturelle Information der Plaques bereitstellen, kann ein Einblick in das Innere von Arterien gegeben werden (28, 29).

Schwingungsspektroskopische Methoden in Kombination mit moderner Mikroskopie und anderen optischen bildgebenden Verfahren besitzen großes Potential, die Lücke zwischen

Ortsauflösung und chemischer Analytik zu schließen. Durch spezifische Banden, die auf der Schwingung von Molekülbindungen basieren, können Rückschlüsse über die in der Probe vorhandenen Moleküle gezogen werden. Gleichzeitig kann durch die Kopplung mit einem Mikroskop eine Bildgebung gewährleistet werden, deren Auflösung durch das Abbe-Limit beschränkt wird. Die Infrarot-Spektroskopie (IR) basiert auf der Absorption von infrarotem Licht durch Moleküle. Sie ist eine weitverbreitete Methode zur Strukturklärung unbekannter Substanzen oder zur quantitativen Analytik basierend auf dem Lambert-Beer-Gesetz. Pathologische Biopsien von atherosklerotischen Plaques konnten mithilfe von IR erfolgreich charakterisiert werden (30, 31). Die Aufnahme von Fettsäuren in Krebszellen wurde untersucht (32), allerdings ist die räumliche Auflösung für Einzelzellstudien aufgrund der hohen Anregungswellenlänge stark begrenzt. Eine subzelluläre Darstellung einzelner Lipidtropfen kann nicht erreicht werden. Problematisch ist auch eine starke Wasserabsorption im infraroten Wellenlängenbereich. Durch ATR-IR (abgeschwächte Totalreflexion, engl. *attenuated total reflection*) kann die Untersuchung von Lebendzellen durch die Erzeugung von evaneszenten Wellen an der Grenzfläche zwischen Probe und Reflexionselement trotzdem ermöglicht werden (33).

Für die Untersuchung des Metabolismus von ausgewählten Lipiden in Einzelzellen mit einer subzellulären Auflösung sind die bisher erwähnten Methoden nicht anwendbar. Hier hat die Raman-Spektroskopie als weitere Methode der Schwingungsspektroskopie das größte Potential. Durch die Verwendung von Anregungswellenlängen im sichtbaren bis nahinfraroten Bereich ist sie für die Bildgebung von Zellen geeigneter als IR. Während des letzten Jahrzehnts wurde in der Lipidforschung zunehmend ein Augenmerk auf Raman-Spektroskopie gelegt, die im nächsten Kapitel näher beleuchtet wird.

1.3 Raman-Spektroskopie

1.3.1 Spontane und kohärente Raman-Streuung

Die Raman-Spektroskopie basiert auf inelastischer Streuung von monochromatischem Licht an Molekülen. Durch die Wechselwirkung elektromagnetischer Strahlung mit einem Molekül wird dessen Elektronenwolke gegenüber dem Atomkern verschoben und eine Polarisation hervorgerufen. Das induzierte elektrische Dipolmoment oszilliert mit der derselben Frequenz ω_0 wie die einfallende Strahlung und emittiert wiederum wie ein Hertzscher Dipol sekundäre Strahlung der Frequenz ω_0 . Dieser elastische Streueffekt wird Rayleigh-Streuung genannt (siehe Abbildung 2). Durch Anregung zusätzlicher Eigenschwingungen des Moleküls, wird das induzierte Dipolmoment in der Frequenz moduliert und es treten weitere Beiträge mit einer niedrigeren ($\omega_0 - \omega$, Stokes) und höheren Frequenz ($\omega_0 + \omega$, Anti-Stokes) auf (34). Dieser Effekt heißt Raman-Streuung und wurde nach dem indischen Physiker C.V. Raman benannt, welcher im Jahr 1928 die Streuung experimentell nachwies. Damit eine Molekülschwingung Raman-aktiv ist, muss sich deren Polarisierbarkeit α ändern. Dies bedeutet, dass sich die Elektronendichte gegenüber dem Gleichgewichtszustand verschieben muss (35, 36). Von Gasen können neben Molekülschwingungen auch Rotationen angeregt werden. In Abbildung 2 sind die Streueffekte im Jablonski-Diagramm beschrieben. Ein Molekül wird aus einem energetisch niedrigeren Eigenzustand in ein kurzlebige virtuelles Niveau angeregt und geht abhängig von der vorliegenden Streuung in einen finalen Eigenzustand über. Ein virtuelles Niveau ist ein nichtstationärer Zustand mit einer Lebensdauer im Bereich von Femtosekunden, der nur während der Wechselwirkung zwischen Molekül und elektromagnetischer Strahlung vorliegt.

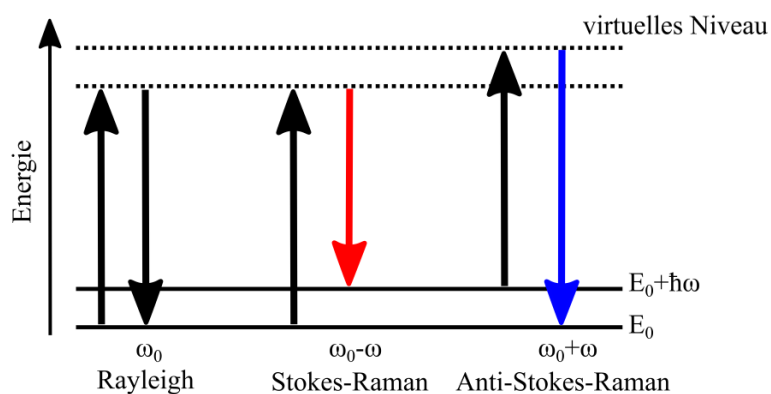


Abbildung 2 Elastische Rayleigh-Streuung und inelastische Raman-Streuung im Jablonski-Diagramm

Als Lichtquelle werden schmalbandige Laser eingesetzt, deren Wellenlängen üblicherweise im sichtbaren bis nahinfraroten Bereich liegen. Für die Aufspaltung und Detektion des gestreuten Lichts wird meist ein dispersiver Aufbau mit einer CCD-Kamera (ladungsgespeistes Bauteil, engl. *charge-coupled device*) verwendet. Abhängig von den Messanforderungen sind unterschiedliche Modalitäten möglich. Wird die Raman-Spektroskopie in einen mikroskopischen Aufbau integriert, können neben den spektralen auch orts aufgelöste chemische Informationen erhalten werden. Diese Anwendung wird Raman-Mikrospektroskopie genannt. Raman-Bilder werden aufgenommen, in dem ein Anregungslaser die Probe zwei- oder dreidimensional abtastet. Jeder Bildpunkt entspricht demnach einem Spektrum. Durch die geeignete Auswahl einer Schwingungsbande kann über deren räumliches Intensitätsprofil eine Abbildung rekonstruiert werden.

Die Raman-Spektroskopie bietet durch die Schwingungsanregung von chemischen Bindungen Spektren mit einer sehr spezifischen Bandenstruktur. Die Intensität der Banden hängt von folgenden Faktoren ab:

$$I_{Stokes} \propto N * \left(\frac{\partial \alpha}{\partial q} \right)_{q_0}^2 * (\omega_0 - \omega)^4 * I_0$$

| | |
|--------------------------------------|---|
| mit N | Anzahl streuender Moleküle |
| $\frac{\partial \alpha}{\partial q}$ | Änderung der Polarisierbarkeit entlang der Normalkoordinate |
| ω_0 | Frequenz der eingestrahnten Photonen |
| ω | Frequenz der Molekülschwingung |
| I_0 | Intensität der eingestrahnten Photonen |

Je mehr Moleküle sich im Laserfokus befinden und je höher die Intensität der eingestrahnten Photonen ist, desto intensiver ist die Schwingungsbande (hier für die Stokes-Raman-Streuung dargestellt). Gleichzeitig steigt die Intensität der Banden proportional zur vierten Potenz der Frequenzen. Demnach führt eine höhere Anregungswellenlänge im nahinfraroten Bereich zu einem deutlich geringeren Signal. Allerdings ist auch die Energieübertragung auf die Probe reduziert, was wiederum die Wahrscheinlichkeit von phototoxischen Reaktionen der Probe verringert.

Der oben beschriebene spontane Raman-Effekt ist typischerweise ein schwacher Prozess, bei dem abhängig vom Streuquerschnitt von 10^6 Photonen nur etwa eines inelastisch gestreut wird. Eine schnelle Bildgebung ist somit nicht immer möglich. Allerdings können zur Verstärkung des Signals nicht-lineare Effekte ausgenutzt und Aufnahmen in Videobildrate erreicht werden (37). Abbildung 3 zeigt die Übergänge der kohärenten Raman-Modalitäten (CRS, engl. *coherent Raman scattering*) der stimulierten Raman-Streuung (SRS) und kohärenten Anti-Stokes-Raman-Streuung (CARS, engl. *coherent anti-Stokes Raman scattering*) im Jablonski-Diagramm. Diese Methoden basieren auf der Synchronisation zweier gepulster Laser, deren Frequenzunterschied einem definierten Schwingungsübergang entspricht.

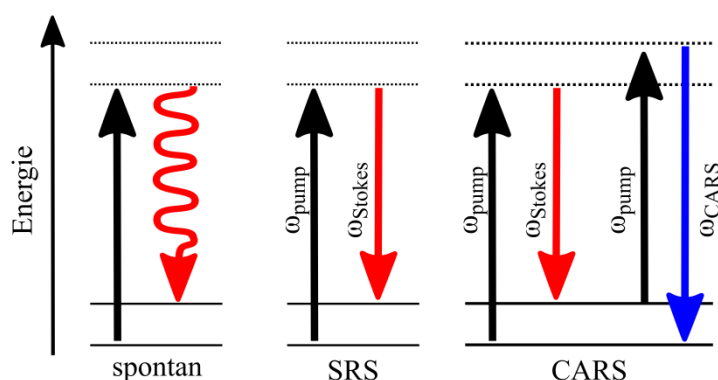


Abbildung 3 Kohärente Raman-Streuung im Vergleich zur spontanen Raman-Streuung im Jablonski-Diagramm

Stimulierte Raman-Streuung basiert auf dem gleichen Übergang wie spontane Raman-Streuung, stimuliert diesen aber durch gleichzeitige Einstrahlung von ω_{pump} und ω_{Stokes} . Dadurch erfährt die Intensität des Pump-Strahls eine Reduzierung, während der Stokes-Strahl intensiver wird (36). Eine stimulierte Streuung geschieht nur, wenn der Frequenzunterschied der Laser dem Frequenzunterschied der Molekülschwingung entspricht. Durch Modulation eines Lasers kann die Intensitätsänderung des anderen detektiert werden. Wird zum Beispiel der Stokes-Laser moduliert, wird das SRS-Signal durch den Abfall des Pump-Lasers detektiert (engl. *stimulated Raman loss*). Die Erfassung der Modulation der Laserintensität fordert einen deutlich komplexeren Messaufbau als ein gewöhnliches Raman-Mikroskop. Besonders wichtig sind ein stabiles Laser- und sensitives Detektorsystem, welches die geringfügige Änderung des intensiven Pump-Lasers detektieren kann (Figure 1 in [CS2]).

Nach der Boltzmann-Verteilung sind im thermischen Gleichgewicht nur wenige Moleküle in einem angeregten Schwingungszustand. Die Anti-Stokes-Raman-Streuung ist daher schwächer ausgeprägt als die Stokes-Raman-Streuung, welche für spontane Raman-Spektroskopie betrachtet wird. CARS verstärkt die Anti-Stokes-Frequenz ω_{CARS} , durch einen Vier-Wellen-Mischprozess, bei dem der höher angeregte Schwingungszustand besetzt wird. Durch eine weitere Anregung mit ω_{pump} zu einem höher angeregten, virtuellen Niveau wird ω_{CARS} verstärkt (36). Ein Nachteil von CARS ist die Anregung von nicht-resonantem Untergrund, der unabhängig von der Laserwellenlänge ist und zusätzlich zur eigentlichen Schwingungsanregung zum Signal beiträgt. Bei konventionellen CRS wird nur eine definierte Schwingung angeregt, wodurch keine umfangreiche spektrale Information entsteht. Es gibt allerdings eine Vielzahl von Weiterentwicklungen für die multispektrale Detektion, die in einem Übersichtsartikel zusammengefasst wurden (38). Ebenfalls wird die Instrumentierung von Raman- und CRS-Methoden diskutiert.

1.3.2 Raman-Spektroskopie an Einzelzellen

In Abbildung 4 sind beispielhaft Raman-Spektren von Lipiden und Proteinen dargestellt, welche die zwei Hauptbestandteile einer Zelle darstellen. In den Spektren wird die Intensität der Raman-Streuung gegenüber der relativen Wellenzahl aufgetragen, um vergleichbare Spektren bei unterschiedlichen Anregungswellenlängen zu erhalten. Raman-Spektren können in zwei Bereiche unterteilt werden. Der niedrige Wellenzahlbereich zwischen 600 und 1800 cm^{-1} stellt den charakteristischen Fingerabdruck der angeregten Moleküle dar. Hier ist ein eindeutiger Unterschied zwischen der Bandenstruktur von Lipiden und Proteinen zu beobachten. Charakteristische Banden in Lipidspektren sind die C=O-Streckschwingung der Carboxylgruppen von Triglyceriden bei 1741 cm^{-1} , die C=C-Streckschwingung von ungesättigten Fettsäuren bei 1656 cm^{-1} und die CH_2 -Deformationsschwingung bei 1443 cm^{-1} . In Proteinspektren ist die symmetrische Ringatmung von Phenylalanin bei 1003 cm^{-1} kennzeichnend. Weiterhin ist die Amid-I-Bande bei 1665 cm^{-1} ausgeprägt. Im hohen Wellenzahlbereich von 2800 bis 3100 cm^{-1} befinden sich CH-Streckschwingungen, deren Bande in Lipiden aufgrund der höheren Anzahl an CH-Bindungen intensiver ist als bei Proteinen. Zwischen diesen Bereichen liegt der sogenannte „stille“ Wellenzahlbereich.

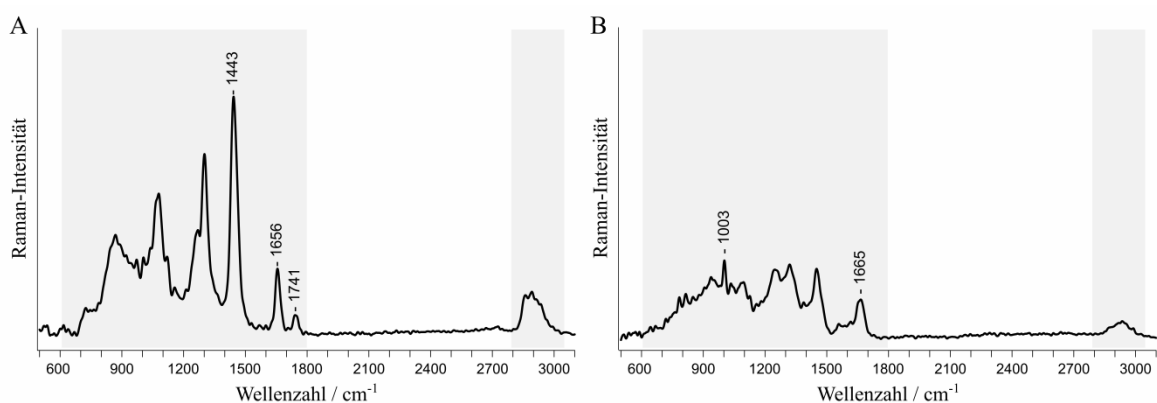


Abbildung 4 Beispielspektren der Hauptbestandteile einer Zelle

Dargestellt sind Raman-Spektren von (A) Lipiden und (B) Proteinen, die bei einer Anregungswellenlänge von 785 nm aufgenommen wurden. Die Spektren entstammen einem Raman-Bild eines Makrophagen. Der niedrige und hohe Wellenzahlbereich sowie charakteristische Schwingungsbanden sind markiert.

Obwohl eine wesentliche Stärke der Raman-Spektroskopie die Fähigkeit ist, die Verteilung von Molekülen markierungsfrei darzustellen, kann der Bildkontrast sowie molekulare

Sensitivität und Spezifität durch stabile Isotopenmarkierung weiter verbessert werden. Dies ist unter anderem bei Inkubationsstudien von Bedeutung, um eine exogen zugefügte Substanz innerhalb einer Zelle verfolgen zu können. Im Falle der in dieser Dissertation durchgeführten Arbeiten wurden deuterierte Lipide verwendet, um den Lipidmetabolismus von Makrophagen zu untersuchen. Die chemischen Eigenschaften werden durch die Deuterierung nur minimal verändert, wodurch die zellulären Eigenschaften nicht beeinträchtigt werden. Durch das im Vergleich zum Wasserstoff schwerere Deuterium entstehen Schwingungsbanden bei niedrigeren Wellenzahlen als bei undeuterten Alkylketten. CD-Schwingungen treten zwischen 2000 und 2500 cm^{-1} auf und somit im stillen Wellenzahlbereich, wo keine Banden von biologischen Proben liegen. Dadurch ist eine sehr spezifische Lokalisation innerhalb der Zellen möglich. In diesem Bereich treten neben Schwingungen deuterierter Verbindungen ebenfalls Schwingungen von Kohlenstoffdreifachbindungen oder Schwefelverbindungen auf, die auch als Marker für exogen zugefügte Substanzen verwendet werden können (39-43).

In einem im Zuge dieser Dissertation angefertigten Übersichtsartikel wurde der aktuelle Forschungsstand der Raman-Spektroskopie in der molekularen Diagnostik zusammengefasst [CS4]. Ebenfalls wird ein Einblick in die Datenverarbeitung von Raman-Spektren gegeben, die basierend auf dem spontanen Raman-Effekt aufgenommen wurden (Figure 5 in [CS4]). Neben wichtigen Schritten zur Spektrenvorbehandlung wie Basislinienkorrektur, gibt es zwei Hauptzweige der chemometrischen Auswertung von Raman-Daten. Abhängig von der Fragestellung kann zwischen unüberwachten Methoden, die nur auf den Raman-Daten basieren, und überwachten Methoden, die zusätzliche Daten wie pathologische Befunde einbinden, unterschieden werden. Um die Zusammensetzung einer Zelle zu untersuchen, eignen sich für die Auswertung von Raman-Bildern die unüberwachten, spektralen Entmischungsmethoden wie der in dieser Dissertation verwendete N-FINDR-Algorithmus (44, 45). Der N-FINDR-Algorithmus sucht nach den Spektren mit den größten Unterschieden im Datensatz und gibt diese als sogenannte Endmember aus (46), die die vorhandenen Komponenten der Probe repräsentieren. Durch lineare Kombination der Endmember kann deren Konzentrationsverteilung rekonstruiert und bildlich dargestellt werden.

Die Kombination aus chemischer Information mit örtlicher Auflösung im subzellulären Bereich stellt einen großen Gewinn der Raman-spektroskopischen Bildgebungsverfahren gegenüber den in Kapitel 1.2 vorgestellten Methoden dar. Da Lipide einen hohen Raman-Streuquerschnitt besitzen, sind sie für Raman-spektroskopische Untersuchungen gut geeignet. Hauptaugenmerk liegt auf der Zusammensetzung und Verteilung von Lipiden in Zellen und Modellorganismen wie *Caenorhabditis elegans* (47-53). Durch die hohe chemische Spezifität können Aussagen über die Sättigung und Veresterung von Fettsäuren in Lipidtropfen getroffen werden. Für mögliche *in vivo* Anwendungen zur Identifikation und Beurteilung von atherosklerotischen Plaques werden auch faserbasierte Raman-Applikationen in Kombinationen mit IVUS oder optischer Kohärenztomographie erforscht (54, 55).

1.4 Zielsetzung der Dissertation

In der vorliegenden Dissertation wurde die Raman-Spektroskopie als Messmethode eingesetzt, um den Lipidstoffwechsel von Makrophagen zu untersuchen. Die Nachverfolgung der Metabolisierung und Speicherung von Lipiden in Zellen wurde durch die Verwendung von deuterierten Lipiden ermöglicht. Die Experimente wurden so konzipiert, dass sich die experimentellen den physiologischen Bedingungen möglichst weit annäherten. Abbildung 5 stellt einen Überblick über die durchgeführten Projekte dar. Zu Beginn wurden verschiedene Fettsäuretypen ausgewählt und die Entwicklung von Schaumzellen untersucht, da diese für die frühe Entstehungsphase von Atherosklerose von besonderem Interesse sind. Um genauere Informationen zu dynamischen Prozessen zu erhalten, wurden anschließend Zellen unter Bedingungen vermessen, welche die Zellen lebend betrachten lassen. Beide Projekte basierten auf dem Albumintransport, der in der Zellkultur standardmäßig angewendet wird. Im dritten Projekt wurden stattdessen Lipoproteine mit Triglyceriden beladen und deren endozytotische Aufnahme in Makrophagen wurde untersucht. Jedes dieser Projekte führte zu einer wissenschaftlichen Publikation, welche die Grundlage für diese kumulative Dissertation bilden (siehe Kapitel 6).

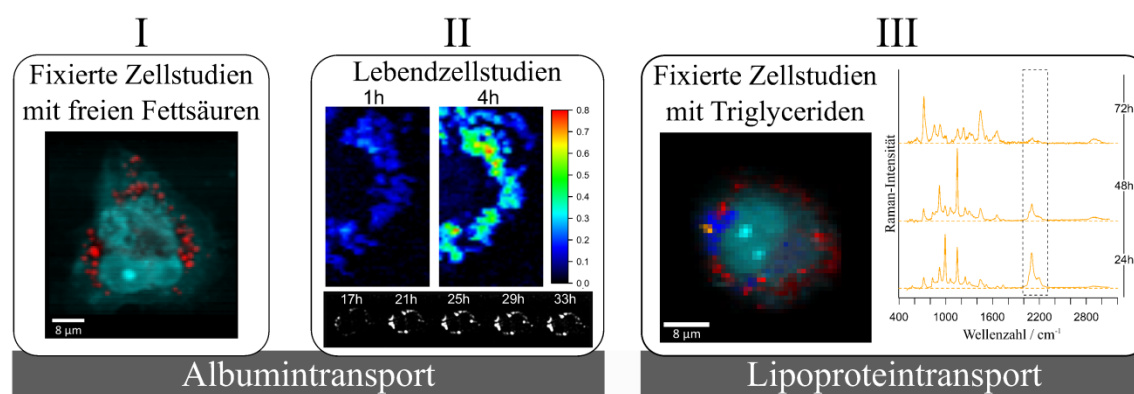


Abbildung 5 Übersicht der Forschungsprojekte

2 Eigene Forschungsergebnisse

Im Folgenden werden die Forschungsergebnisse zur Untersuchung des Lipidstoffwechsels dargestellt. Zuerst wird auf die Aufnahme von freien Fettsäuren über den Albumintransport eingegangen [CS1]. Im nachfolgenden Schritt wurden Lebzellversuche durchgeführt. Dabei wurden einzelne Zellen zeitlich verfolgt, um die Aufnahmedynamik von freien Fettsäuren zu untersuchen [CS2]. Um eine schnelle Bildgebung zu gewährleisten, wurde hier neben der Raman-Mikrospektroskopie auch SRS angewendet. Im letzten Abschnitt wird die Aufnahme von Triglyceriden durch Lipoproteine diskutiert [CS3]. Ein Zellkulturprotokoll wurde entwickelt, um deuterierte Triglyceride in oxLDL einzubringen. Anschließend wurden Makrophagen mit beladenem oxLDL inkubiert und die Verteilung des CD-Signals analysiert.

2.1 Aufnahme und Metabolisierung von deuterierter Arachidonsäure durch Makrophagen

([CS1] Stiebing et al. (2014) *Anal Bioanal Chem.* 406:7037–7046)

In diesem Projekt wurden Raman-Mikrospektroskopie und GC angewendet, um den Metabolismus von Arachidonsäure in Makrophagen zu untersuchen. Arachidonsäure ist eine mehrfach ungesättigte Fettsäure, die zu den ω -6-Fettsäuren gehört und hauptsächlich in Phospholipiden von zellulären Membranen eingebaut ist. Sie ist der Vorläufer wichtiger Signalstoffe, den Eicosanoiden, die zum Beispiel Entzündungen vermitteln oder bei der Blutgerinnung mitwirken. Daher wird die Arachidonsäure als biologisch aktiv bezeichnet (7, 56). Sie wird im Körper hauptsächlich über Linolsäure hergestellt (Figure 5 in [CS1]) oder über die Nahrung vor allem durch tierische Produkte aufgenommen (57). Eine Fragestellung dieses Projektes war, ob Arachidonsäure bei einem Überangebot auch in Lipidtropfen von Makrophagen gespeichert wird, um so der Bildung von entzündungsfördernden Eicosanoiden entgegenzuwirken (58, 59).

In Vorstudien zu dieser Arbeit wurden die Aufnahme und Metabolisierung von gesättigter Palmitinsäure untersucht (60). Nach nur 15 min war diese in Lipidtropfen nachweisbar und nach spätestens 30 h Inkubationszeit war eine deutliche Schaumzellbildung erkennbar.

Anhand einer steigenden Bandenintensität bei 1738 cm^{-1} durch die C=O-Streckschwingung der Carboxylgruppe konnte die Veresterung der Fettsäure zu Triglyceriden festgestellt werden. Palmitinsäure ist ein typisches Speicherlipid, das hauptsächlich in Lipidtropfen von Zellen gespeichert und bei Bedarf zu langkettigeren Fettsäuren verlängert wird. Ausgehend von den vorangegangenen Ergebnissen war es nun von besonderem Interesse herauszufinden, auf welche Weise eine bioaktive Fettsäure wie die Arachidonsäure in Lipidtropfen von Makrophagen abgespeichert wird und ob diese zu Schaumzellen transformieren.

Als Zellmodell wurden humane Makrophagen verwendet, die aus THP-1-Monozyten differenziert wurden. Die adhärennten Makrophagen wurden auf CaF_2 -Objektträgern kultiviert und mit $400\text{ }\mu\text{M}$ deuterierter Arachidonsäure (d_8 -Arachidonsäure) inkubiert. d_8 -Arachidonsäure wurde vorher an Albumin gebunden, damit die hydrophobe Fettsäure leicht in die Zellen gelangen kann. Nach der Inkubation wurden die Makrophagen gewaschen und mit Paraformaldehyd fixiert. Bei einer Anregungswellenlänge von 785 nm , einer Schrittweite von $0,5\text{ }\mu\text{m}$ und einer Integrationszeit von $0,5\text{ s}$ wurden Raman-Bilder von Einzelzellen bei unterschiedlichen Inkubationszeiten aufgenommen. Ein Wasser-Immersionsobjektiv ermöglichte eine Messung im wässrigen Medium, um die dreidimensionale Struktur der Zellen aufrecht zu erhalten.

Wie bereits in Kapitel 1.3.2 erläutert, liefert Deuterierung von Zielmolekülen die Möglichkeit, diese in Zellen anhand des CD-Signals zu verfolgen. d_8 -Arachidonsäure besitzt jeweils zwei Deuteriumatome an den vier Doppelbindungen, wodurch eine Schwingungsbande mit einem Maximum bei 2243 cm^{-1} entsteht (Figure 1a in [CS1]). Im niedrigen Wellenzahlbereich kann festgestellt werden, dass die C=C-Schwingungsbande bei 1633 cm^{-1} aufgrund des Deuteriums zu niedrigeren Wellenzahlen verschoben ist. Um die Zusammensetzung der Zellen auszuwerten, wurde der N-FINDR-Algorithmus angewendet (siehe Kapitel 1.3.2). Es wurden drei Komponenten extrahiert: die Lipid- und Proteinkomponente sowie die wässrige Umgebung der Zelle, die für die weitere Auswertung vernachlässigt wurde (Figure 1c in [CS1]). In der rekonstruierten Abbildung der Endmember ist die Proteinkomponente in Cyan dargestellt (Figure 1d in [CS1]). Aufgrund der höheren Proteinkonzentration im Nukleus und Nukleolus, können diese vom Zytoplasma unterschieden werden. Die in Rot dargestellte Lipidkomponente ist im

Zytoplasma der Zelle in Organellen mit einem Durchmesser zwischen 0,5 und 2 μm lokalisiert, welche die Lipidtropfen repräsentieren. Nach einer Inkubationszeit von 3 h war in den Lipidspektren von Makrophagen eine Bande bei 2248 cm^{-1} sichtbar. Die leichte Verschiebung der Bande im Vergleich zum reinen Spektrum beruht auf der unterschiedlich vorliegenden Konformation zwischen kristalliner und gelöster Form. Bei Aufnahme eines Lipidspektrums mit einem höherauflösenden Gitter konnte eine Trennung der C=C-Streckschwingung bei 1640 cm^{-1} in zwei Maxima bei 1633 und 1653 cm^{-1} festgestellt werden. Es lagen somit C=C-Doppelbindungen von nicht-deuterierten Fettsäuren und d_8 -Arachidonsäure vor. Dies bedeutet, dass d_8 -Arachidonsäure während der Speicherung in Lipidtropfen nicht oxidiert wurde. Allgemein lag eine homogene Verteilung der d_8 -Arachidonsäure innerhalb der Lipidtropfen einer Zelle vor. Auffällig ist, dass selbst nach einer Inkubation von 32 h keine signifikante Schaumzellbildung auftrat (Figure 2 in [CS1]). Über die asymmetrische Methode der kleinsten Quadrate (asLS, engl. *asymmetric least squares fitting*) wurde eine Quantifizierung des CD-Signals in Lipidtropfen erstellt. In Abbildung 6A ist zu sehen, dass eine Sättigung der Lipidtropfen mit d_8 -Arachidonsäure bereits nach 8 h eintrat.

Um eine Übersicht über die komplette Lipidzusammensetzung der Zellen zu erhalten, wurden GC-Messungen durchgeführt. Die Zellen wurden analog zu den Raman-Messungen mit nicht-deuterierter Arachidonsäure inkubiert und die Lipide der gesamten Zellpopulation wurden extrahiert. Somit wurden nicht nur Lipidtropfen, sondern auch Phospholipide aus Membranen mit in die Untersuchung eingebunden. In Abbildung 6B ist die relative Fettsäurekonzentration der Arachidonsäure über die Zeit aufgetragen. Ein deutlicher Anstieg war erkennbar, der nach etwa 12 h abflacht. Die Sättigung der Gesamtaufnahme in Makrophagen scheint später einzusetzen, als für Lipidtropfen durch Raman-Messungen festgestellt wurde. Dies deutet daraufhin, dass die Fettsäure zuerst in Lipidtropfen abgespeichert, aber zu späteren Zeiten vermehrt in die Phospholipidmembranen der Zellen eingebaut wurde. Höchstwahrscheinlich ist die schnelle Speicherung in Lipidtropfen ein Mechanismus gegen Lipotoxizität und Freisetzung von Eicosanoiden, da dadurch die Konzentration von freier Arachidonsäure verringert wird. Durch die GC-Analyse ist zu erkennen, dass der prozentuale Anteil an Adrensäure in den Zellen zunahm. Nach 24 h war der Anteil von 0,1 auf 16 % gestiegen (Table 1 in [CS1]).

Offensichtlich wird Arachidonsäure in den Makrophagen in Adrensäure umgewandelt, um die bioaktive Arachidonsäure in eine weniger aktive Fettsäure zu überführen (Figure 5 in [CS1]). Aufgrund des nur kleinen Unterschieds in der Kettenlänge durch eine Ethyleneinheit ($-(CH_2)_2-$) konnte in den Raman-Spektren nicht festgestellt werden, zu welchen Anteilen Arachidon- und Adrensäure in den Lipidtröpfchen gespeichert wurden.

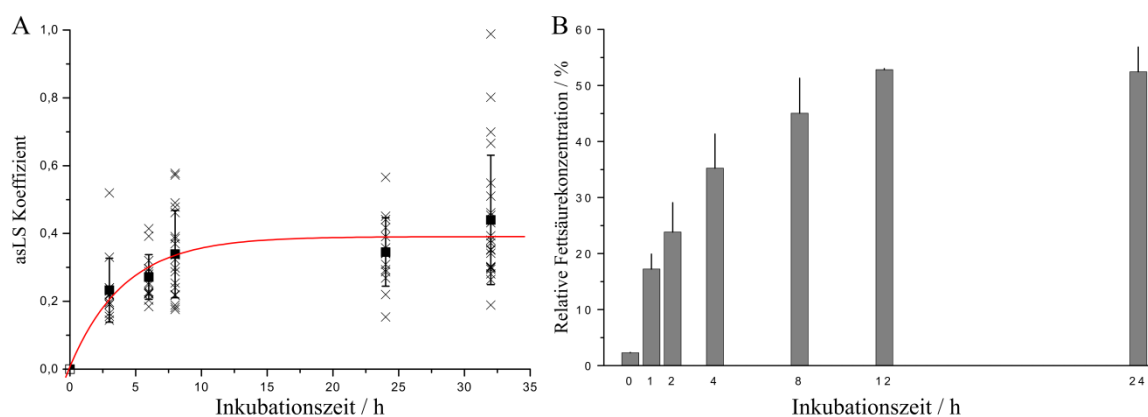


Abbildung 6 Quantifizierung der Aufnahme von Arachidonsäure über die Zeit

(A) Quantifizierung der Raman-Spektren basierend auf der CD-Bande zwischen 1900 und 2500 cm^{-1} mithilfe von asLS. Kreuz: Einzelzellwerte, Kasten: Mittelwert pro Zeitpunkt, Linie: angepasste Sättigungskurve. (B) GC-Daten der relativen Fettsäurekonzentration für Arachidonsäure.

Arachidon- und Palmitinsäure zeigten sehr unterschiedliche Aufnahmekapazitäten in THP-1-Makrophagen. Während Arachidonsäure keine Schaumzelltransformation hervorruft, wird Palmitinsäure deutlich effizienter in Lipidtröpfchen gespeichert und induziert eine deutliche Schaumzellbildung (60). In physiologischer Umgebung werden Makrophagen gleichzeitig unterschiedlichen Lipiden ausgesetzt. Um diesen Effekt nachzubilden, wurden in dieser Studie Zellen mit gleichen Anteilen deuterierter Palmitinsäure (d_{31} -Palmitinsäure) und d_8 -Arachidonsäure inkubiert. Da es sich um zwei verschiedene Fettsäuretypen handelt, konnte das Deuteriumsignal basierend auf vorhandenen Doppelbindungen unterschieden werden. Die vollständig gesättigte d_{31} -Palmitinsäure besitzt keine Doppelbindung und die Bandenmaxima liegen bei 2100 und 2197 cm^{-1} aufgrund von CD_2 - und CD_3 -Streckschwingungen und kann somit von der Bande bei 2248 cm^{-1} der d_8 -Arachidonsäure unterschieden werden. Abbildung 7A zeigt das Spektrum von d_{31} -Palmitinsäure in grün und d_8 -Arachidonsäure in schwarz. Das Spektrum in Rot stellt ein Lipidspektrum eines inkubierten Makrophagen dar, welches eindeutig die drei Bandenmaxima der verschiedenen CD-Schwingungen aufweist.

d_{31} -Palmitinsäure wurde schnell und homogen in die Lipidtropfen von inkubierten Makrophagen eingelagert. Dagegen zeigt d_8 -Arachidonsäure ein abweichendes Speicherverhalten, auch im Vergleich zur Einzelinkubation. Nicht in jedem Lipidtropfen konnte d_8 -Arachidonsäure gefunden werden. In Abbildung 7B sind die Konzentrationsverteilungen der Endmember von inkubierten Makrophagen bei unterschiedlichen Inkubationszeiten dargestellt. In Cyan ist die Proteinkomponente, in Gelb sind die Lipidtropfen mit d_{31} -Palmitinsäure und in Rot die Lipidtropfen mit d_{31} -Palmitinsäure und d_8 -Arachidonsäure aufgetragen. Bei kurzer Inkubationszeit konnte nur in wenigen Tropfen d_8 -Arachidonsäure nachgewiesen werden, aber selbst nach langen Inkubationszeiten von 24 h wurde sie nicht in jedem Lipidtropfen gespeichert. Dies führte zu dem Schluss, dass Arachidonsäure bei Ko-Inkubation mehr in Phospholipiden gespeichert wird.

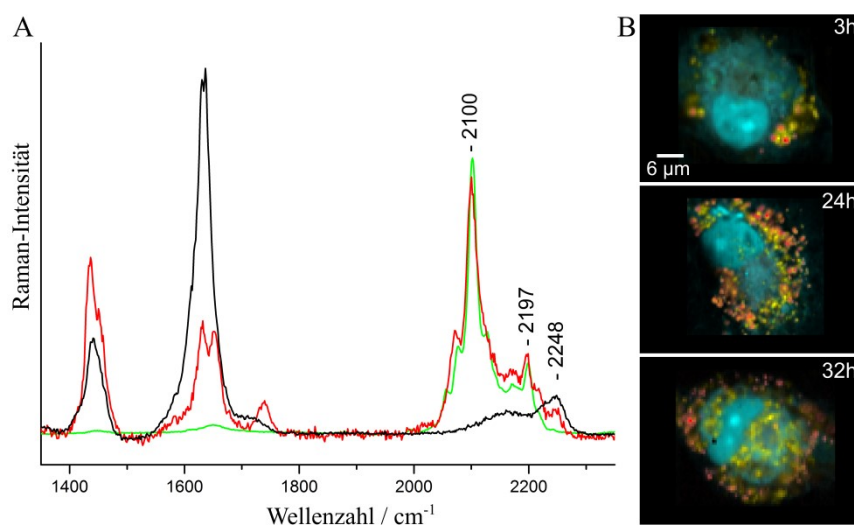


Abbildung 7 Ko-Inkubationsstudie mit zwei Fettsäuretypen

(A) Spektren von kristalliner d_8 -Arachidonsäure (schwarz), kristalliner d_{31} -Palmitinsäure (grün) und eines Lipidtropfens einer mit beiden Fettsäuren inkubierten Makrophage (rot). Eine klare Trennung der CD-Signale kann in Lipidtropfen visualisiert werden. (B) Konzentrationsverteilung von Protein (cyan), Lipidtropfen mit d_{31} -Palmitinsäure (gelb) und Lipidtropfen mit d_{31} -Palmitinsäure und d_8 -Arachidonsäure (rot). d_8 -Arachidonsäure wurde nur vereinzelt in Lipidtropfen gespeichert.

Zusammenfassend zeigte sich, dass Makrophagen eine geringere Aufnahmekapazität für Arachidonsäure als für Palmitinsäure haben. Die Elongation und Speicherung von Arachidonsäure verhindert, dass Eicosanoide gebildet werden können. Bei Ko-Inkubation wurde gezeigt, dass die Affinität Palmitinsäure in Lipidtropfen zu speichern größer ist als für Arachidonsäure.

2.2 Untersuchung von lebenden Makrophagen während der Inkubation mit deuterierter Palmitinsäure

([CS2] Stiebing et al. (2017) *J Biophotonics*. DOI: 10.1002/jbio.201600279)

Die Untersuchung von Zellen unter Lebendbedingungen ist von fundamentaler Bedeutung, um dynamische Prozesse in Zellen zu verstehen. Der Vorteil gegenüber fixierten Zellstudien besteht darin, dass dieselben Zellen über einen gewissen Zeitraum hinweg verfolgt werden können. Nur so können molekulare Dynamiken der Zellen untersucht werden. Besonders für Proliferations- oder Inkubationsstudien ist die zeitliche Überwachung von großer Bedeutung. Eine Herausforderung bei Lebendzellversuchen ist dabei, die Zellen während einer Messung lebensfähig zu halten und möglichst wenig zu beeinflussen.

Die bei fixierten Zellstudien verwendeten Fluoreszenzmarker sind für Lebendzellen oft ungeeignet, da sich diese zytotoxisch auswirken können (61). Vitalfärbungen, die auch in klinischer Umgebung für Operationen Anwendung finden, müssen speziell auf die Experimente abgestimmt und deren Toxizität überprüft werden (62, 63). Methoden wie GC oder MS können für Lebendzellversuche aufgrund der notwendigen Probenpräparation nicht angewendet werden (siehe Kapitel 1.2). Raman-Spektroskopie bietet ein hohes Potential für Lebendzellversuche. Da Wasser nur einen geringen Streuquerschnitt besitzt, können Zellen in wässrigem Medium gemessen werden, was notwendig für die Lebensfähigkeit der Zellen ist.

Das Ziel dieses Projektes war es, schnelle Raman-Bildgebungsverfahren für die Einzelzellanalyse zu etablieren und anzuwenden, um die Aufnahmekinetik von Lipiden in Echtzeit spektroskopisch zu verfolgen. Um lebende Zellen zu untersuchen, müssen bestimmte Umgebungsbedingungen eingehalten werden. Dazu wurde ein spezieller Aufbau verwendet, der aus einer beheizbaren Probenkammer besteht und mit Zellkulturmedium gefüllt werden kann (hier RPMI-1640 ohne Phenolrot). Die reifen Makrophagen wurden auf CaF₂-Objektträgern in den Lebendzellaufbau überführt. Für die Inkubation wurden jeweils 400 µM d₃₁-Palmitinsäure verwendet, die zuvor an Albumin gebunden wurde. Als erste Modalität wurde Raman-Mikrospektroskopie angewendet und

die Inkubation wurde kurz vor der Messung direkt am Messgerät gestartet. Die richtige Wahl von Messbedingungen spielte eine bedeutende Rolle, da die lebenden Zellen phototoxisch auf den Laser reagieren können.

In einer 2002 erschienenen Studie wurden Tests durchgeführt, um den Einfluss von Laserstrahlung auf Lebendzellen während der Raman-Spektroskopie zu testen (64). Lebende Lungenzellen blieben nach einer Bestrahlung von 40 min mit 785 nm bei 115 mW lebensfähig, was durch Zellviabilitätstests nachgewiesen wurde. Anders war dies bei einer Anregungswellenlänge von 488 und 514 nm, wo dramatische Veränderungen in der Zellmorphologie schon nach 5 min bei nur 5 mW Leistung auftraten. Eigens durchgeführte Experimente unterstützen diese Ergebnisse, wobei Anregungswellenlängen bei 514 und 633 nm getestet wurden. Während Zellen bei 514 nm bereits nach wenigen Minuten nicht mehr lebensfähig waren, veränderte sich die Morphologie der Zellen bei 633 nm nur wenig. Allerdings wurde keine Aufnahme von Lipiden detektiert, was darauf hindeutet, dass die Zellen phototoxisch auf die Laserwellenlänge reagierten. Bei Anregung mit 785 nm war dagegen eine klare Aufnahme von Lipiden sichtbar, welche über einen Zeitraum von mehr als 5 h verfolgt werden konnte.

Für die Messungen wurde eine deutlich verkürzte Integrationszeit von 85 ms eingesetzt. Dadurch konnte ein ausgewählter Zellbereich in weniger als 4 min in Abständen von 15 min aufgenommen werden. Für gewöhnlich werden Zeiten im Bereich von Sekunden für biologische Proben verwendet. Eine signifikante Verbesserung der Aufnahmegeschwindigkeit ist somit erreicht worden. Die Schnelligkeit der Bildaufnahme ist auch aufgrund von morphologischen Veränderungen der Zellen von Bedeutung. So sind zum Beispiel Lipidtropfen keine starren Organellen, sondern können sich im Zytoplasma diffus oder auch aktiv bewegen (65). Um keine Artefakte im Bild zu erzeugen, muss daher die Messung möglichst schnell durchgeführt werden. Trotz der kurzen Integrationszeit war ein intensives Signal von Lipiden und somit gutes Signal-Rausch-Verhältnis gewährleistet. In Abbildung 8 sind exemplarisch die Ergebnisse einer Zelle dargestellt. Abbildung 8A zeigt die Lipidkomponente nach Auswertung mit dem N-FINDR-Algorithmus für unterschiedliche Zeitpunkte. Eine deutliche Zunahme der CD-Schwingungen zwischen 2000 und 2400 cm^{-1} ist sichtbar. Ebenfalls sind typische Lipidschwingungen im niedrigeren Wellenzahlbereich zwischen 600 und 1800 cm^{-1} vorhanden, die eine

Zusammensetzung unterschiedlicher Lipide darstellt. Zum Beispiel ist anhand der C=C-Streckschwingung bei 1650 cm^{-1} erkennbar, dass auch ungesättigte Fettsäuren vorhanden sind. Abbildung 8B zeigt die relative Konzentrationsverteilung der Spektren aus Abbildung 8A für den aufgenommenen Ausschnitt der Zelle. Die Lipide sind in Tropfen gespeichert und ringförmig um den Nukleus angeordnet (Figure 2A in [CS2]). Das farblich-kodierte Lipidsignal steigt innerhalb der dargestellten 4 h deutlich an. Weiterhin ist zu sehen, dass die Anzahl der Lipidtropfen über die Zeit zunimmt. Besonders deutlich wird dies in der oberen rechten Ecke der Bildausschnitte.

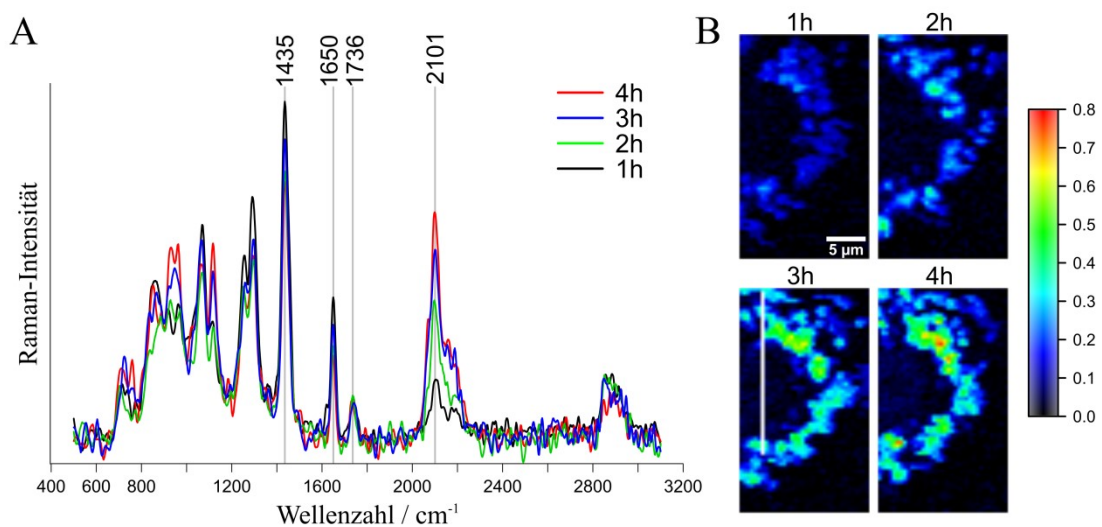


Abbildung 8 Lebendzellversuche mit Raman-Mikrospektroskopie

(A) Dargestellt ist die Lipidkomponente einer Zelle als Endmember für unterschiedliche Zeitpunkte. (B) Darstellung der relativen Konzentrationsverteilung der Endmember innerhalb des gemessenen Bildausschnitts.

Spontane Raman-Spektroskopie bietet eine umfangreiche spektrale Übersicht der chemischen Substanzen im Laserfokus. Allerdings werden durch das Abrastern der Probe die Aufnahmegeschwindigkeit und die Größe des Bildes begrenzt. Wie in Kapitel 1.3.1 beschrieben wurde, ist bei nicht-linearen Methoden wie SRS eine deutlich schnellere Aufnahme möglich. Versuche mit SRS wurden durchgeführt, um größere Zellansammlungen zeitgleich untersuchen zu können. Zur Detektion des SRS-Signals wurde dazu der Bereich der CD-Schwingungen bei 2125 cm^{-1} ausgewählt. Dadurch erhält man ausschließlich Informationen über die in den Zellen abgespeicherte d_{31} -Palmitinsäure. Das SRS-Signal ist linear abhängig von der Menge der angeregten Bindungen, wodurch eine Abschätzung über die abgespeicherte Fettsäure gemacht werden kann.

Die Inkubation wurde vor Beginn der Messung gestartet, um zu gewährleisten, dass bereits d_{31} -Palmitinsäure in den Lipidtröpfchen gespeichert wurde und somit das SRS-Signal für die Detektion intensiv genug war. Durch vorangegangene Inkubationsstudien mit fixierten Makrophagen ist bekannt, dass selbst für lange Inkubationszeiten von über 30 h die Aufnahme von d_{31} -Palmitinsäure nicht gesättigt ist (60). Die Messung wurde nach 17 h Inkubationszeit gestartet und alle 30 min wurde ein Bild von mehreren Zellen aufgenommen. In Abbildung 9A ist die aufgenommene Makrophagenpopulation mit überlagertem SRS-Signal in Gelb dargestellt. Es stellte sich heraus, dass die Zellen in zwei Klassen unterteilt werden können. Einige Zellen hatten zu Beginn der Messung bereits eine hohe SRS-Intensität, welche sich während der Messung bei den meisten nicht veränderte. Die Aufnahmekapazität von d_{31} -Palmitinsäure scheint in diesen Zellen bereits in den ersten 17 h der Inkubation ausgeschöpft zu sein. Zellen mit einem konstanten SRS-Signal sind in Abbildung 9A schwarz markiert. Bei den rot markierten Zellen stieg die Intensität und somit die Konzentration an gespeicherter d_{31} -Palmitinsäure über die Messzeit an. Die meisten dieser Zellen zeigten eine deutlich kleinere Anfangsintensität, die um das 50-fache geringer war. Um den Konzentrationsanstieg auszuwerten, wurden die Pixelwerte einer Zelle pro Zeitpunkt aufsummiert und als SRS-Intensität über die Zeit aufgetragen. Der Intensitätsanstieg ist beispielhaft für drei Zellen in Abbildung 9B für die in Abbildung 9A nummerierten Zellen aufgetragen. Deutlich wird, dass sich innerhalb einer Zelle die Aufnahmerate verändern kann. In Zelle 3 kann beobachtet werden, dass nach 24 h die Aufnahme beschleunigt und vermehrt d_{31} -Palmitinsäure abgespeichert wurde. Der sprunghafte Anstieg und Abfall bei 18 h stellt dagegen ein Fokusartefakt dar, welches aufgrund der Bewegung der Zelle entstand. Morphologische Veränderungen in der Lipidstruktur der Zellen aufgrund der Inkubation konnten nachverfolgt werden (Figure 4 in [CS2]). Generell konnte keine Abnahme von d_{31} -Palmitinsäure festgestellt werden.

Offensichtlich ist die Aufnahmekinetik für individuelle Zellen verschieden, was zu einer großen Heterogenität innerhalb der Zellpopulation führt. Die Zell-zu-Zell-Heterogenität ist höchstwahrscheinlich ein Mechanismus, um die Lipotoxizität bei einem Überangebot von Lipiden zu reduzieren, die bei der vorliegenden Inkubationsstudie simuliert wurde. Eine 2013 veröffentlichte Studie unterstützt die Ergebnisse, da diese ebenfalls eine Heterogenität zwischen Zellen derselben Population berichtet (66). Allerdings wurde nicht

die Zusammensetzung sondern die Anzahl der Lipidtropfen bestimmt. Innerhalb einer Leberzellpopulation wurden einige Zellen gefunden, die eine hohe Anzahl von Lipidtropfen im Vergleich zu den anderen besaßen. Die Autoren beschreiben, dass diese Zellen eine wichtige Rolle für die Zellpopulation einnehmen, da sie die Freisetzung toxischer Botenstoffe beeinflussen und Zellen mit geringerem Lipidgehalt mit Lipiden versorgen können.

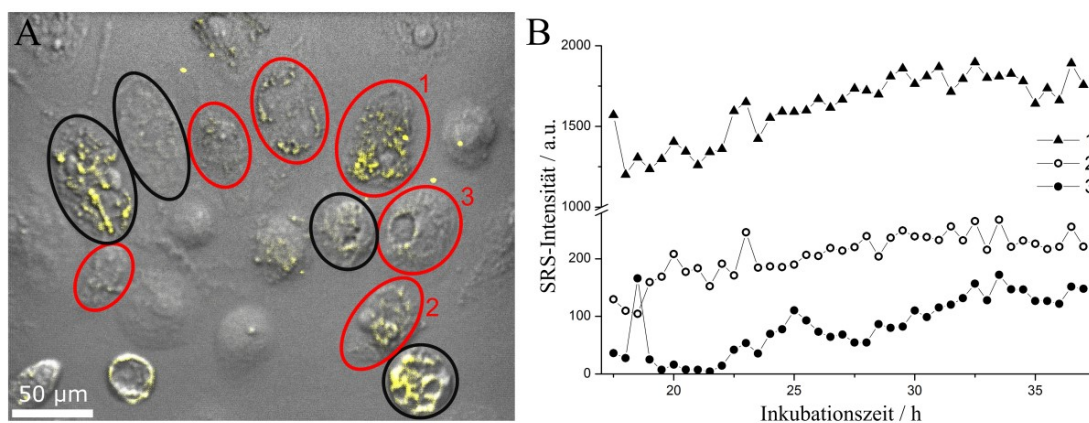


Abbildung 9 Lebendzellversuche mit SRS

(A) Übersichtsbild der aufgenommenen Zellpopulation mit überlagertem SRS-Signal in Gelb. Zellen mit konstanter SRS-Intensität sind schwarz und Zellen mit steigender Intensität rot markiert. (B) SRS-Intensität der in A nummerierten Zellen über die Zeit.

Zusammenfassend wurde innerhalb dieses Projektes eine umfassende Übersicht über die Aufnahmekinetik von d_{31} -Palmitinsäure in Makrophagen dargestellt. Mithilfe von spontaner Raman-Spektroskopie konnten die frühen Inkubationszeiten untersucht werden. Ein deutlicher Anstieg des CD-Signals und eine Vermehrung der Lipidtropfen wurde detektiert. Durch SRS konnte eine Ansammlung von Zellen über einen langen Zeitraum beobachtet werden. Die Aufnahme von d_{31} -Palmitinsäure stellte sich als dynamische Komponente heraus und Zellen konnten aufgrund der gespeicherten d_{31} -Palmitinsäure in zwei Klassen unterteilt werden.

2.3 Aufnahme von deuteriertem Tripalmitin durch Makrophagen über den Lipoproteintransportweg

([CS3] Stiebing et al. (2017) *J Lipid Res.* 58(5): 876–883)

Das Auftreten von modifiziertem LDL ist ein Schlüsselfaktor bei der frühen atherosklerotischen Plaqueentwicklung. Da Lipide in der Blutbahn hauptsächlich über Lipoproteine transportiert werden, ist es von Bedeutung, die Wechselwirkung zwischen modifiziertem LDL und Makrophagen zu untersuchen. Erst wenn der Aufnahmeprozess verstanden ist, kann die frühzeitige Plaqueentstehung mit verbesserten therapeutischen Ansätzen minimiert oder gar verhindert werden. Das Ziel dieses Projektes war es daher, das Verhalten von Makrophagen während der Inkubation mit oxLDL zu untersuchen und die Speicherung von Triglyceriden nachzuverfolgen, die durch die Aufnahme von oxLDL in Makrophagen eingelagert werden.

Die Experimente in den vorangegangenen Kapiteln basierten der Aufnahme von Fettsäuren, die an das Protein Albumin gebunden vorlagen. Wie in Kapitel 1.1 beschrieben wurde, ist der Aufnahme- und Speicherprozess von LDL beziehungsweise oxLDL deutlich komplexer, da die Partikel über Endozytose aufgenommen werden. Bisher gibt es nur wenige Forschungsarbeiten über bildgebende Verfahren, die die Aufnahme von Lipoproteinen behandeln. Neben fluoreszenzbasierten Studien (67), wurden CARS-Studien über die Aufnahme von Fettsäuren aus Lipolyseprodukten von Lipoproteinen durchgeführt (68, 69). Allerdings wurde durch die Zerstörung der Lipoproteine der native Aufnahmeweg nicht berücksichtigt.

Im Zuge dieses Projektes wurde ein Zellkulturprotokoll entwickelt, um deuterierte Triglyceride in oxLDL zu komplexieren und in die Zellen einzubringen. LDL wurde dafür aus dem Blut von gesunden Spendern durch Ultrazentrifugation isoliert und mit CuSO_4 oxidiert. Als Triglycerid wurde das an den Seitenketten vollständig deuterierte Tri(palmitin- d_{31}) (d-TP) ausgewählt. Um es erfolgreich in oxLDL zu überführen, wurde d-TP zuerst in Liposomen eingeschlossen. Dazu wurde Phosphatidylcholin mit d-TP in einer wässrigen Lösung über 6 h sonifiziert. Die dadurch entstandenen Liposomen wurden direkt im Anschluss mit oxLDL in RPMI-1640 Zellkulturmedium für etwa 17 h bei 37 °C

gemischt, wodurch die Liposomen mit den Lipoproteinen fusionieren. THP-1-Makrophagen wurden auf CaF₂-Objektträgern kultiviert und anschließend mit 50 µg/mL d-TP-beladenem oxLDL inkubiert. Nach unterschiedlichen Zeitpunkten wurden die Makrophagen mit Paraformaldehyd fixiert. Raman-Mikrospektroskopie wurde bei einer Anregungswellenlänge von 785 nm durchgeführt. Raman-Bilder wurden mit einer Integrationszeit von 1 s und Schrittweite von 1 µm aufgenommen.

Die Zusammensetzung der Lipoproteine wird maßgeblich durch die Ernährung des Spenders beeinflusst. Neben Lipiden können auch lipophile Vitamine wie β -Carotin in LDL vorhanden sein. β -Carotin liefert aufgrund der konjugierten Doppelbindungen intensive Raman-Banden, besonders wenn in Resonanz bei ca. 450 nm angeregt wird (70, 71). In Abbildung 10A ist die Strukturformel und das Raman-Spektrum von β -Carotin bei einer Anregungswellenlänge von 785 nm dargestellt. Prominente Banden liegen bei 1511 cm⁻¹ aufgrund von C=C- und bei 1153 cm⁻¹ aufgrund von C-C-Streckschwingungen. Die Bande bei 1006 cm⁻¹ kann C=CH₃-Methylschwingungen und CH-Deformationsschwingungen zugeordnet werden (72). In Abbildung 10B ist das Raman-Spektrum von oxLDL aufgetragen. Beiträge von β -Carotin sind deutlich sichtbar, wobei die Banden aufgrund der veränderten Konformation innerhalb der LDL-Partikel im Vergleich zur kristallinen Form leicht verschoben sind. Weitere Banden im niedrigen Wellenzahlbereich zeigen ebenfalls eine Mischung aus Lipiden und Proteinen.

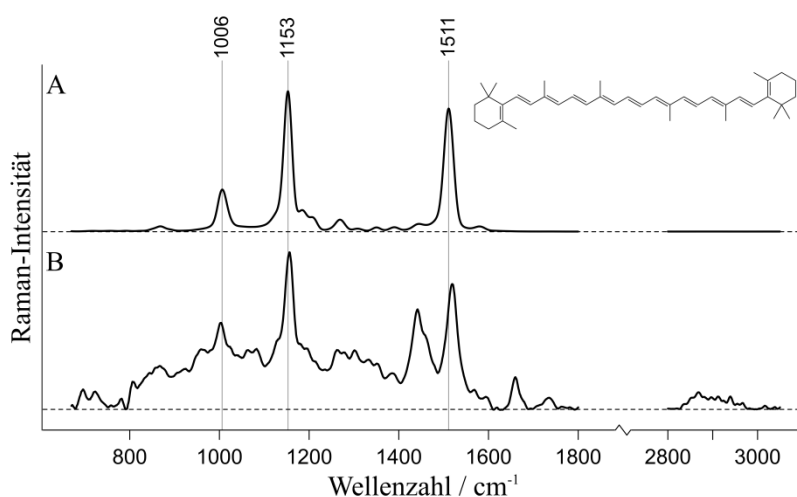


Abbildung 10 Vergleich von oxLDL und β -Carotin

- (A) Strukturformel und Spektrum von β -Carotin aufgenommen bei einer Anregungswellenlänge von 785 nm.
(B) Spektrum von oxLDL mit spektralen Beiträgen von β -Carotin.

THP-1-Makrophagen enthalten unter normalen Zellkulturbedingungen kein β -Carotin. Nur nach Inkubation mit oxLDL gelangt dieses in die Zellen, welches somit als Indikatormolekül für die Aufnahme angesehen werden kann. Nach 24 h kann β -Carotin in Lipidtropfen von Makrophagen nachgewiesen werden (Figure 2 in [CS3]). Als spezifische Indikation für die Aufnahme von oxLDL eignet sich die C=C-Schwingungsbande bei 1519 cm^{-1} (in kristalliner Form bei 1511 cm^{-1}), da die weiteren Banden durch andere Schwingungen, zum Beispiel von Phenylalanin oder d-TP, überlagert werden können.

Durch die mittels Inkorporation von d-TP in oxLDL bewirkte Aufnahme konnten ebenfalls CD-Schwingungen von d-TP nach 24 h in Zellen detektiert werden. Da alle Wasserstoffatome an den drei Palmitinsäureketten deuteriert sind, entsteht eine intensive Bande durch symmetrische CD_2 -Streckschwingungen bei 2103 cm^{-1} (Figure 3A in [CS3]). Die endständigen CD_3 -Gruppen schwingen bei 2193 cm^{-1} und die Carboxylestergruppen bei 1734 cm^{-1} . Beiträge von d-TP wurden in Lipidtropfen gefunden (Figure 3B in [CS3]). Die CD-Schwingung ist in der Lipidkomponente (rotes Spektrum) zu sehen, wobei im niedrigen Wellenzahlbereich nicht-deuterierte Lipide dominieren. Das exogen hinzugefügte d-TP wird somit gemeinsam mit endogenen Lipiden abgespeichert. Im Gegensatz zum Transport von Lipiden in Albumin wurden bei Inkubation mit oxLDL zwei weitere Komponenten gefunden. Neben den Lipidtropfen in Rot und der Proteinkomponente in Cyan ist auch ein endozytotisches Vesikel sichtbar, das nur etwa $2\text{ }\mu\text{m}$ groß ist (dargestellt in Orange in Figure 3B und C in [CS3]). Klar dominierend sind spektrale Beiträge von d-TP, wobei die Bande bei 1519 cm^{-1} ebenfalls das Vorkommen von β -Carotin beweist. Die blau dargestellte Komponente zeigt intensive Banden von β -Carotin und ist in der Nähe des Nukleus und ER lokalisiert. Das Spektrum besitzt Ähnlichkeit zu dem von oxLDL mit zusätzlichen Lipidbeiträgen (siehe Abbildung 10). Möglicherweise handelt es sich hierbei um frühe Endosome, bei denen das aufgenommene oxLDL noch nicht metabolisiert wurde.

Übergreifend kann eine interessante Aussage zu den endozytotischen Vesikeln aufgestellt werden. Abhängig von der Inkubationszeit scheint sich die Zusammensetzung der Vesikel zu verändern. Abbildung 11A zeigt beispielhaft drei Spektren von Vesikeln aus Zellen unterschiedlicher Inkubationszeiten. Während bei frühen Zeiten von 24 h spektrale Beiträge von d-TP dominieren, ist zu längeren Zeiten eine klare Abnahme der CD-

Schwingungen sichtbar. Ebenfalls ist die Struktur im niedrigen Wellenzahlbereich deutlich verändert. Die intensivste Bande bei 72 h liegt bei 719 cm^{-1} , die in den anderen Spektren deutlich schwächer ausgeprägt ist. Die Bande kann CN-Schwingungen der Cholingruppe von Phosphatidylcholinen zugeordnet werden (73), welches der Hauptbestandteil der Lipidmembran von LDL ist und ebenfalls für die Bildung der Liposomen verwendet wurde. Ein Beitrag von β -Carotin ist sichtbar, der aber nicht von der Inkubationszeit abhängt. Gleichzeitig zu der sinkenden Konzentration von d-TP in den Vesikeln, steigt das CD-Signal in den Lipidtropfen der gleichen Zellen (siehe Abbildung 11B). Die CD-Schwingungen steigen deutlich an und zu höheren Inkubationszeiten wird auch der niedrige Wellenzahlbereich von deuterierten Verbindungen dominiert. Aufgrund der Metabolisierung von oxLDL in endozytotischen Vesikeln ist es wahrscheinlich, dass d-TP gespalten und die frei gewordenen Palmitinsäuremoleküle während der Speicherung in Lipidtropfen zu neuen Triglyceriden zusammengesetzt werden (siehe Kapitel 1.1). Dabei kann die d_{31} -Palmitinsäure auch mit anderen Fettsäureketten kombiniert worden sein. Wieder wurden β -Carotinbanden unabhängig von der Inkubationszeit in den Spektren gefunden.

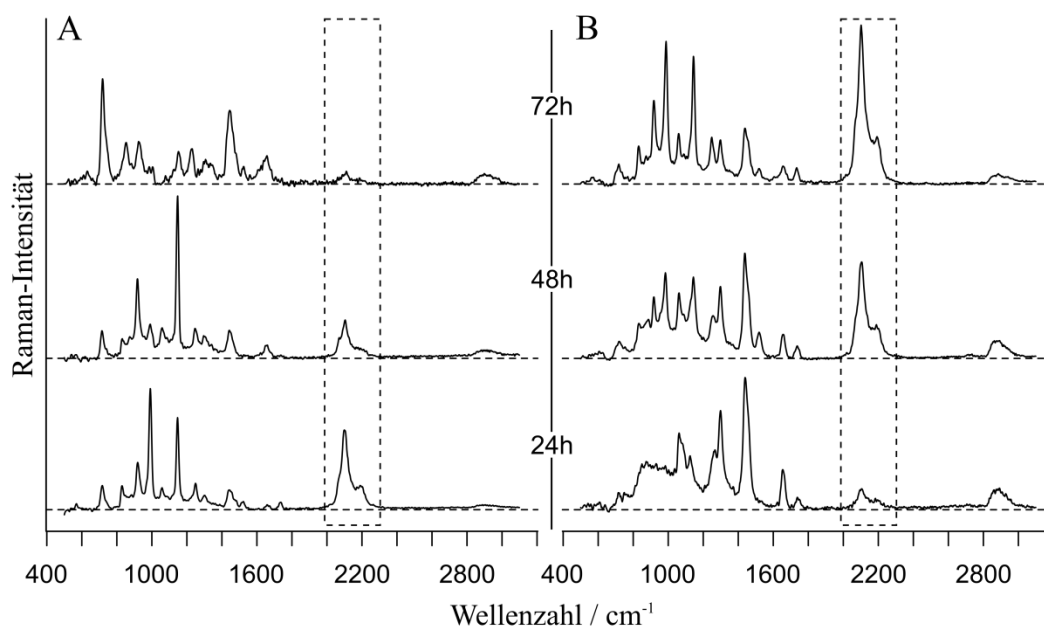


Abbildung 11 Zeitliche Übersicht von endozytotischen Vesikeln und Lipidtropfen

Raman-Spektren von (A) endozytotischen Vesikeln und (B) Lipidtropfen zu unterschiedlichen Zeitpunkten. Spektren auf einer Zeile wurden aus derselben Zelle entnommen und repräsentieren Endmember.

Eine hohe Heterogenität in Bezug auf Zellen der gleichen Inkubationszeit ist ebenfalls festgestellt worden (Figure 5 in [CS3]). Während die Konzentration und Verteilung von d-TP innerhalb einer Zelle gleichmäßig waren, sind diese im Vergleich zwischen Zellen sehr unterschiedlich. Ebenfalls ist nicht in allen Zellen die oxLDL-ähnliche Komponente zu finden. Die Heterogenität zeigt, dass oxLDL trotz identischer Inkubationszeit nicht gleichmäßig von Zellen einer Population aufgenommen wird. Es wurde keine klare Schaumzelltransformation festgestellt.

Zusammenfassend wurde ein zeitlicher Transfer von deuterierten Lipiden zwischen endozytotischen Vesikeln und Lipidtropfen beobachtet. Eine Homogenität der Lipidzusammensetzung auf Einzelzellebene wurde festgestellt, aber auch eine hohe Heterogenität zwischen Zellen einer Inkubationszeit.

3 Zusammenfassung

Die vorliegende Dissertation thematisiert die Visualisierung des Lipidmetabolismus von Makrophagen durch Raman-spektroskopische Bildgebungsverfahren. Um Erkenntnisse über die Mechanismen der Atherogenese auf Einzelzellebene zu gewinnen, wurden Inkubationsstudien mit unterschiedlichen Aufnahmeprozessen sowie verschiedenen Fettsäuren und Triglyceriden durchgeführt. Neben Studien an fixierten Zellen wurden auch lebende Zellen untersucht, bei denen der Zellmetabolismus erhalten war. Die Kombination von Raman-Spektroskopie mit stabiler Isotopenmarkierung durch Deuterium ermöglichte es die Aufnahmekinetik von Lipiden und deren Speicherprozess in intrazellulären Lipidtröpfchen zu erforschen.

Im ersten Projekt wurde gezeigt, dass die bioaktive Arachidonsäure bei einem Überangebot vermehrt in Lipidtröpfchen von Makrophagen abgespeichert wird, aber keine Schaumzellbildung hervorruft [CS1]. Anhand der Raman-Daten konnten chemische Informationen aus Lipidtröpfchen gewonnen und diese in Einzelzellen lokalisiert werden. Die Konzentrationsverteilung in Lipidtröpfchen innerhalb einer Zelle war homogen und eine Sättigung trat bereits nach 8 h ein. Eine Sättigung des Gesamtlipidgehalts einer Zelle setzte scheinbar erst nach etwa 12 h ein, wie durch GC-Messungen gezeigt wurde. Neben der Speicherung in Lipidtröpfchen ist eine Einlagerung in zelluläre Phospholipidmembranen wahrscheinlich. Eine Auftrennung der C=C-Schwingungsbande in zwei Maxima wurde detektiert, die zum einen durch nicht-deuterierte Fettsäuren und zum anderen durch d_8 -Arachidonsäure hervorgerufen wurden. Eine intrazelluläre Oxidation von d_8 -Arachidonsäure konnte somit ausgeschlossen werden. Allerdings wurde eine Elongation der Arachidonsäure durch den deutlichen Anstieg der relativen Konzentration der Adrensäure in den GC-Daten festgestellt. Da sich die beiden Fettsäuren nur durch eine Ethyleneinheit unterscheiden, konnten diese nicht in den Raman-Daten separiert werden. Die Speicherung von Arachidonsäure in Lipidtröpfchen sowie die Kettenverlängerung ist höchstwahrscheinlich ein Mechanismus gegen die Bildung entzündungsfördernder Eicosanoide, die aus freier Arachidonsäure entstehen können. Insgesamt stellte sich die Speicherung von Arachidonsäure als deutlich ineffizienter als die der gesättigten Palmitinsäure heraus. In Inkubationsstudien mit gleichzeitiger Zuführung von

d_8 -Arachidon- und d_{31} -Palmitinsäure wurde deutlich, dass d_{31} -Palmitinsäure homogen über die Zelle in alle Lipidtropfen verteilt wird. d_8 -Arachidonsäure dagegen wurde nur vereinzelt in Lipidtropfen gefunden. Dies steht stark in Kontrast zur Einzelinkubation der Fettsäure, wo eine homogene Verteilung in alle Lipidtropfen beobachtet wurde. Bei gleichzeitigem Angebot der verschiedenen Fettsäuren dominiert Palmitinsäure in Lipidtropfen. Eine deutliche Schaumzellformation wurde nur durch Palmitinsäure hervorgerufen, nicht aber durch Arachidonsäure. Bei einem Überangebot induziert die gesättigte Palmitinsäure somit schneller toxische Lipidwerte in Makrophagen als Arachidonsäure.

Durch Lebendzellversuche im zweiten Projekt konnte die Aufnahmekinetik von d_{31} -Palmitinsäure in einzelnen Makrophagen über einen langen Zeitraum verfolgt werden [CS2]. Dabei wurde durch Kombination von Raman-Mikrospektroskopie und SRS-Bildgebung eine Zeitspanne von bis zu 37 h abgedeckt. Raman-Mikrospektroskopie zeigte den besten Kompromiss zwischen Lebensfähigkeit der Zellen und Signalintensität bei einer Anregungswellenlänge von 785 nm. Niedrigere Wellenlängen, welche durch die ω^4 -Abhängigkeit ein stärkeres Signal erzeugen, führten aufgrund der höheren Energieübertragung zu phototoxischen Effekten in den Zellen. Durch eine kurze Integrationszeit von 85 ms konnte in 4 min ein Raman-Bild aufgenommen werden. Neben der Akkumulation von d_{31} -Palmitinsäure in Lipidtropfen konnte auch eine steigende Anzahl von Lipidtropfen im Bildausschnitt festgestellt werden. Die Lipidtropfen ordneten sich in der Nähe des ER an, was den derzeitigen Forschungsstand zur Lipidtropfenbildung bestätigt (5). SRS-Bildgebung ermöglichte es, die Aufnahmekinetik in mehreren Makrophagen gleichzeitig zu verfolgen. Auf Einzelzellbasis unterschied sich die Aufnahme deutlich, sodass eine Heterogenität in der zellulären Konzentration von d_{31} -Palmitinsäure in der Zellpopulation vorherrschte. Darauf basierend konnten die Makrophagen in zwei Klassen unterteilt werden. Während einige Zellen die Aufnahmekapazität in den ersten 17 h ausschöpften und eine konstante Konzentration von d_{31} -Palmitinsäure über den Messzeitraum zeigten, stieg die Konzentration in den meisten Zellen. Letztere zeigten ebenfalls eine geringere Konzentration zu Beginn der Messung. Es stellte sich heraus, dass sich die Aufnahmerate einer Zelle während der Inkubation verändern kann.

In der dritten Forschungsstudie wurde die endozytotische Aufnahme von oxLDL durch Makrophagen und die anschließende Speicherung von Lipiden aus den Partikeln zum ersten Mal bildgebend untersucht [CS3]. Ein Indikatormolekül für die Aufnahme wurde in Form von β -Carotin in den oxLDL-Partikeln gefunden, welches in kultivierten THP-1-Makrophagen nicht vorhanden ist. Die Bande bei 1519 cm^{-1} wurde als Indikator bestimmt. Innerhalb einer Zelle wurde β -Carotin homogen in den Lipidtropfen von Makrophagen gespeichert. Weiterhin konnte eine zusätzliche, bisher nicht eindeutig identifizierbare, zelluläre Komponente mit hohem β -Carotingehalt in vereinzelt Zellen beobachtet werden. Da die spektralen Eigenschaften denen des oxLDL ähnlich waren, könnte es sich hier um frühe Endosome handeln, in denen das oxLDL noch nicht metabolisiert wurde. Diese Komponente trat lokalisiert in der Nähe des Nukleus und des ER auf. In einer früheren Studie wurde β -Carotin in Ablagerungen von Aortenklappen gefunden und diskutiert, dass dieses durch die Aufnahme und Metabolisierung von LDL durch Makrophagen in die Ablagerungen gelangen könnte (53). Diese Aussage kann durch die in der vorliegenden Arbeit präsentierten Daten untermauert werden. Der Speicherprozess von Lipiden, die durch oxLDL in die Zellen transportiert wurden, konnte aufgrund der Inkorporation von d-TP untersucht werden. Die deuterierten Lipide wurden homogen in die Lipidtropfen einer Zelle verteilt, die Konzentration in individuellen Zellen bei gleicher Inkubationszeit war aber sehr unterschiedlich. Die Menge des aufgenommenen oxLDL pro Zelle scheint nicht zeitlich reguliert zu sein, wodurch die gezeigte Heterogenität erklärt werden könnte. Die unterschiedlichen endozytotischen Aufnahmewege, die in Kapitel 1.1 beschrieben wurden, können gleichzeitig stattfinden und zu der Variation beitragen. Intrazelluläre Vesikel mit einer Größe von nur etwa $2\text{ }\mu\text{m}$, die aufgrund der endozytotischen Aufnahme von oxLDL entstehen, konnten gefunden werden. Die spektralen Informationen waren abhängig von der Inkubationszeit. Über die CD-Schwingungsbanden konnte erstmals eine Translokation von deuterierten Lipiden zwischen endozytotischen Vesikeln und Lipidtropfen verfolgt werden.

Eine Heterogenität in der Lipidkonzentration unterschiedlicher Zellen einer Inkubationszeit konnte in allen drei vorgestellten Studien festgestellt werden. Besonders auffällig war dies bei der Aufnahme von oxLDL und den Lebendzellversuchen. Aber auch bei den Experimenten mit Arachidonsäure ist eine Heterogenität ersichtlich, wenn man die

Einzelzellwerte der asLS-Auswertung betrachtet. Obwohl die Mittelwerte für die Inkubationszeiten einen Trend zur Aufnahme und Sättigung darstellen, streuen die Einzelwerte relativ deutlich. Ob die Streuung der Konzentrationswerte auf der unterschiedlichen Aufnahmekinetik individueller Zellen beruht, die bei den Lebendzellversuchen festgestellt wurden, kann allerdings nicht bewiesen werden. Einige zellkulturbasierte Faktoren können ebenfalls zur Streuung beitragen. Das größte Problem ist, dass Studien mit fixierten Zellen auf getrennten Kulturansätzen für jeden Inkubationszeitpunkt beruhen. Außerdem kann sie auch hervorgerufen werden, weil sich die Makrophagen nicht im selben Status des Zellzyklus befanden, da die Ausdifferenzierung von Monozyten nicht synchronisiert werden kann. Wie in Kapitel 2.2 diskutiert, ist die Heterogenität in der Lipidkonzentration einer Zellpopulation vermutlich ein Mechanismus zur Reduzierung der Lipotoxizität und der Freisetzung toxischer Botenstoffe.

Wird die Aufnahme von Lipiden in Makrophagen über oxLDL mit der über den Albumintransport verglichen, so sieht man eine deutlich komplexere Zusammensetzung der Zelle. Während bei dem Albumintransport freie Fettsäuren direkt zur Speicherung in Makrophagen zur Verfügung stehen, werden die Triglyceride mit dem oxLDL endozytotisch aufgenommen und metabolisiert. Die benötigte Zeit, um deuterierte Lipide nachzuweisen, ist deutlich länger. Erst wenn das endozytotische Vesikel aufgenommen und abgebaut ist, können die deuterierten Fettsäuren der gespaltenen Triglyceride in den Lipidtropfen neu verestert und gespeichert werden. Nach 24 h konnten CD-Schwingungen in den Lipidtropfen detektiert werden. Unter Verwendung des Albumintransports war dies bereits nach 15 min möglich. Obwohl in beiden Ansätzen eine homogene Verteilung der deuterierten Lipide in den Lipidtropfen einer Zelle gezeigt werden konnte, war eine deutlich höhere Heterogenität innerhalb der Zellpopulation nach Aufnahme von oxLDL zu sehen. Eine Transformation zu Schaumzellen geschah nur bei Inkubation mit d_{31} -Palmitinsäure über den Albumintransport, aber nicht bei d-TP-beladenem oxLDL. Obwohl sich d-TP ebenfalls aus d_{31} -Palmitinsäure zusammensetzt, scheint die direkte Verfügbarkeit der freien Form toxischer für Makrophagen zu sein.

Raman-Spektroskopie in Verbindung mit stabiler Isotopenmarkierung ist eine leistungsstarke Kombination, um Inkubationsstudien auf Einzelzellbasis durchzuführen.

Die nur geringfügige Änderung durch die Deuterierung stellt ein leistungsfähiges Pendant zur etablierten Fluoreszenzmikroskopie dar. Eine umfangreiche Übersicht über den Albumin- und endozytotischen Lipoproteintransportweg konnte erstellt und der Beitrag von freien Fettsäuren sowie Triglyceriden zur Schaumzellbildung von Makrophagen auf Einzelzellebene untersucht werden. Eine interessante Weiterführung der Forschungsarbeiten wäre eine Verbindung mit einem mikrofluidischen Aufbau, in dem der Blutfluss über adhärente Makrophagen simuliert wird. Dies würde einen weiteren Schritt in Richtung der physiologischen Bedingungen in Arterien bedeuten.

4 Summary

The present thesis addresses the visualization of the lipid metabolism of macrophages by Raman spectroscopic imaging techniques. In order to gain insights into the mechanism of atherogenesis at the single cell level, incubation studies covering different uptake pathways as well as individual fatty acids and triglycerides were conducted. Next to studies on fixed cells, living cells under non-cytotoxic conditions to sustain the cell metabolism were investigated. Due to the combination of Raman spectroscopy with stable isotopic labelling with deuterium, uptake kinetics of lipids and their storage behavior in intracellular lipid droplets were investigated.

In the first project it was shown that bioactive arachidonic acid is stored in lipid droplets of macrophages in case of an overexposure but no prominent foam cell formation was observed [CS1]. Based on the Raman data, chemical information on lipid droplets was obtained and their location in single cells was identified. The fatty acid was distributed homogeneously in lipid droplets of one cell and saturation of intracellular accumulation was reached after 8 h. However, saturation based on the total cellular lipid content seemed to occur later after around 12 h, as shown by GC measurements. Next to the storage in lipid droplets, arachidonic acid was apparently incorporated into cellular membrane phospholipids. A separation of the C=C vibrational band into two maxima was detected, which is due to vibrations of non-deuterated fatty acids and d_8 -arachidonic acid. An intracellular oxidation of d_8 -arachidonic acid could thus be excluded. However, elongation of arachidonic acid is evident in the GC data due to the significant increase of the relative concentration of adrenic acid. Since the two fatty acids only differ by an ethylene unit, they cannot be distinguished in the Raman data. The storage of arachidonic acid in lipid droplets and the elongation process is most likely a mechanism against the formation of inflammatory eicosanoids, which can only be generated from free arachidonic acid. Overall, the storage of arachidonic acid was found to be less efficient than that of saturated palmitic acid. In incubation studies with simultaneous administration of d_8 -arachidonic acid and d_{31} -palmitic acid it was obvious that d_{31} -palmitic acid was distributed homogeneously in all cytosolic lipid droplets. In contrast, d_8 -arachidonic acid was found only in a few droplets. This contradicts the results from single incubation studies, where a

homogeneous distribution of d_8 -arachidonic within all lipid droplets was observed. If provided simultaneously, palmitic acid is preferred and predominantly incorporated in lipid droplets. Under these conditions, a clear foam cell formation was only mediated by palmitic acid but not by arachidonic acid. Hence, in case of overexposure saturated palmitic acid likely induces more rapidly toxic lipid levels in macrophages than arachidonic acid.

By conducting live cell experiments in the second project, uptake kinetics of d_{31} -palmitic acid could be monitored in individual macrophages over a long period of time [CS2]. Incubation times of up to 37 h were covered by combining Raman micro-spectroscopy and SRS imaging. Raman micro-spectroscopy presented the best compromise between cell viability and signal intensity at an excitation wavelength of 785 nm. Lower wavelengths, that produce a stronger signal due to the ω^4 dependency, resulted in phototoxic effects in the cells due to the higher energy transfer. A fast integration time of 85 ms provided a single Raman image in only 4 min. An accumulation of d_{31} -palmitic acid in lipid droplets and an increase of droplets in the image frame were observed. The lipid droplets were located close to the ER which is in line with the current state of research on lipid droplet formation (5). SRS imaging allowed the investigation of the uptake kinetics in several macrophages at the same time. The uptake differed between single cells which lead to a heterogeneity of the cellular concentration of d_{31} -palmitic acid in the cell population. A classification of macrophages into two groups was possible. While some cells exhausted their uptake capacity in the first 17 h and had a stable concentration of d_{31} -palmitic acid, in most cells the concentration increased. The latter also showed a lower concentration at the beginning of the measurement. It was found that the uptake rate of a cell can change during the incubation process.

In the third study, the endocytic uptake of oxLDL by macrophages and the subsequent storage of lipids provided by the particles were presented for the first time [CS3]. A marker molecule for the uptake of oxLDL was found due to the presence of β -carotene, which is not present in cultivated THP-1 macrophages. The band at 1519 cm^{-1} was specified as the marker band. Within one cell, β -carotene was stored homogeneously in lipid droplets of macrophages. Furthermore, in some cells an additional component with high β -carotene content could be observed. Since the spectral properties were similar to those of oxLDL,

these might represent early endosomes in which oxLDL had not yet been metabolized. The components occurred localized close to the nucleus and ER. In a previous study, β -carotene was found in plaque depositions of aortic valves (53). The authors discussed, that it could have been incorporated by the uptake and metabolism of LDL in macrophages. This concept is supported by the results presented in this thesis. The cellular storage process of lipids provided by oxLDL could be investigated due to the incorporation of d-TP. The deuterated lipids were distributed homogeneously within a cell, but the concentrations in cells with the same incubation time were highly different. The amount of oxLDL taken up by a cell in a certain time seems to not be regulated, which can result in the presented heterogeneity. The different endocytic uptake pathways, which were explained in Chapter 1.1, can occur at the same time and contribute to the variations. Intracellular vesicles with a size of only around 2 μm , resulting from the endocytic uptake of oxLDL, were found. The spectral information was dependent on the incubation time. Based on the CD vibration bands, a translocation of deuterated lipids between endocytic vesicles and lipid droplets was observed.

Heterogeneity of the lipid concentrations within cells with the same incubation time was found in all of the three presented studies. This was particularly obvious for oxLDL and live cell studies. But also in the experiments with arachidonic acid, heterogeneity can be seen by evaluating the individual asLS coefficients. Although the mean values for each incubation time follow the trend of uptake and saturation, the individual values are clearly scattering. If the scattering of the concentration values is based on different uptake kinetics of individual cells, as seen in the live cell studies, cannot be verified. Some cell culture-based factors may also contribute to the spread. The main problem is that studies of fixed cells are based on different cell culture batches for each incubation time. Furthermore, it can be caused due the fact that the macrophages were in different states of the cell cycle because the differentiation of monocytes cannot be synchronized. As discussed in Chapter 2.2, heterogeneity of the lipid concentration of a cell population is most likely a mechanism to reduce lipotoxicity and the release of toxic messenger molecules.

The uptake of lipids into macrophages by oxLDL compared to the albumin-based uptake leads to a more complex composition of the cells. While albumin-coupled fatty acids are directly available for storage in macrophages, triglycerides inside oxLDL are taken up and

metabolized by endocytosis. The time required to detect deuterated lipids in cytosolic lipid droplets is therefore significantly longer. Only after the endocytic vesicle is build and the particles metabolized, the deuterated fatty acids of the cleaved triglycerides can be re-esterified and stored in the lipid droplets. CD vibrations were detected in lipid droplets after 24 h. Using the albumin transport this was possible after only 15 min. Although a homogeneous distribution of the lipids within the lipid droplets of a cell was shown in both approaches, a significantly higher heterogeneity was observed in the cell population after the uptake of oxLDL. A prominent transformation into foam cells occurred only after incubation with d_{31} -palmitic acid through albumin transport, but not with d-TP-loaded oxLDL. Although d-TP is also composed of d_{31} -palmitic acid, the direct availability of the free form appears to be more toxic.

Raman spectroscopy in combination with stable isotopic labelling is a powerful method for incubation studies on the single cell level. Deuteration is an effective counterpart to the established fluorescence microscopy due to only introducing subtle changes. A comprehensive overview of the albumin and endocytic lipoprotein uptake pathways has been established and the contribution of free fatty acids and triglycerides to macrophage foam cell formation was investigated at the single cell level. An interesting continuation of the presented research would be the incorporation of the incubation studies into a microfluidic setup, where the blood flow over adherent macrophages can be simulated. This would be a further step towards physiological conditions in arteries.

5 Literaturverzeichnis

1. WHO (2016) World health statistics 2016: Monitoring health for the SDGs, sustainable development goals.
2. WHO (2014) Global status report on noncommunicable diseases 2014.
3. Lorkowski S, Cullen P (2007) Atherosclerosis: Pathogenesis, clinical features and treatment. In: eLS. John Wiley & Sons, Ltd.
4. Moore K, Sheedy F, Fisher E (2013) Macrophages in atherosclerosis: A dynamic balance. *Nat Rev Immunol.* 13: 709-721.
5. Wilfling F, Haas JT, Walther TC, Farese RV (2014) Lipid droplet biogenesis. *Curr Opin Chem Biol.* 29: 39-45.
6. Dai Y, Condorelli G, Mehta JL (2015) Scavenger receptors and non-coding RNAs: Relevance in atherogenesis. *Cardiovasc Res.* 109: 24-33.
7. Brash AR (2001) Arachidonic acid as a bioactive molecule. *J Clin Invest.* 107: 1339.
8. Goldberg IJ (1996) Lipoprotein lipase and lipolysis: Central roles in lipoprotein metabolism and atherogenesis. *J Lipid Res.* 37: 693-707.
9. Nauck M, Warnick GR, Rifai N (2002) Methods for measurement of LDL-cholesterol: A critical assessment of direct measurement by homogeneous assays versus calculation. *Clin Chem.* 48: 236-254.
10. Zhao Y-Y, Miao H, Cheng X-L, Wei F (2015) Lipidomics: Novel insight into the biochemical mechanism of lipid metabolism and dysregulation-associated disease. *Chem Biol Interact.* 240: 220-238.
11. Li L, Han J, Wang Z, Liu J, Wei J, Xiong S, Zhao Z (2014) Mass spectrometry methodology in lipid analysis. *Int J Mol Sci.* 15: 10492-10507.
12. Tranchida PQ, Donato P, Dugo G, Mondello L, Dugo P (2007) Comprehensive chromatographic methods for the analysis of lipids. *Trends Anal Chem.* 26: 191-205.
13. Cruz-Hernandez C, Destailats F (2012) Analysis of lipids by gas chromatography. In: Gas chromatography. Poole C, editor. Elsevier.

14. Horn PJ, Ledbetter NR, James CN, Hoffman WD, Case CR, Verbeck GF, Chapman KD (2011) Visualization of lipid droplet composition by direct organelle mass spectrometry. *J Biol Chem.* 286: 3298-3306.
15. Cajka T, Fiehn O (2014) Comprehensive analysis of lipids in biological systems by liquid chromatography-mass spectrometry. *Trends Anal Chem.* 61: 192-206.
16. Ellis SR, Brown SH, in het Panhuis M, Blanksby SJ, Mitchell TW (2013) Surface analysis of lipids by mass spectrometry: More than just imaging. *Prog Lipid Res.* 52: 329-353.
17. Lanni EJ, Rubakhin SS, Sweedler JV (2012) Mass spectrometry imaging and profiling of single cells. *J Proteomics.* 75: 5036-5051.
18. Sparvero LJ, Amoscato AA, Dixon CE, Long JB, Kochanek PM, Pitt BR, Bayir H, Kagan VE (2012) Mapping of phospholipids by MALDI imaging (MALDI-MSI): Realities and expectations. *Chem Phys Lipids.* 165: 545-562.
19. Berezin MY, Achilefu S (2010) Fluorescence lifetime measurements and biological imaging. *Chem Rev.* 110: 2641-2684.
20. Listenberger LL, Ostermeyer-Fay AG, Goldberg EB, Brown WJ, Brown DA (2007) Adipocyte differentiation-related protein reduces the lipid droplet association of adipose triglyceride lipase and slows triacylglycerol turnover. *J Lipid Res.* 48: 2751-2761.
21. Zhang H, Zhai Z, Zhou H, Li Y, Li X, Lin Y, Li W, Shi Y, Zhou M-S (2015) Puerarin inhibits oxLDL-induced macrophage activation and foam cell formation in human THP1 macrophage. *Biomed Res Int.* 2015: 403616.
22. Martins de Lima T, Cury-Boaventura MF, Giannocco G, Nunes MT, Curi R (2006) Comparative toxicity of fatty acids on a macrophage cell line (J774). *Clin Sci (Lond).* 111: 307-317.
23. Xu X, Zhang A, Li N, Li P-L, Zhang F (2015) Concentration-dependent diversification effects of free cholesterol loading on macrophage viability and polarization. *Cell Physiol Biochem.* 37: 419-431.
24. Daemen S, van Zandvoort MA, Parekh SH, Hesselink MK (2015) Microscopy tools for the investigation of intracellular lipid storage and dynamics. *Mol Metab.* 5: 153-163.

25. Galler K, Brautigam K, Gro, Popp J, Neugebauer U (2014) Making a big thing of a small cell - recent advances in single cell analysis. *Analyst*. 139: 1237-1273.
26. Phipps J, Sun Y, Saroufeem R, Hatami N, Fishbein MC, Marcu L (2011) Fluorescence lifetime imaging for the characterization of the biochemical composition of atherosclerotic plaques. *J Biomed Opt*. 16: 096018.
27. Cicchi R, Baria E, Matthäus C, Lange M, Lattermann A, Brehm BR, Popp J, Pavone FS (2015) Non-linear imaging and characterization of atherosclerotic arterial tissue using combined SHG and FLIM microscopy. *J Biophotonics*. 8: 347-356.
28. Bec J, Ma DM, Yankelevich DR, Liu J, Ferrier WT, Southard J, Marcu L (2014) Multispectral fluorescence lifetime imaging system for intravascular diagnostics with ultrasound guidance: In vivo validation in swine arteries. *J Biophotonics*. 7: 281-285.
29. Fatakdawala H, Gorpas D, Bishop JW, Bec J, Ma D, Southard JA, Margulies KB, Marcu L (2015) Fluorescence lifetime imaging combined with conventional intravascular ultrasound for enhanced assessment of atherosclerotic plaques: An ex vivo study in human coronary arteries. *J Cardiovasc Transl Res*. 8: 253-263.
30. Lattermann A, Matthäus C, Bergner N, Beleites C, Romeike BF, Krafft C, Brehm BR, Popp J (2013) Characterization of atherosclerotic plaque depositions by Raman and FTIR imaging. *J Biophotonics*. 6: 110-121.
31. Wrobel TP, Mateuszuk L, Kostogryś RB, Chlopicki S, Baranska M (2013) Quantification of plaque area and characterization of plaque biochemical composition with atherosclerosis progression in ApoE/LDLr^{-/-} mice by FT-IR imaging. *Analyst*. 138: 6645-6652.
32. Gazi E, Harvey TJ, Brown MD, Lockyer NP, Gardner P, Clarke NW (2009) A FTIR microspectroscopic study of the uptake and metabolism of isotopically labelled fatty acids by metastatic prostate cancer. *Vib Spectrosc*. 50: 99-105.
33. Baker MJ, Trevisan J, Bassan P, Bhargava R, Butler HJ, Dorling KM, Fielden PR, Fogarty SW, Fullwood NJ, Heys KA, Hughes C, Lasch P, Martin-Hirsch PL, Obinaju B, Sockalingum GD, Sulé-Suso J, Strong RJ, Walsh MJ, Wood BR, Gardner P, Martin FL (2014) Using fourier transform IR spectroscopy to analyze biological materials. *Nat Protoc*. 9: 1771-1791.

34. Long DA (2002) The Raman effect: A unified treatment of the theory of Raman scattering by molecules. John Wiley & Sons, Ltd.
35. McCreery RL (2000) Raman spectroscopy for chemical analysis. Winefordner JD, editor. John Wiley & Sons, Inc.
36. Schmitt M, Mayerhöfer T, Popp J, Kleppe I, Weisshart K (2011) Light–matter interaction. In: Handbook of biophotonics. Popp J, Tuchin VV, Chiou A, Heinemann SH, editors. Wiley-VCH Verlag GmbH & Co. KGaA.
37. Boyd RW (2008) Stimulated Raman scattering and stimulated Rayleigh-wing scattering. In: Nonlinear optics (third edition). Academic Press.
38. Krafft C, Schie IW, Meyer T, Schmitt M, Popp J (2016) Developments in spontaneous and coherent Raman scattering microscopic imaging for biomedical applications. *Chem Soc Rev.* 45: 1819-1849.
39. Tipping WJ, Lee M, Serrels A, Brunton VG, Hulme AN (2016) Stimulated Raman scattering microscopy: An emerging tool for drug discovery. *Chem Soc Rev.* 45: 2075-2089.
40. Alfonso-Garcia A, Pfisterer SG, Riezman H, Ikonen E, Potma EO (2015) D38-cholesterol as a Raman active probe for imaging intracellular cholesterol storage. *J Biomed Opt.* 21: 061003.
41. Fu D, Yu Y, Folick A, Currie E, Farese R, Tsai T-H, Xie XS, Wang MC (2014) In vivo metabolic fingerprinting of neutral lipids with hyperspectral stimulated Raman scattering microscopy. *J Am Chem Soc.* 136: 8820-8828.
42. Slipchenko MN, Le TT, Chen H, Cheng J-X (2009) High-speed vibrational imaging and spectral analysis of lipid bodies by compound Raman microscopy. *J Phys Chem B.* 113: 7681-7686.
43. Chen Z, Paley DW, Wei L, Weisman AL, Friesner RA, Nuckolls C, Min W (2014) Multicolor live-cell chemical imaging by isotopically edited alkyne vibrational palette. *J Am Chem Soc.* 136: 8027-8033.
44. Hedegaard M, Matthäus C, Hassing S, Krafft C, Diem M, Popp J (2011) Spectral unmixing and clustering algorithms for assessment of single cells by Raman microscopic imaging. *Theor Chem Acc.* 130: 1249-1260.

45. Bergner N, Krafft C, Geiger KD, Kirsch M, Schackert G, Popp J (2012) Unsupervised unmixing of Raman microspectroscopic images for morphochemical analysis of non-dried brain tumor specimens. *Anal Bioanal Chem.* 403: 719-725.
46. Winter ME (1999) N-FINDR: An algorithm for fast autonomous spectral end-member determination in hyperspectral data. *Proc SPIE.* 3753: 266-275.
47. Smith R, L. Wright K, Ashton L (2016) Raman spectroscopy: An evolving technique for live cell studies. *Analyst.* 141: 3590-3600.
48. Schie IW, Krafft C, Popp J (2015) Applications of coherent Raman scattering microscopies to clinical and biological studies. *Analyst.* 140: 3897-3909.
49. Cao C, Zhou D, Chen T, Streets AM, Huang Y (2016) Label-free digital quantification of lipid droplets in single cells by stimulated Raman microscopy on a microfluidic platform. *Anal Chem.* 88: 4931–4939.
50. Yu Y, Ramachandran PV, Wang MC (2014) Shedding new light on lipid functions with CARS and SRS microscopy. *Biochim Biophys Acta.* 1841: 1120-1129.
51. Yi Y-H, Chien C-H, Chen W-W, Ma T-H, Liu K-Y, Chang Y-S, Chang T-C, Lo SJ (2013) Lipid droplet pattern and nondroplet-like structure in two fat mutants of *caenorhabditis elegans* revealed by coherent anti-Stokes Raman scattering microscopy. *J Biomed Opt.* 19: 011011.
52. Kochan K, Maslak E, Krafft C, Kostogryz R, Chlopicki S, Baranska M (2015) Raman spectroscopy analysis of lipid droplets content, distribution and saturation level in non-alcoholic fatty liver disease in mice. *J Biophotonics.* 8: 597-609.
53. Bonetti A, Bonifacio A, Mora AD, Livi U, Marchini M, Ortolani F (2015) Carotenoids co-localize with hydroxyapatite, cholesterol, and other lipids in calcified stenotic aortic valves. Ex vivo Raman maps compared to histological patterns. *Eur J Histochem.* 59: 2505.
54. Dochow S, Fatakdawala H, Phipps JE, Ma D, Bocklitz T, Schmitt M, Bishop JW, Margulies KB, Marcu L, Popp J (2016) Comparing Raman and fluorescence lifetime spectroscopy from human atherosclerotic lesions using a bimodal probe. *J Biophotonics.* 9: 958-966.
55. Matthäus C, Dochow S, Bergner G, Lattermann A, Romeike BFM, Marple ET, Krafft C, Dietzek B, Brehm BR, Popp J (2012) In vivo characterization of atherosclerotic plaque depositions by Raman-probe spectroscopy and in vitro

- coherent anti-stokes Raman scattering microscopic imaging on a rabbit model. *Anal Chem.* 84: 7845-7851.
56. Gulbins E, Lang F (2007) Signaltransduktion. In: Physiologie des Menschen: Mit Pathophysiologie. Schmidt RF, Lang F, editors. Springer Berlin Heidelberg.
57. Thomas MH, Pelleieux S, Vitale N, Olivier JL (2016) Dietary arachidonic acid as a risk factor for age-associated neurodegenerative diseases: Potential mechanisms. *Biochimie.* 130: 168-177.
58. Astudillo AM, Balgoma D, Balboa MA, Balsinde J (2012) Dynamics of arachidonic acid mobilization by inflammatory cells. *BBA-Mol Cell Biol L.* 1821: 249-256.
59. van Manen H-J, Kraan YM, Roos D, Otto C (2005) Single-cell Raman and fluorescence microscopy reveal the association of lipid bodies with phagosomes in leukocytes. *Proc Natl Acad Sci USA.* 102: 10159-10164.
60. Matthäus C, Krafft C, Dietzek B, Brehm BR, Lorkowski S, Popp J (2012) Noninvasive imaging of intracellular lipid metabolism in macrophages by Raman microscopy in combination with stable isotopic labeling. *Anal Chem.* 84: 8549-8556.
61. Zumbusch A, Langbein W, Borri P (2013) Nonlinear vibrational microscopy applied to lipid biology. *Prog Lipid Res.* 52: 615-632.
62. DeLong JC, Hoffman RM, Bouvet M (2016) Current status and future perspectives of fluorescence-guided surgery for cancer. *Expert Rev Anticancer Ther.* 16: 71-81.
63. Allison RR (2016) Fluorescence guided resection (FGR): A primer for oncology. *Photodiagnosis Photodyn Ther.* 13: 73-80.
64. Notingher I, Verrier S, Romanska H, Bishop A, Polak J, Hench L (2002) In situ characterisation of living cells by Raman spectroscopy. *Spectroscopy.* 16: 43-51.
65. Jüngst C, Winterhalder MJ, Zumbusch A (2011) Fast and long term lipid droplet tracking with CARS microscopy. *J Biophotonics.* 4: 435-441.
66. Herms A, Bosch M, Ariotti N, Reddy BJN, Fajardo A, Fernández-Vidal A, Alvarez-Guaita A, Fernández-Rojo MA, Rentero C, Tebar F, Enrich C, Geli M-I, Parton RG, Gross SP, Pol A (2013) Cell-to-cell heterogeneity in lipid droplets suggests a mechanism to reduce lipotoxicity. *Curr Biol.* 23: 1489-1496.

67. Etzion Y, Hackett A, Proctor BM, Ren J, Nolan B, Ellenberger T, Muslin AJ (2009) An unbiased chemical biology screen identifies agents that modulate uptake of oxidized LDL by macrophages. *Circ Res.* 105: 148-157.
68. Schie IW, Wu J, Weeks T, Zern MA, Rutledge JC, Huser T (2011) Label-free imaging and analysis of the effects of lipolysis products on primary hepatocytes. *J Biophotonics.* 4: 425-434.
69. den Hartigh LJ, Connolly-Rohrbach JE, Fore S, Huser TR, Rutledge JC (2010) Fatty acids from very low-density lipoprotein lipolysis products induce lipid droplet accumulation in human monocytes. *J Immunol.* 184: 3927-3936.
70. Mayne ST, Cartmel B, Scarmo S, Jahns L, Ermakov IV, Gellermann W (2013) Resonance Raman spectroscopic evaluation of skin carotenoids as a biomarker of carotenoid status for human studies. *Arch Biochem Biophys.* 539: 163-170.
71. Verma SP, Philippot JR, Bonnet B, Sainte-Marie J, Moschetto Y, Wallach DF (1984) Resonance Raman spectra of beta-carotene in native and modified low-density lipoprotein. *Biochem Biophys Res Commun.* 122: 867-875.
72. Marshall CP, Olcott Marshall A (2010) The potential of Raman spectroscopy for the analysis of diagenetically transformed carotenoids. *Phil Trans R Soc A.* 368: 3137-3144.
73. Krafft C, Neudert L, Simat T, Salzer R (2005) Near infrared Raman spectra of human brain lipids. *Spectrochim Acta Mol Biomol Spectrosc.* 61: 1529-1535.

6 Publikationen

Im Folgenden sind die Nachdrucke der Publikationen aufgeführt, die für die vorliegende Dissertation berücksichtigt wurden.

- [CS1] Complexity of fatty acid distribution inside human macrophages on single cell level using Raman micro-spectroscopy
Clara Stiebing, Christian Matthäus, Christoph Krafft, Andrea-Anneliese Keller, Karina Weber, Stefan Lorkowski⁺, Jürgen Popp⁺ (2014)
Anal Bioanal Chem. 406:7037–7046.
- [CS2] Real-time Raman and SRS imaging of living human macrophages reveals cell-to-cell heterogeneity and dynamics of lipid uptake
Clara Stiebing, Tobias Meyer, Ingo Rimke, Christian Matthäus, Michael Schmitt, Stefan Lorkowski⁺, Jürgen Popp⁺ (2017)
J Biophotonics. DOI: 10.1002/jbio.201600279
- [CS3] Raman spectroscopic imaging of human macrophages incubated with triglyceride-enriched oxLDL visualizes translocation of lipids between endocytic vesicles and lipid droplets
Clara Stiebing, Lisa Schmölz, Maria Wallert, Christian Matthäus, Stefan Lorkowski⁺, Jürgen Popp⁺ (2017)
J Lipid Res. 58(5): 876–883.
- [CS4] Advantages and limitations of Raman spectroscopy for molecular diagnostics: an update.
Katharina Eberhardt^{*}, Clara Stiebing^{*}, Christian Matthäus, Michael Schmitt, Jürgen Popp (2015)
Expert Rev Mol Diagn. 15(6): 773–787.

^{*} geteilte Erstautorenschaft

⁺ gleichwertige Autorenschaft

6.1 Complexity of fatty acid distribution inside human macrophages on single cell level using Raman micro-spectroscopy [CS1]

Clara Stiebing, Christian Matthäus, Christoph Krafft, Andrea-Anneliese Keller, Karina Weber, Stefan Lorkowski⁺, Jürgen Popp⁺ (2014)

Anal Bioanal Chem. 406:7037–7046.

⁺gleichwertige Autorenschaft

Der Nachdruck der folgenden Publikation erscheint mit freundlicher Genehmigung von Springer.

Erklärung zu den Eigenanteilen der Promovendin sowie der weiteren Doktoranden/ Doktorandinnen als Koautoren an den Publikationen und Zweitpublikationsrechten bei einer kumulativen Dissertation.

| Doktoranden | Clara Stiebing | Andrea-Anneliese Keller |
|--|----------------|-------------------------|
| Konzeption des Forschungsansatzes | x | |
| Planung der Untersuchungen | x | |
| Datenerhebung | x | x |
| Datenanalyse und –interpretation | x | |
| Schreiben des Manuskripts | x | |
| Vorschlag Anrechnung Publikationsäquivalente | 1,0 | |

Anal Bioanal Chem (2014) 406:7037–7046
DOI 10.1007/s00216-014-7927-0

RESEARCH PAPER

Complexity of fatty acid distribution inside human macrophages on single cell level using Raman micro-spectroscopy

Clara Stiebing · Christian Matthäus · Christoph Krafft ·
Andrea-Anneliese Keller · Karina Weber ·
Stefan Lorkowski · Jürgen Popp

Received: 31 March 2014 / Revised: 26 May 2014 / Accepted: 26 May 2014 / Published online: 18 June 2014
© Springer-Verlag Berlin Heidelberg 2014

Abstract Macrophages are phagocytic cells which are involved in the non-specific immune defense. Lipid uptake and storage behavior of macrophages also play a key role in the development of atherosclerotic lesions within walls of blood vessels. The allocation of exogenous lipids such as fatty acids in the blood stream dictates the accumulation and quantity of lipids within macrophages. In case of an overexposure, macrophages transform into foam cells because of the large amount of lipid droplets in the cytoplasm. Raman micro-spectroscopy is a powerful tool for studying single cells due to the combination of microscopic imaging with spectral information. With a spatial resolution restricted by the diffraction limit, it is possible to visualize lipid droplets within macrophages. With stable isotopic labeling of fatty acids with deuterium, the uptake and storage of exogenously provided fatty acids can be investigated. In this study, we present the results of time-dependent Raman spectroscopic imaging of

single THP-1 macrophages incubated with deuterated arachidonic acid. The polyunsaturated fatty acid plays an important role in the cellular signaling pathway as being the precursor of icosanoids. We show that arachidonic acid is stored in lipid droplets but foam cell formation is less pronounced as with other fatty acids. The storage efficiency in lipid droplets is lower than in cells incubated with deuterated palmitic acid. We validate our results with gas chromatography and gain information on the relative content of arachidonic acid and its metabolites in treated macrophages. These analyses also provide evidence that significant amounts of the intracellular arachidonic acid is elongated to adrenic acid but is not metabolized any further. The co-supplementation of deuterated arachidonic acid and deuterated palmitic acid leads to a non-homogenous storage pattern in lipid droplets within single cells.

Keywords Macrophages · Lipid droplet · Arachidonic acid · Atherosclerosis · Gas chromatography · Raman spectroscopy

Stefan Lorkowski and Jürgen Popp contributed equally to this work.

Published in the topical collection *Single Cell Analysis* with guest editors Petra Dittrich and Norbert Jakubowski.

Electronic supplementary material The online version of this article (doi:10.1007/s00216-014-7927-0) contains supplementary material, which is available to authorized users.

C. Stiebing · C. Matthäus · C. Krafft · K. Weber · J. Popp (✉)
Leibniz Institute of Photonic Technology (IPHT),
Albert-Einstein-Straße 9, 07745 Jena, Germany
e-mail: juergen.popp@ipht-jena.de

C. Stiebing · C. Matthäus · C. Krafft · K. Weber · J. Popp
Institute of Physical Chemistry and Abbe Center of Photonics,
Friedrich Schiller University Jena, Helmholtzweg 4, 07743 Jena,
Germany

A.-A. Keller · S. Lorkowski
Institute of Nutrition and Abbe Center of Photonics, Friedrich
Schiller University Jena, Dornburger Straße 25, 07743 Jena,
Germany

Introduction

Macrophages are involved in the non-specific immune response. They take up various biological materials, such as lipids, bacteria or debris. Lipid uptake and storage behavior of macrophages play a key role in the development of atherosclerotic lesions within the walls of blood vessels. Macrophages are monocyte-derived cells which are often located in the subendothelial area of arteries in case of local damage or inflammation. Through receptor-mediated pathways, macrophages take up lipids complexed in lipoproteins as well as fatty acids bound to serum albumin in the blood stream. Both processes are uncontrolled leading to tremendous accumulation of lipids inside the cell in form of cytosolic lipid droplets. Eventually, extensive formation of lipid droplets leads to a

 Springer

foamy appearance of the cells, called foam cell formation, but also toxic levels are reached upon excessive uptake. Apoptosis or necrosis takes place and the excessive lipid content of the macrophage is released into the arterial walls, where the lipid depositions consequently form atherosclerotic plaques [1].

Lipid droplets are very interesting dynamic cellular organelles. Although plenty of research has been conducted, there are still various questions about the development and composition of lipid droplets [2, 3]. Many studies involve the incubation of different cell types with fatty acids, as for instance the saturated palmitic acid or monounsaturated oleic acid, to study their lipotoxicity and storage characteristics [4, 5]. Common methods to investigate lipid droplets are biochemical fractionation, gas chromatography, also combined with mass spectrometry, electron microscopy and fluorescence microscopy. Raman micro-spectroscopy, as a vibrational spectroscopic imaging method, has recently gained popularity to identify cells and study cellular processes [6–17]. A Raman spectrum is a representation of all chemical components present in the laser focus. With a spatial resolution restricted by the diffraction limit, Raman micro-spectroscopy provides the possibility to correlate the visual image of cells with chemical information.

Schie et al. evaluated the concentration of palmitic acid and oleic acid in lipid droplets by comparing Raman spectra of lipid droplets of hepatocytes to pure component spectra by using least square fitting algorithms [18]. Their results showed that asymmetric least square fitting is a very feasible possibility to analyze the content of individual lipid droplets in cells, which is independent of external labels. However, without any labeling, it is not possible to distinguish exogenously added fatty acids from the cell-intrinsic fatty acids. Macrophages, especially, can exhibit many lipid droplets under culture conditions in the presence of serum before any incubation and hence contain a variety of endogenous cellular lipids. To ascertain that a fatty acid is taken up by the cell and stored in lipid droplets, deuterium labels can be introduced [19–22]. Due to the higher mass of deuterium than hydrogen, deuterium-associated vibrational bands are shifted to lower wavenumbers compared to hydrogen bands. CH stretching vibrations exhibit spectral contributions around 2,800–3,100 cm^{-1} and significantly shift to 2,000–2,500 cm^{-1} through the exchange of hydrogen with deuterium. Therefore, CD stretching vibrations have spectral contributions within a normally silent region. Furthermore, band shifts of CD vibrations between pure spectra and lipid spectra inside of lipid droplets can be interpreted as a clear indication for structural changes.

With FTIR micro-spectroscopy, Gazi et al. studied the effect of deuterated palmitic acid, as well as deuterated arachidonic acid on exposed prostate cancer cells (PC-3) [23]. In an earlier study the group showed that PC-3 cells translocate lipids with adipocytes, which were previously incubated with

deuterated palmitic acid [24]. The study demonstrates nicely the power of isotopic labeling with deuterium by tracking the signal originating through deuterium bond vibrations. However, due to the longer wavelength used in FTIR micro-spectroscopy, the spatial resolution is inferior to Raman microscopy and single lipid droplets of non-adipocytes cannot be resolved.

Apparently, compositional parameters can have great influence on lipotoxicity. Co-supplementation studies by Listenberger et al. have been conducted using oleic acid and palmitic acid to investigate fatty acid induced cell death [4]. The study showed that in Chinese hamster ovary (CHO) cells, oleic acid channels palmitic acid to triglyceride storage when given supplementary. Solely added, incubation with palmitic acid caused apoptosis through lipotoxicity. It has been shown that triglyceride storage protects against lipotoxicity and that triglyceride accumulation is higher in cells treated with polyunsaturated fatty acids. These findings were confirmed by Martins de Lima et al. [5], who performed lipotoxicity tests on J774.A1 macrophages with different types of fatty acids including palmitic acid, oleic acid and arachidonic acid. These studies indicated that the toxicity of fatty acids is not strictly related to carbon-chain length and the number of double bonds.

The polyunsaturated arachidonic acid is an essential omega-6-fatty acid and acts as a bioactive molecule [25, 26]. It plays an important role for inflammatory signaling in cells as the precursor of eicosanoids. Arachidonic acid can be esterified and stored in cellular lipid compartments besides its use in phospholipids such as phosphatidylethanolamine, phosphatidylcholine, and phosphatidylinositides [27]. Van Manen et al. used deuterated arachidonic acid to investigate the association of lipid bodies with phagosomes in leukocytes [28]. They showed that incubation with arachidonic acid leads to esterified arachidonate in the lipid bodies near the phagocytized microspheres.

In this study, we present the results of time-dependent Raman spectroscopic imaging of single THP-1 macrophages incubated with deuterated arachidonic acid. Through data analyses with a spectral unmixing algorithm, we found that deuterated arachidonic acid is stored in lipid droplets but less efficiently than deuterated palmitic acid and oleic acid as previously shown [19]. The Raman spectroscopic imaging results were compared to gas chromatographic analyses. We observed a significant increase of arachidonic acid but also adrenic acid as the first two-carbon elongation product of arachidonic acid in the macrophages during the incubation process. The co-supplementation of deuterated arachidonic acid and palmitic acid lead to non-homogeneous storage in lipid droplets within a single cell. To the best of our knowledge, non-homogeneous storage patterns of two different types of fatty acids in lipid droplets of one cell have not yet been shown.

Material and methods

Cell culture

THP-1 monocytes (DSMZ, Braunschweig, Germany) have been cultured in RPMI 1640 medium (Sigma-Aldrich, St. Louis, MO) containing 10 % (v/v) fetal bovine serum superior (Biochrom, Berlin) and 1 % (v/v) penicillin/streptomycin/L-glutamine (Sigma-Aldrich) in an atmosphere of 5 % CO₂ at 37 °C. Monocytes have been differentiated into macrophages using RPMI 1640 medium supplemented with 100 ng/mL phorbol-12-myristate-13-acetate and 50 μM β-mercaptoethanol for 96 h as previously described [29, 30]. After differentiation, mature THP-1 macrophages were incubated for up to 32 h. Supplemented RPMI 1640 medium without serum was used with either 400 μM *d*₈-arachidonic acid or a mixture of 400 μM *d*₈-arachidonic acid and 400 μM *d*₃₁-palmitic acid (Sigma-Aldrich). Before incubation, the fatty acids were complexed to fatty acid-free bovine serum albumin (Sigma-Aldrich) at a molar ratio of 4:1 in Krebs-Ringer bicarbonate buffer. After incubation, cells were washed with phosphate buffered saline (PBS) and fixed with 4 % (w/v) paraformaldehyde in PBS for 20 min at room temperature.

Raman measurements

For Raman imaging, THP-1 macrophages were grown on calcium fluoride slides (Crystal, Berlin, Germany), in order to avoid disturbing background signals caused by common glass slides. Raman images were acquired using a confocal Raman Microscope Model alpha300 R (WITec, Ulm, Germany) and a Nikon water immersion objective with a magnification of ×60 and a numerical aperture of 1.00. An excitation wavelength of 785 nm was provided by a cw diode laser (Toptica Photonics, Gräfelfingen, Germany). Raman images were taken at a step size of 0.5 μm with an integration time of 0.5 s. Each pixel in an image represents one spectrum. If not declared otherwise, a grating of 300 grooves/mm was used, leading to a spectral resolution of around 6 cm⁻¹.

Data analysis of Raman measurements

All spectra were cleared from cosmic rays before analysis using the software CytoSpec (Cytospec, Berlin, Germany). Image analysis and spectral quantification was then performed in MatLab (MathWorks, Natick, MA). Baseline correction with a second order polynomial and vector normalization was implemented. Images acquired with Raman microspectroscopy were analyzed by the N-FINDR spectral unmixing algorithm described by Winter et al. [31, 32]. A wavenumber region from 500 to 3,100 cm⁻¹ was used. The quantification of *d*₈-arachidonic acid was performed by an

asymmetric least square fitting [33, 18]. A wavenumber region of 1,900 to 2,500 cm⁻¹ was chosen to evaluate the uptake of *d*₈-arachidonic acid through the deuterium signal in lipid droplets. Graphs were plotted and evaluated in Origin (OriginLab, Northampton, MA).

Gas chromatography

Lipids were extracted from mature THP-1 macrophages cultured for the times indicated in the figures with serum albumin-complexed fatty acids using a methanol/chloroform/water-mixture (2:1:1, v/v/v) according to the method of Bligh and Dyer [34]. Fatty acid methyl esters (FAME) were prepared with boron trifluoride in methanol (10 %, v/v; Supelco, Bellefonte, PA). Fatty acid analyses were conducted by gas chromatography using a Shimadzu GC-17V3 (Tokyo, Japan) equipped with auto sampler and flame ionization detector. Fatty acids ranging from 4 to 26 carbon atoms in length were determined using a fused silica capillary column (DB-225 ms: 60 m, i.d. 0.25 mm, 0.25 μm film thickness; Agilent Technologies, Böblingen, Germany). Analysis of *trans* fatty acids were conducted by a second measurement using a Shimadzu GC-2010 with flame ionization detector and a high polarity column (CP 7421: 200 m, i.d. 0.25 mm, 0.25 μm film thickness; Varian, Middelburg, the Netherlands). Various reference standards were used as FAME mix to verify the identity of fatty acid peaks: No. 463, 674 (NU-CHEK PREP, Elysian, MN), BR2, BR4, and ME 93 (Larodan, Sweden), Menhaden and several *cis/trans* standards (Supelco). Peaks of C24:4 (*n*-6) and C24:5 (*n*-6) were located by extrapolation as no standards were available. LabSolutions software for gas chromatography (GCsolution, Shimadzu, Japan) was used for peak integration. The measurements were recalculated with each other under consideration of the respective response factor. Fatty acid concentrations are expressed as percentage of the total area of all FA peaks (% of total FAME). The procedure was adapted from Kraft et al. [35].

Results and discussion

Uptake and storage of *d*₈-arachidonic acid by THP-1 macrophages

Figure 1a shows the Raman spectrum of pure *d*₈-arachidonic acid. The molecule is deuterated at eight positions as depicted in Fig. 1a. Deuterium labels are introduced at carbon atoms which feature a double bond. A specific signal between 2,100 and 2,300 cm⁻¹ appears due to =CD stretching vibrations in the usually silent region of non-deuterated fatty acid spectra. The spectrum is dominated by the band at 1,633 cm⁻¹ which corresponds to Raman scattering intensities of C=C bonds.

Due to the deuterium label, the band appears at a lower wavenumber instead of around $1,655\text{ cm}^{-1}$ reported for non-deuterated, unsaturated fatty acids [11, 28, 36].

The bright field image of a macrophage incubated with $400\text{ }\mu\text{M}$ d_8 -arachidonic acid complexed to serum albumin for 24 h is shown in Fig. 1b. The cytosolic lipid droplets are located close to the nucleus which contains a clearly visible nucleolus. Raman micro-spectroscopic images of treated cells were analyzed using the N-FINDR algorithm. The output spectra, usually referred to as endmembers, can be interpreted as spectra which represent the highest differences in the hyperspectral dataset. The number of used endmembers was chosen so that the protein and lipid composition could be differentiated. In average, this led to three endmembers—one corresponding to lipids, one to proteins and one to the cell surrounding background (see Electronic Supplementary Material Fig. S1). Using more endmembers proved to be not

beneficial, e.g., having more than one spectrum corresponding to lipids resulted only in a change of overall intensity. Therefore, the two main components represented by endmember spectra for the cell in Fig. 1b are the lipid (red) and protein (cyan) distribution within the cell (Fig. 1c), which were used to reconstruct the false-color image depicted in Fig. 1d. In the red spectrum, the deuterium signal is clearly visible between $2,100$ and $2,300\text{ cm}^{-1}$, providing evidence that d_8 -arachidonic acid is taken up and stored in lipid droplets of THP-1 macrophages. The fingerprint region between 500 and $2,000\text{ cm}^{-1}$ exhibits typical spectral characteristics of lipids and corresponds to a composition of different fatty acids within the lipid droplets. The shift of the C=C band from $1,633$ to $1,640\text{ cm}^{-1}$ and the C=O band of ester groups at $1,743\text{ cm}^{-1}$ that is not present in Fig. 1a indicate that non-deuterated lipids are also part of the lipid droplets in addition to deuterated arachidonic acid. Figure 1d shows the corresponding,

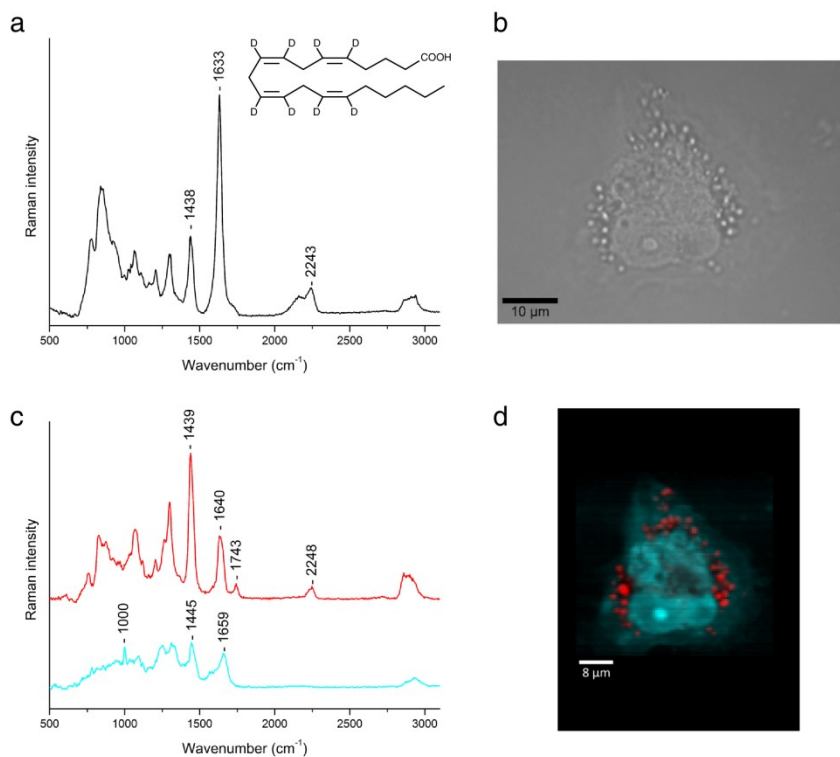


Fig. 1 a Chemical structure and Raman spectrum of pure d_8 -arachidonic acid. The spectral features between $2,100$ and $2,300\text{ cm}^{-1}$ originate from =CD stretching vibrations. b Bright field image of a THP-1 macrophage incubated with $400\text{ }\mu\text{M}$ d_8 -arachidonic acid complexed to serum albumin for 24 h. c Raman endmember spectra of the imaged cell in b after

applying the N-FINDR algorithm showing the lipid composition including the deuterium signal of d_8 -arachidonic acid in red and the protein composition in cyan. d Reconstructed cell image after N-FINDR analysis of b. The colors correspond to the endmember spectra in c

reconstructed image. The color intensity corresponds to the density and concentration of the plotted components. The nucleus and nucleolus are distinguishable due to the higher protein density compared to the cytoplasm. The lipid droplets with a diameter from 0.5 to 2 μm are clearly visible and colored in red. Smaller lipid accumulations are difficult to resolve due to the resolution limit.

Although arachidonic acid is a biologically active fatty acid, our results show clearly that it is stored in lipid droplets in case of excessive exposure of the cells. By enhancing the spectral resolution from approximately 6 to 3 cm^{-1} by using a grating of 600 grooves/mm, the band corresponding to C=C stretching vibrations features two maxima at 1,633 and 1,653 cm^{-1} (as shown below). This suggests that the double bonds of d_8 -arachidonic acid are not oxidized during their accumulation in lipid droplets.

To investigate the time-dependent uptake of d_8 -arachidonic acid into THP-1 macrophages different incubation times were chosen. Reconstructed cell images based on the N-FINDR analysis are shown in Fig. 2. The first column shows control cells which were fixed after the differentiation process without any incubation with fatty acids. Here, lipid droplets do not show deuterium signals (depicted in blue) and differ in quantity inside

individual cells. Monocytes cannot be synchronized in the way that they are in the same cell cycle phase before the differentiation process begins. Hence, macrophages show large inter-cell variability and already exhibit highly different amounts of lipid droplets prior to incubation with serum albumin-complexed fatty acids. After 3 h of incubation, a clear deuterium signal of the d_8 -arachidonic acid appears in the spectra corresponding to lipid droplets (depicted in red). A quantification of d_8 -arachidonic acid in lipid droplets was performed through an asymmetric least square fitting of the endmember spectra corresponding to lipids for each cell and time point compared to the pure d_8 -arachidonic acid spectrum. A wavenumber region between 1,900 and 2,500 cm^{-1} was chosen to only investigate bands originating from deuterium bond vibrations of d_8 -arachidonic acid. In the lower wavenumber region, overlapping spectral contributions of all fatty acids within a droplet are present. Figure 3 displays the results for all measured cells plotted over the incubation time. A rapid increase of d_8 -arachidonic acid in lipid droplets is occurring initially but after 3 h of incubation storage capacity is nearly exploited. Saturation is reached after 8 h. A high variation of the quantification for each time point was observed, which can be attributed to the non-synchronized cell cultivation protocol mentioned earlier.

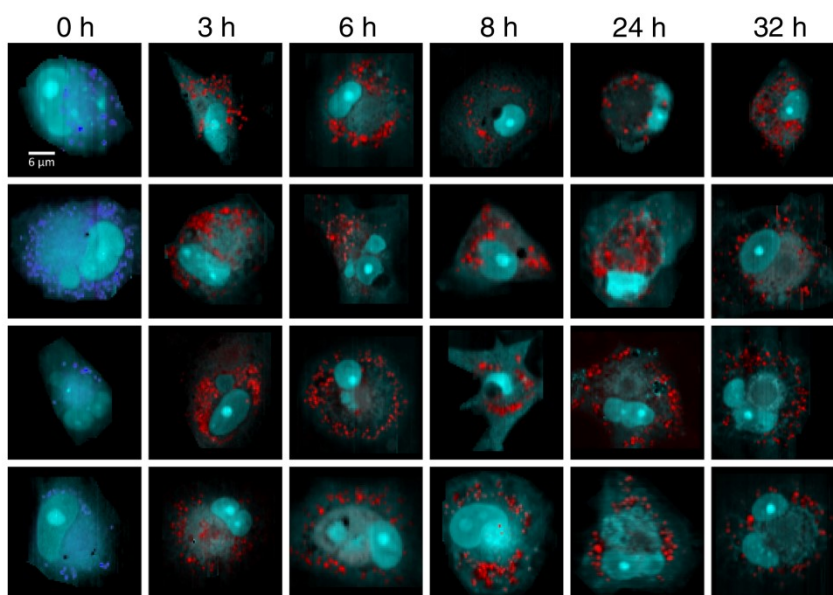


Fig. 2 Time-dependent series of incubated THP-1 macrophages with d_8 -arachidonic acid complexed to serum albumin at a concentration of 400 μM . The time points are indicated at the top of the columns. Images were reconstructed based on the lipid and protein endmember spectra

after N-FINDR analysis of the measured cells. At 0 h, no deuterium signals in the lipid component (*blue*) and hence no d_8 -arachidonic acid was detected. Over time, the deuterium signal in the lipid endmember spectra (*red*) is increasing. The protein distribution is depicted in *cyan*

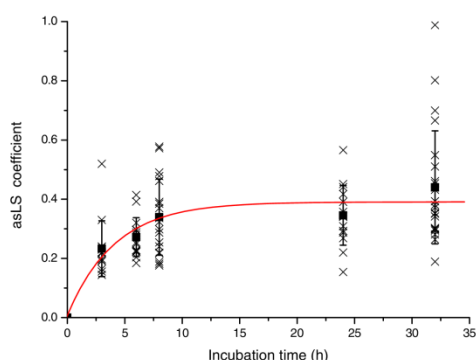


Fig. 3 Quantification of the uptake and storage of d_8 -arachidonic acid into lipid droplets over time using an asymmetric least square (*asLS*) fitting of the endmember spectra corresponding to lipids to the pure d_8 -arachidonic acid spectrum between 1,900 and 2,500 cm^{-1} . A quick uptake and storage in lipid droplets is detected. Saturation is reached after 8 h. *Cross* single cell measurement; *box* averaged value for each time point; *red line* fitted saturation curve

Over time, the content of d_8 -arachidonic acid in lipid droplets is increasing. However, no foam cell formation is visible as no apparent excess of lipid droplets inside the cell's cytoplasm occurs. This is in contrast to previous experiments conducted on saturated palmitic and unsaturated oleic acid, where clear foam cell formation was detected after 24 h of incubation [19]. The storage of arachidonic acid in lipid droplets is therefore less efficient. Our findings indicate that this fatty acid is not only stored in lipid droplets but also metabolized or subjected to other cellular compartments, for example, in form of phospholipids.

GC analysis of macrophages after arachidonic acid uptake

To confirm and extend the results obtained by Raman microspectroscopy, gas chromatographic analyses of THP-1 macrophages cultured in the presence of 400 μM arachidonic acid complexed to serum albumin for the times indicated in Fig. 4 were performed. In contrast to the Raman measurements, gas chromatography investigates bulk samples and therefore the total amount of cellular fatty acids without spatial information. In addition to the relative content of different types of fatty acids it is possible to obtain information on the metabolic fate of individual fatty acids, such as shortening by β -oxidation, elongation, and desaturation.

Figure 4 displays the relative content of arachidonic acid (C20:4) as well as its metabolic precursor dihomo- γ -linolenic acid (C20:3) and its metabolites adrenic acid (C22:4) and tetracosatetraenoic acid (C24:4) inside of arachidonic acid treated THP-1 macrophages. This information is supplemented by Table 1 which provides the numeric data shown in Fig. 4 plus data on the remaining fatty acids of the metabolic

pathway, namely the precursors linoleic acid (C18:2) and γ -linolenic acid (C18:3), and the metabolites tetracosapentaenoic acid (C24:5) and docosapentaenoic acid (C22:5). The total fatty acid content at each time point corresponds to 100 %. Chemical structures and the metabolic interactions between these fatty acids are displayed in Fig. 5. As expected, arachidonic acid is rapidly taken up by macrophages. Its cellular content increases steadily over time but slows down towards longer periods of incubation reaching a plateau after 12 h. After 24 h of incubation the relative cellular amount of arachidonic acid is about 50 %. In addition, a relevant increase of adrenic acid as the first two-carbon elongation product of arachidonic acid is also detected. Without reaching a plateau the cellular content of adrenic acid steadily increases up to nearly 16 % after 24 h whereas the cellular content of the next two-carbon elongation product tetracosatetraenoic acid increases only slightly. After 24 h its cellular content is less than 2 %. The subsequent metabolites likely produced by the pathway analogous to the Sprecher's shunt via desaturation (tetracosapentaenoic acid) and subsequent β -oxidation (docosapentaenoic acid) comprised each less than 0.1 % of the total cellular content.

Saturation of macrophage uptake of arachidonic acid is later than saturation of the storage of arachidonic acid in lipid droplets. This indicates that arachidonic acid is first stored in lipid droplets where saturation is reached after 8 h. For longer incubation times, the fatty acid is more likely incorporated into phospholipids of cell and organelle membranes. Raman spectroscopy only allows identifying components of a certain local concentration and size. Single arachidonic acid

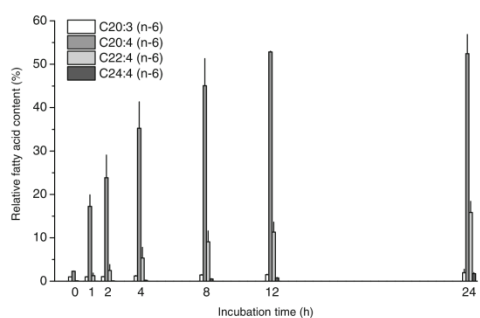


Fig. 4 Time-dependent results of THP-1 macrophages incubated with 400 μM arachidonic acid (C20:4) obtained by gas chromatography. The relative fatty acid content of arachidonic acid (C20:4) and its metabolic precursor dihomo- γ -linolenic acid (C20:3) and its metabolites adrenic acid (C22:4) and tetracosatetraenoic acid (C24:4) are displayed. The total fatty acid content at each time point corresponds to 100 %. A rapid increase of relative arachidonic acid content inside of macrophages is observed and saturation is reached after 12 h. Adrenic acid as the first two-carbon elongation product of arachidonic acid appears during the incubation with arachidonic acid and reaches 16 % of relative fatty acid content in the cells after 24 h. Numeric data is provided in Table 1

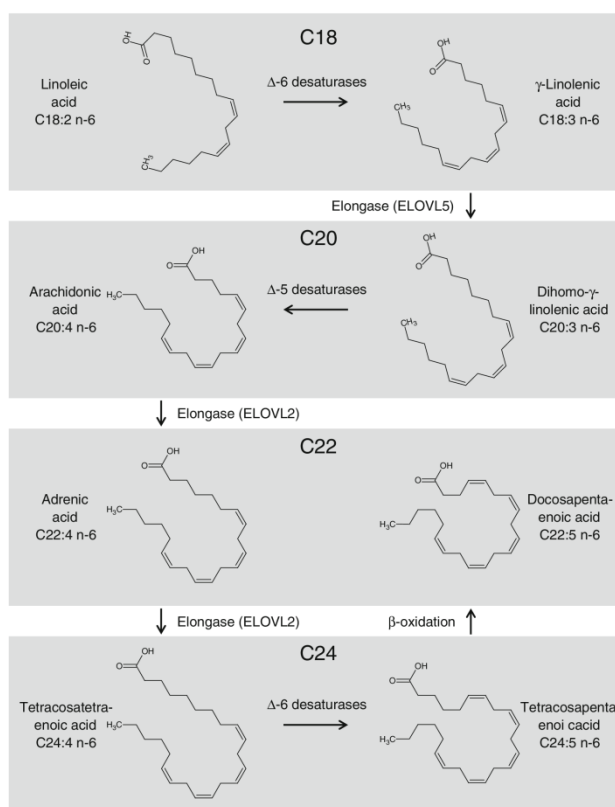
Table 1 Percentage of total fatty acid content in THP-1 macrophages after different times of incubation with 400 μ M arachidonic acid complexed to serum albumin obtained by gas chromatography. Only fatty acids metabolized from arachidonic acid and directed to the Sprecher's shunt as well as the metabolic precursors of arachidonic acid are shown

| <i>s</i> | <i>n</i> -6 | 0 h | 1 h | 2 h | 4 h | 8 h | 12 h | 24 h |
|----------------------------------|-------------------------------------|-----------------|------------------|------------------|------------------|------------------|------------------|------------------|
| Linoleic acid | C18:2 all- <i>cis</i> -9,12 | 1.45 \pm 0.13 | 1.29 \pm 0.08 | 1.17 \pm 0.01 | 0.94 \pm 0.02 | 0.71 \pm 0.07 | 0.56 \pm 0.00 | 0.46 \pm 0.03 |
| γ -Linolenic acid | C18:3 all- <i>cis</i> -6,9,12 | 0.00 \pm 0.00 | 0.08 \pm 0.01 | 0.11 \pm 0.03 | 0.17 \pm 0.04 | 0.24 \pm 0.06 | 0.32 \pm 0.02 | 0.49 \pm 0.05 |
| Dihomo- γ -linolenic acid | C20:3 all- <i>cis</i> -8,11,14 | 1.00 \pm 0.03 | 1.02 \pm 0.07 | 1.05 \pm 0.06 | 1.20 \pm 0.15 | 1.43 \pm 0.11 | 1.50 \pm 0.11 | 1.94 \pm 0.81 |
| Arachidonic acid | C20:4 all- <i>cis</i> -5,8,11,14 | 2.28 \pm 0.06 | 17.24 \pm 2.68 | 23.83 \pm 5.24 | 35.25 \pm 6.07 | 45.04 \pm 6.26 | 52.84 \pm 0.18 | 52.45 \pm 4.42 |
| Adrenic acid | C22:4 all- <i>cis</i> -7,10,13,16 | 0.11 \pm 0.03 | 1.26 \pm 0.60 | 2.47 \pm 1.37 | 5.33 \pm 2.48 | 9.08 \pm 2.52 | 11.30 \pm 2.32 | 15.85 \pm 2.58 |
| Tetracosatetraenoic acid | C24:4 all- <i>cis</i> -9,12,15,18 | 0.00 \pm 0.00 | 0.03 \pm 0.00 | 0.05 \pm 0.02 | 0.21 \pm 0.09 | 0.52 \pm 0.09 | 0.77 \pm 0.10 | 1.73 \pm 0.25 |
| Tetracosapentaenoic acid | C24:5 all- <i>cis</i> -6,9,12,15,18 | 0.00 \pm 0.00 | 0.00 \pm 0.00 | 0.00 \pm 0.00 | 0.00 \pm 0.00 | 0.01 \pm 0.01 | 0.01 \pm 0.01 | 0.03 \pm 0.03 |
| Docosapentaenoic acid | C22:5 all- <i>cis</i> -4,7,10,13,16 | 0.03 \pm 0.01 | 0.02 \pm 0.02 | 0.02 \pm 0.03 | 0.01 \pm 0.02 | 0.02 \pm 0.01 | 0.02 \pm 0.02 | 0.03 \pm 0.01 |

molecules or the arachidonic acid-containing phospholipids in cellular membranes cannot be detected by Raman micro-spectroscopic imaging. Further investigations have to be conducted whether arachidonic acid is stored unaltered in lipid

droplets or rather elongated and stored as adrenic acid. The reason for the elongation may be that it is energetically more favorable to store longer fatty acid chains or that it protects the cells from an overexposure with arachidonic acid thus

Fig. 5 Chemical structures of the fatty acids listed in Table 1 including their metabolic interactions. The number of carbon atoms increases downwards. Arrows depict the interactions between the fatty acids



hindering an overproduction of icosanoids. Comai et al. investigated isolated lipid droplets from rabbit renal medullary tissue and showed that adrenic and arachidonic acid are both present as triglycerides in cytosolic lipid droplets [37]. The difference of two carbons does not change the chemical structure sufficiently to detect intensity or wavenumber variations in Raman spectra between adrenic and arachidonic acid and we therefore cannot deduce which type of fatty acid is more prominent in lipid droplets.

Colocalization of d_8 -arachidonic acid and d_{31} -palmitic acid in THP-1 macrophages

For Raman measurements, THP-1 macrophages were treated simultaneously with d_8 -arachidonic acid and d_{31} -palmitic acid to investigate the intracellular distribution patterns of the two different types of fatty acids. The fatty acids were again complexed to serum albumin and cells were incubated with

a concentration of 400 μM each. These two fatty acids were chosen because they are different with respect to their cellular function. While arachidonic acid is bioactive and a precursor to inflammatory molecules such as prostaglandins, palmitic acid is a storage molecule and acts as a precursor for the synthesis of longer fatty acid chains. The previous analyses revealed that uptake and storage efficiency of arachidonic acid in lipid droplets compared to palmitic acid or oleic acid is quite different.

Figure 6a depicts the Raman spectrum of a lipid droplet of a cell (red) incubated for 24 h with polyunsaturated d_8 -arachidonic and saturated d_{31} -palmitic acid that is overlaid by the pure spectra of d_8 -arachidonic (black) and d_{31} -palmitic acid (green). Both fatty acids are stored in lipid droplets alongside each other. Because of the different types of deuterium labels of the two fatty acids ($=\text{CD}$ vs. CD), it is possible to differentiate between the signals originating from the d_{31} -palmitic acid (2,100 and 2,197 cm^{-1}) and the one from d_8 -arachidonic

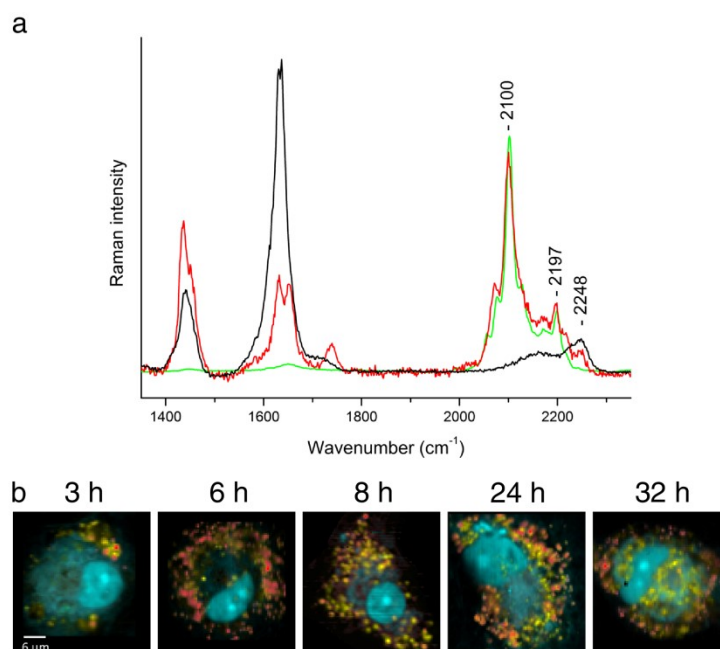


Fig. 6 **a** Raman spectrum of a lipid droplet of a cell (red) incubated for 24 h with both 400 μM d_8 -arachidonic acid and 400 μM d_{31} -palmitic acid complexed to serum albumin overlaid by the pure spectra of d_8 -arachidonic acid (black) and d_{31} -palmitic acid (green). Bands at 2,100 and 2,197 cm^{-1} in the red spectrum can be assigned to d_{31} -palmitic acid, the band at 2,248 cm^{-1} to d_8 -arachidonic acid. Two bands of $\text{C}=\text{C}$ vibrations are observed at 1,633 cm^{-1} and 1,653 cm^{-1} originating from deuterated and non-deuterated, unsaturated fatty acids as explained earlier. For better

spectral resolution, a grating of 600 grooves/mm was used, leading to a spectral resolution of approximately 3 cm^{-1} . **b** Reconstructed images of THP-1 macrophages with two lipid and one protein endmember spectra for different time points. Red corresponds to lipid droplets which feature deuterium signals of d_8 -arachidonic acid and d_{31} -palmitic acid, yellow to lipid droplets which only feature deuterium signals of d_{31} -palmitic acid and cyan displays protein density

acid ($2,248\text{ cm}^{-1}$). Since d_{31} -palmitic acid is deuterated at all carbon atoms along the alkyl chain, the signal is more intense than that of d_8 -arachidonic acid. Furthermore, the signal originating from the $=\text{CD}$ vibrations of the d_8 -arachidonic acid is associated with a sp^2 -hybridization, which exhibits less intense Raman signals compared to the sp^3 -hybridized CD bonds of the d_{31} -palmitic acid.

In the presence of both fatty acids, macrophages transformed rapidly into foam cells due to the high amount of lipid droplets inside the cells (Fig. 6b). Interestingly, the storage distribution of the two fatty acids inside the same cell is not homogeneous. In the early phase of incubation, d_8 -arachidonic acid is present only in a few lipid droplets. In contrast, d_{31} -palmitic acid is immediately distributed over the whole cell after starting the incubation and is detected in almost all lipid droplets within a cell independent of the incubation time. The amount of lipid droplets which feature d_8 -arachidonic acid is increasing over time but not quantifiable due to high differences between cells incubated for the same time. For long incubation times higher than 24 h, the majority of lipid droplets surrounding the nucleus are comprised only by d_{31} -palmitic acid. Figure 6b exemplary shows reconstructed N-FINDR images of THP-1 macrophages incubated with the two fatty acids for different time points. On average, four endmembers for each cell were investigated (see Electronic Supplementary Material Fig. S2). Two lipid endmembers, one with both d_8 -arachidonic acid and d_{31} -palmitic acid (red) and one with just d_{31} -palmitic acid (yellow), and one endmember showing the protein distribution (cyan) are depicted. The corresponding red lipid endmember spectrum shows a distinct band at $2,248\text{ cm}^{-1}$, which is not detectable in the yellow endmember spectrum representing d_{31} -palmitic acid. d_8 -Arachidonic acid is therefore stored in different concentrations in lipid droplets within one cell if d_{31} -palmitic acid is present. This is in contrast to its storage in all lipid droplets in the case of macrophages solely incubated with d_8 -arachidonic acid.

Conclusions

In this study, we have presented the uptake and storage behavior of arachidonic acid in human macrophages. By using Raman micro-spectroscopy and deuterium-labeled arachidonic acid, we were able to trace exogenously provided arachidonic acid within cytosolic lipid droplets in macrophages. Spectral analyses revealed that the bulk of the fatty acid is not subjected to β -oxidation following uptake. This was confirmed by gas chromatography measurements, which also revealed that arachidonic acid is

elongated to adrenic acid in significant amounts. Our results show that macrophages quickly store arachidonic acid in lipid droplets in case of excessive exposure. Saturation is reached after 8 h of incubation. The increased cellular accumulation of arachidonic acid after 8 h as discovered by gas chromatography in contrast to the saturation of its storage in lipid droplets suggests that in late periods of incubation the fatty acid may be stored mostly in membrane phospholipids rather than in lipid droplet storage organelles. However, our data also provide evidence that free arachidonic acid is also converted at least in part into adrenic acid by two-carbon elongation before integration into lipid droplets or phospholipids. This biologically relevant observation indicates that the immediate storage in lipid droplets after uptake may be a protective mechanism against lipotoxicity that is overwhelmed at later stages. However, the reasons for the more limited capability for storing arachidonic acid in contrast to the larger ability to store palmitic acid or oleic acid needs to be unraveled. In contrast to arachidonic acid, palmitic acid is stored predominantly in lipid droplets [19], whereas arachidonic acid may also be metabolized to phospholipids [38], which cannot be located by Raman micro-spectroscopy.

Co-supplementation studies with both fatty acids were also performed. Through their distinctive deuterium signals, we were able to distinguish their subcellular distribution in macrophages. Clear foam cell formation for long incubation times was detected and a non-homogenous storage pattern in lipid droplets is obvious. In contrast to palmitic acid, arachidonic acid is not stored homogeneously in all lipid droplets.

Raman micro-spectroscopy proved to be a powerful tool to spatially resolve and investigate the chemical compositions of a single cell. This allows studying not only the distribution and quantity of lipid droplets on single cell level but also the location of exogenously provided fatty acids. As a non-destructive and non-invasive method, it also enables future in vivo studies. These are advantages compared to common methods which are based on bulk samples. However, gas chromatography provides additional chemical information as to the presence of other fatty acids in the cells such as precursors and metabolites. Only through the combination of several different methods like Raman micro-spectroscopy and gas chromatography will it be possible to fully understand the molecular processes in cells.

Acknowledgments We thank Carsten Rohrer for conducting the GC measurements, Maria Wallert and Lisa Schmözl for the introduction into the cell culture work and Dr. Iwan W. Schie for helpful discussions. We gratefully acknowledge the financial support by the Carl Zeiss Stiftung and the "Jenaer Biochip Initiative 2.0" (JBCI 2.0). The project "JBCI 2.0" (03IPT513Y) within the framework "InnoProfile-Transfer-Unternehmen Region" is supported by the Federal Ministry of Education and Research (BMBF), Germany.

References

- Lorkowski S, Cullen P (2007) *Atherosclerosis: pathogenesis, clinical features and treatment*. Wiley, Chichester
- Ohsaki Y, Suzuki M, Fujimoto T (2014) Open questions in lipid droplet biology. *Chem Biol* 21:86–96
- Melo RC, D'Avila H, Wan HC, Bozza PT, Dvorak AM, Weller PF (2011) Lipid bodies in inflammatory cells: structure, function, and current imaging techniques. *J Histochem Cytochem* 59:540–556
- Listenberger LL, Han X, Lewis SE, Cases S, Farese RV Jr, Ory DS, Schaffer JE (2003) Triglyceride accumulation protects against fatty acid-induced lipotoxicity. *Proc Natl Acad Sci U S A* 100:3077–3082
- Martins de Lima T, Cury-Boaventura MF, Giannocco G, Nunes MT, Curi R (2006) Comparative toxicity of fatty acids on a macrophage cell line (J774). *Clin Sci* 111:307–317
- Diem M, Mazur A, Lenau K, Schubert J, Bird B, Miljkovic M, Krafft C, Popp J (2013) Molecular pathology via IR and Raman spectral imaging. *J Biophotonics* 6:855–886
- Krafft C, Dietzek B, Popp J (2009) Raman and CARS microspectroscopy of cells and tissues. *Analyst* 134:1046–1057
- Lattermann A, Matthäus C, Bergner N, Beleites C, Romeike BF, Krafft C, Brehm BR, Popp J (2013) Characterization of atherosclerotic plaque depositions by Raman and FTIR imaging. *J Biophotonics* 6:110–121
- Wu H, Volponi JV, Oliver AE, Parikh AN, Simmons BA, Singh S (2011) In vivo lipidomics using single-cell Raman spectroscopy. *Proc Natl Acad Sci U S A* 108:3809–3814
- Matthäus C, Dochow S, Bergner G, Lattermann A, Romeike BF, Marple ET, Krafft C, Dietzek B, Brehm BR, Popp J (2012) In vivo characterization of atherosclerotic plaque depositions by Raman-probe spectroscopy and in vitro coherent anti-stokes Raman scattering microscopic imaging on a rabbit model. *Anal Chem* 84:7845–7851
- Krafft C, Neudert L, Simat T, Salzer R (2005) Near infrared Raman spectra of human brain lipids. *Spectrochim Acta A Mol Biomol Spectrosc* 61:1529–1535
- Neugebauer U, Bocklitz T, Clement JH, Krafft C, Popp J (2010) Towards detection and identification of circulating tumour cells using Raman spectroscopy. *Analyst* 135:3178–3182
- Dochow S, Krafft C, Neugebauer U, Bocklitz T, Henkel T, Mayer G, Albert J, Popp J (2011) Tumour cell identification by means of Raman spectroscopy in combination with optical traps and microfluidic environments. *Lab Chip* 11:1484–1490
- Hedegaard M, Krafft C, Ditzel HJ, Johansen LE, Hassing S, Popp J (2010) Discriminating isogenic cancer cells and identifying altered unsaturated fatty acid content as associated with metastasis status, using k-means clustering and partial least squares-discriminant analysis of Raman maps. *Anal Chem* 82:2797–2802
- Chan JW (2013) Recent advances in laser tweezers Raman spectroscopy (LTRS) for label-free analysis of single cells. *J Biophotonics* 6:36–48
- Kirchner SR, Ohlinger A, Pfeiffer T, Urban AS, Stefani FD, Deak A, Lutich AA, Feldmann J (2012) Membrane composition of jetted lipid vesicles: a Raman spectroscopy study. *J Biophotonics* 5:40–46
- Matthäus C, Schubert S, Schmitt M, Krafft C, Dietzek B, Schubert US, Popp J (2013) Resonance Raman spectral imaging of intracellular uptake of beta-carotene loaded poly(D, L-lactide-co-glycolide) nanoparticles. *ChemPhysChem* 14:155–161
- Schie IW, Nolte L, Pedersen TL, Smith Z, Wu J, Yahiatene I, Newman JW, Huser T (2013) Direct comparison of fatty acid ratios in single cellular lipid droplets as determined by comparative Raman spectroscopy and gas chromatography. *Analyst* 138:6662–6670
- Matthäus C, Krafft C, Dietzek B, Brehm BR, Lorkowski S, Popp J (2012) Noninvasive imaging of intracellular lipid metabolism in macrophages by Raman microscopy in combination with stable isotopic labeling. *Anal Chem* 84:8549–8556
- Caruso D, Rise P, Galella G, Regazzoni C, Toia A, Galli G, Galli C (1994) Formation of 22 and 24 carbon 6-desaturated fatty acids from exogenous deuterated arachidonic acid is activated in THP-1 cells at high substrate concentrations. *FEBS Lett* 343:195–199
- Slipchenko MN, Le TT, Chen H, Cheng JX (2009) High-speed vibrational imaging and spectral analysis of lipid bodies by compound Raman microscopy. *J Phys Chem B* 113:7681–7686
- Brash AR, Ingram CD (1986) Lipoxygenase metabolism of endogenous and exogenous arachidonate in leukocytes: GC-MS analyses of incubations in H₂(18)O buffers. *Prostaglandins Leukot Med* 23:149–154
- Gazi E, Harvey TJ, Brown MD, Lockyer NP, Gardner P, Clarke NW (2009) A FTIR microspectroscopic study of the uptake and metabolism of isotopically labelled fatty acids by metastatic prostate cancer. *Vib Spectrosc* 50:99–105
- Gazi E, Gardner P, Lockyer NP, Hart CA, Brown MD, Clarke NW (2007) Direct evidence of lipid translocation between adipocytes and prostate cancer cells with imaging FTIR microspectroscopy. *J Lipid Res* 48:1846–1856
- Brash AR (2001) Arachidonic acid as a bioactive molecule. *J Clin Invest* 107:1339–1345
- Spector AA (1999) Essentiality of fatty acids. *Lipids* 34(Suppl):S1–S3
- Perez R, Matabosch X, Llebaria A, Balboa MA, Balsinde J (2006) Blockade of arachidonic acid incorporation into phospholipids induces apoptosis in U937 promonocytic cells. *J Lipid Res* 47:484–491
- van Manen HJ, Kraan YM, Roos D, Otto C (2005) Single-cell Raman and fluorescence microscopy reveal the association of lipid bodies with phagosomes in leukocytes. *Proc Natl Acad Sci U S A* 102:10159–10164
- Schnoor M, Cullen P, Lorkowski J, Stolle K, Robenek H, Troyer D, Rauterberg J, Lorkowski S (2008) Production of type VI collagen by human macrophages: a new dimension in macrophage functional heterogeneity. *J Immunol* 180:5707–5719
- Schnoor M, Buers I, Sietmann A, Brodde MF, Hofnagel O, Robenek H, Lorkowski S (2009) Efficient non-viral transfection of THP-1 cells. *J Immunol Methods* 344:109–115
- Winter ME (1999) N-FINDR: an algorithm for fast autonomous spectral end-member determination in hyperspectral data. *Proc SPIE* 3753:266–275
- Hedegaard M, Matthäus C, Hassing S, Krafft C, Diem M, Popp J (2011) Spectral unmixing and clustering algorithms for assessment of single cells by Raman microscopic imaging. *Theor Chem Acc* 130:1249–1260
- Boelens HF, Dijkstra RJ, Eilers PH, Fitzpatrick F, Westerhuis JA (2004) New background correction method for liquid chromatography with diode array detection, infrared spectroscopic detection and Raman spectroscopic detection. *J Chromatogr A* 1057:21–30
- Bligh EG, Dyer WJ (1959) A rapid method of total lipid extraction and purification. *Can J Biochem Physiol* 37:911–917
- Kraft J, Collomb M, Mockel P, Sieber R, Jahreis G (2003) Differences in CLA isomer distribution of cow's milk lipids. *Lipids* 38:657–664
- Chan JW, Motton D, Rutledge JC, Keim NL, Huser T (2005) Raman spectroscopic analysis of biochemical changes in individual triglyceride-rich lipoproteins in the pre- and postprandial state. *Anal Chem* 77:5870–5876
- Comai K, Farber SJ, Paulsrud JR (1975) Analyses of renal medullary lipid droplets from normal, hydronephrotic, and indomethacin treated rabbits. *Lipids* 10:555–561
- Guijas C, Astudillo AM, Gil-de-Gomez L, Rubio JM, Balboa MA, Balsinde J (2012) Phospholipid sources for adrenergic acid mobilization in RAW 264.7 macrophages. Comparison with arachidonic acid. *Biochim Biophys Acta* 1821:1386–1393

Journal of Analytical and Bioanalytical Chemistry

**Complexity of Fatty Acid Distribution inside Human
Macrophages on Single Cell Level Using
Raman Micro-Spectroscopy**

Supplementary Material

**Clara Stiebing^{1,2}, Christian Matthäus^{1,2}, Christoph Krafft^{1,2}, Andrea-Anneliese Keller³,
Karina Weber^{1,2}, Stefan Lorkowski^{3,*}, Jürgen Popp^{1,2,*}**

¹Leibniz Institute of Photonic Technology (IPHT), Albert-Einstein-Straße 9, 07745 Jena, Germany

²Institute of Physical Chemistry and Abbe Center of Photonics, Friedrich Schiller University Jena,
Helmholtzweg 4, 07743 Jena, Germany

³Institute of Nutrition and Abbe Center of Photonics, Friedrich Schiller University Jena, Dornburger
Straße 25, 07743 Jena, Germany

* Both authors contributed equally

Corresponding author:

Prof. Dr. Jürgen Popp
Leibniz Institute of Photonic Technology (IPHT)
Albert-Einstein-Straße 9
07745 Jena
Germany
E-Mail: juergen.popp@ipht-jena.de
Tel.: +49 3641-206 300
Fax: +49 3641-206 399

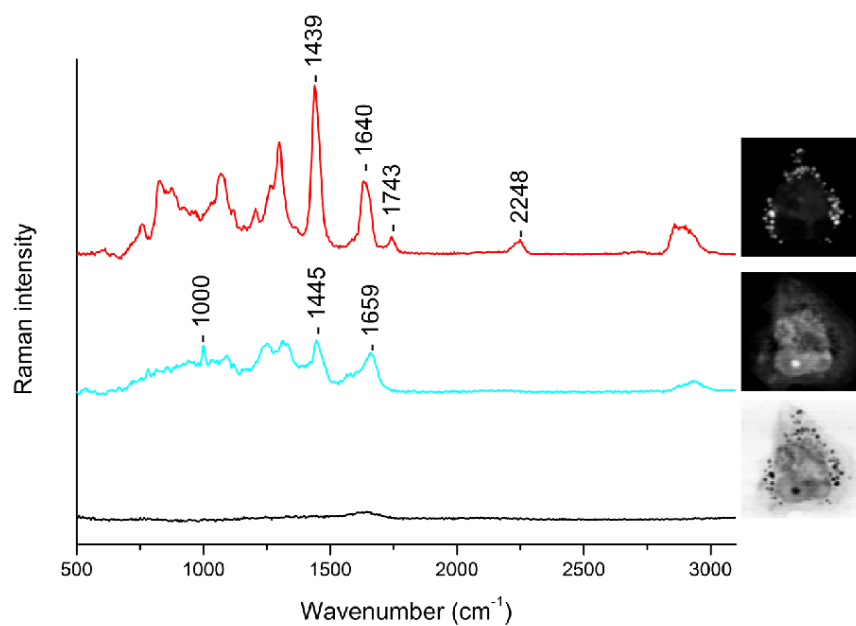


Fig. S1 All obtained endmember spectra after applying the N-FINDR algorithm on the Raman image of a THP-1 macrophage incubated with d_8 -arachidonic acid for 24 h. Depicted in red is the endmember corresponding to the lipid composition of the cell which exhibit the deuterium signal of d_8 -arachidonic acid at 2248 cm^{-1} originating from the $=\text{CD}$ stretching vibrations. The endmember spectrum in cyan represents the protein composition and the endmember in black the water background surrounding the cell. The corresponding distribution in the cell is depicted on the right side of each spectrum. The bright field image of the cell is shown in Figure 1 of the manuscript as well as an image of the composition of the upper two endmembers.

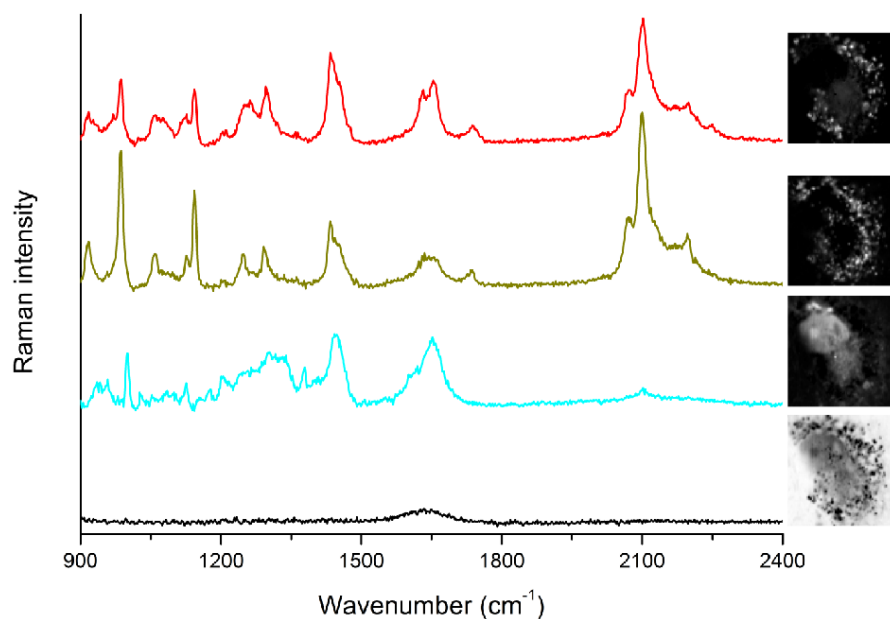


Fig. S2 All obtained endmember spectra after applying the N-FINDR algorithm on the Raman image of a THP-1 macrophage incubated with d_8 -arachidonic acid and d_{31} -palmitic acid for 24 h. The red endmember corresponds to lipid droplets which exhibit deuterium signals of d_8 -arachidonic acid (2248 cm^{-1}) and d_{31} -palmitic acid (2100 and 2177 cm^{-1}), the yellow endmember to lipid droplets which only exhibit deuterium signals of d_{31} -palmitic acid. The endmember spectrum in cyan represents the protein composition. A band at 2100 cm^{-1} is visible in the protein component originating from the most intense peak of the CD vibrations of d_{31} -palmitic acid. This is due to the high amount of lipid droplets inside of the cell and was only observed for cells after long incubation times, which were in foam cell formation. The endmember in black displays the water background surrounding the cell. The corresponding distribution in the cell is depicted on the right side of each spectrum. The cell is shown in Figure 6 of the manuscript as a composition of the upper three endmembers.

6.2 Real-time Raman and SRS imaging of living human macrophages reveals cell-to-cell heterogeneity and dynamics of lipid uptake [CS2]

Clara Stiebing, Tobias Meyer, Ingo Rimke, Christian Matthäus, Michael Schmitt, Stefan Lorkowski⁺, Jürgen Popp⁺ (2017)

J Biophotonics. DOI: 10.1002/jbio.201600279

⁺gleichwertige Autorenschaft

Der Nachdruck der folgenden Publikation erscheint mit freundlicher Genehmigung von John Wiley and Sons.

Erklärung zu den Eigenanteilen der Promovendin sowie der weiteren Doktoranden/ Doktorandinnen als Koautoren an den Publikationen und Zweitpublikationsrechten bei einer kumulativen Dissertation.

| Doktoranden | Clara Stiebing |
|--|----------------|
| Konzeption des Forschungsansatzes | x |
| Planung der Untersuchungen | x |
| Datenerhebung | x |
| Datenanalyse und –interpretation | x |
| Schreiben des Manuskripts | x |
| Vorschlag Anrechnung Publikationsäquivalente | 1,0 |

FULL ARTICLE

Real-time Raman and SRS imaging of living human macrophages reveals cell-to-cell heterogeneity and dynamics of lipid uptake

Clara Stiebing^{1,2}, Tobias Meyer^{1,2}, Ingo Rimke³, Christian Matthäus^{1,2}, Michael Schmitt², Stefan Lorkowski^{*,4,5}, and Jürgen Popp^{*,**}, 1,2

¹ Leibniz Institute of Photonic Technology (IPHT), Albert-Einstein-Straße 9, 07745 Jena, Germany

² Institute of Physical Chemistry and Abbe Center of Photonics, Friedrich Schiller University Jena, Helmholtzweg 4, 07743 Jena, Germany

³ APE Angewandte Physik & Elektronik GmbH, Plauener Straße 163–165, 13053 Berlin

⁴ Institute of Nutrition and Abbe Center of Photonics, Friedrich Schiller University Jena, Dornburger Straße 25, 07743 Jena, Germany

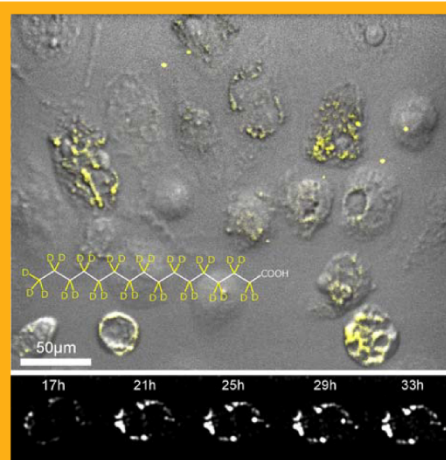
⁵ Competence Cluster of Nutrition and Cardiovascular Health (nutriCARD), Halle-Jena-Leipzig, Friedrich Schiller University Jena, Dornburger Straße 25, 07743 Jena, Germany

Received 1 November 2016, revised 23 December 2016, accepted 18 January 2017

Published online 7 February 2017

Key words: Monocyte-derived macrophages, lipid droplet, isotope labeling, palmitic acid, coherent Raman imaging, stimulated Raman scattering

Monitoring living cells in real-time is important in order to unravel complex dynamic processes in life sciences. In particular the dynamics of initiation and progression of degenerative diseases is intensely studied. In atherosclerosis the thickening of arterial walls is related to high lipid levels in the blood stream, which trigger the lipid uptake and formation of droplets as neutral lipid reservoirs in macrophages in the arterial wall. Unregulated lipid uptake finally results in foam cell formation, which is a hallmark of atherosclerosis. In previous studies, the uptake and storage of different fatty acids was monitored by measuring fixed cells. Commonly employed fluorescence staining protocols are often error prone because of cytotoxicity and unspecific fluorescence backgrounds. By following living cells with Raman spectroscopic imaging, lipid uptake of macrophages was studied with real-time data acquisition. Isotopic labeling using deuterated palmitic acid has been combined with spontaneous and stimulated Raman imaging to investigate the dynamic process of fatty acid storage in human macrophages for incubation times from 45 min to 37 h. Striking heterogeneity in the uptake rate and the total concentration of deuterated palmitic acid covering two orders of magnitude is detected in single as well as ensembles of cultured human macrophages.



SRS signal of deuterated palmitic acid measured at the CD vibration band after incorporation into living macrophages.

* Corresponding author: e-mail: juergen.popp@leibniz-ipht.de, Phone: +49 3641 206300, Fax: +49 3641 206399

** These authors contributed equally to this work.

1. Introduction

The increase of degenerative diseases is a threat for everyone and represents a financial burden for the health care systems of ageing societies. Early disease detection does significantly improve the patient prognosis, since changes in lifestyle can efficiently slow or even prevent the progression of disease. Cardiovascular diseases are the major cause of death in the world [1].

Atherosclerosis is the most prominent among the diverse group of cardiovascular diseases [2]. This chronic inflammatory disease process evolves for decades before first symptoms are noticed and causes myocardial infarction or stroke in the worst case. It is believed that progression of atherosclerosis is promoted by high lipid levels in the blood stream, which trigger the lipid uptake and formation of lipid droplets in macrophages of the arterial wall. The process finally results in foam cell formation when lipid droplets fill the cytoplasm, a stage at which the increased lipid concentrations can become cytotoxic. Subsequent cell death and the remaining cellular debris can substantially contribute to plaque depositions at the inner walls of arteries. Foam cell formation represents an early hallmark of atherosclerosis [3]. Hence the process of foam cell formation itself is of particular interest to study atherogenesis. In previous studies, the cellular uptake and storage of different fatty acids was quantified by measuring fixed cells using fluorescence staining [4–7]. Fixative staining methods provide reproducible data, but are prone to errors mainly due to non-specific staining of other cellular structures and to some extent the interference of autofluorescent species. Most staining agents are not applicable to living specimen, because of cytotoxicity and bleaching of the dye prevents long-term imaging of living cells [8, 9]. Since vital staining based on non-toxic dyes does not even correlate with fat stores as shown for the model organism *C. elegans* [10], fluorescence techniques for live cell experiments prove even worse. To overcome this limitation, label-free imaging techniques based on Raman scattering have been employed to visualize lipid droplets in living cells [11–13]. The Raman effect is an inelastic scattering process exciting molecular vibrations. Since the total number of vibrations depends on the number of atoms and the frequencies on bond strength and mass, the complete Raman spectrum is highly specific for a wide range of chemical structures. Therefore, Raman spectroscopy is a very powerful method to determine subtle compositional changes in biological samples [2]. Since lipids exhibit a large Raman scattering cross-section, the method is specifically suited for visualizing the distribution and composition of lipids. The saturation of lipids can be determined by the strength of the C=C bond vibration, while triglycer-

ide content is accessed by the carboxyl group vibrations. Several studies have therefore focused on lipid uptake and chemical composition of lipid droplets [11, 14–17].

However, spontaneous Raman scattering is a weak process such that fast imaging is not possible. Coherent Raman scattering (CRS), e.g. coherent anti-Stokes Raman scattering (CARS) and stimulated Raman scattering (SRS) overcome this limitation enabling video-rate image acquisition well suited for imaging live cells in real time [18, 19]. In CRS the sample is simultaneously illuminated by two synchronized pulsed lasers called pump and Stokes. When the wavelength difference of the two lasers matches a Raman active vibration, the pump beam will drop in intensity and the Stokes beam will be enhanced (SRS) and light at the anti-Stokes frequency is generated (CARS). By amplitude-modulating the Stokes beam, the decrease of the pump beam can be recorded as intensity oscillation of the pump pulses at the modulation frequency, which is called stimulated Raman loss (SRL). The SRS signal is linearly dependent on the amount of excited bonds and therefore linear to the concentration of the targeted molecule. This is a substantial advantage over CARS, which also suffers from a non-resonant background that is independent of the laser frequency and needs to be corrected before data analysis. SRS does not exhibit a non-resonant background, since no energy will be transferred, if the energy difference between the beams does not match the vibrational excitation. However, the detection of the small modulation of the laser intensity is also difficult requiring ultra-stable laser sources or balanced detection schemes [20, 21]. CRS offers highest image acquisition speeds at the CH stretching vibrations due to the large Raman scattering cross-section of these vibrations. In particular lipid droplets are characterized by an extraordinarily strong CRS signal at the aliphatic CH stretching vibration, which results from (i) the high abundance of methylene groups in fatty acids and (ii) high triglyceride concentration in lipid droplets. Hence, CRS has been employed to visualize the distribution of lipids and lipid droplets in organisms and cells [22–28]. In regards to atherosclerotic progression on a cellular level, in particular the lipid accumulation and metabolism in monocytes and macrophages have been studied [29–32]. Biomedical applications with the focus on CRS-based lipid imaging have been extensively reviewed [8, 19, 33].

While CRS provides the possibility of measuring mm-sized sample areas within a few seconds, e.g. for tissue characterization, the chemical information of fast CRS imaging is limited, because in contrast to spontaneous Raman imaging CRS is based on the acquisition of images at a single vibrational frequency only. However, there are two approaches to

acquire spectral data using CRS. Hyperspectral CRS is based on fast tuning of the wavelength of pump or Stokes laser and sequential recording of a spectral region within microseconds [34–37]. In multiplex CARS on the other hand the sample is illuminated with a broad band pulse covering the spectral range of interest using few cycle lasers of ultrashort pulse duration, e.g. 16 fs [38]. The applications and instrumentations of spontaneous and coherent Raman spectroscopy have been recently reviewed [39].

Although a key strength of CRS and Raman imaging is its ability to visualize the distribution of marker molecules label-free, image contrast as well as molecular sensitivity and specificity can be further enhanced using vibrational labeling techniques, e.g. through the integration of alkyne bonds [40–43] or isotope labels [44–47]. Deuteration of the target molecule by replacing hydrogen by the heavier deuterium, leads to different excitation energies for the corresponding bonds. The spectral bands of CD vibrations will then appear in the so-called silent wavenumber region of the spectrum of biological samples between 2000 cm^{-1} and 2400 cm^{-1} . This provides the possibility to trace lipids, drugs or other molecules of interest inside cells. Deuterated, exogenously provided lipids can be easily distinguished from endogenous lipids inside the cell [34, 48–50]. By synthesizing highly deuterated cholesterol, the storage and esterification in lipid droplets was investigated using hyperspectral SRS imaging [51] nicely demonstrating that Raman spectroscopy combined with stable isotopic labeling is a powerful counterpart to labeled fluorescence microscopy. A review about SRS microscopy in combination with different labeling techniques was published recently [9].

To fully understand the formation and dynamics behind lipid droplet formation and the metabolism of lipids inside macrophages, live cell investigations are required. It is still unknown where lipid droplets are generated, although there are strong arguments for the development at the endoplasmic reticulum (ER) [52]. Of further interest are the mobility and interaction of lipid droplets with other cellular components as well as the proposed fusion of lipid droplets. To really understand transport processes and metabolic changes, single cells have to be observed over time instead of analyzing different cells as representatives for different time points as is the case for fixed cell experiments. Fast imaging at video-rate is required due to cell growth and mobility of the cells as well as of their intracellular components such as lipid droplets. Finally, laser exposure of cells should be as short as possible. In this study, we present fast spontaneous Raman and SRS imaging of living macrophages during the incubation with deuterated palmitic acid (d_{31} -palmitic acid). We thereby track individual cells over several hours to investigate uptake dynamics and storage efficiency at the

single cell level and for entire cell populations. By employing both techniques, we were able to show that d_{31} -palmitic acid is stored homogeneously inside lipid droplets of one cell but the concentration and uptake dynamics differ significantly between individual cells.

2. Experimental

2.1 Cell culture

All chemicals were purchased from Sigma-Aldrich (St. Louis, MO) if not specified otherwise. THP-1 monocytes (DSMZ, Braunschweig, Germany) were cultured and differentiated into macrophages as previously described [48]. RPMI 1640 medium supplemented with 10% (v/v) fetal bovine serum superior (Biochrom, Berlin, Germany), 1% (v/v) penicillin/streptomycin/L-glutamin, 100 ng/mL phorbol-12-myristate-13-acetate and 50 μM β -mercaptoethanol was used to differentiate monocytes into macrophages for 96 h at 37 °C in an atmosphere of 5% (v/v) CO_2 . Macrophages were grown on calcium fluoride slides (Crystal, Berlin, Germany). For live cell imaging, the object slide was transferred to a heated Stable Z System (Chromaphor Analysen-Technik GmbH, Oberhausen, Germany) containing supplemented RPMI 1640 medium without fetal bovine serum. RPMI medium without phenol red was chosen to avoid possible fluorescent background produced by the dye. No spectral contributions of the medium were found in Raman spectra. D_{31} -palmitic acid was complexed to fatty acid-free bovine serum albumin at a molar ratio of 4 : 1 in Krebs-Ringer bicarbonate buffer and added to the medium to a final concentration of 400 μM .

2.2 Raman imaging

Spontaneous Raman measurements were performed on a confocal Raman microscope alpha300 R (WITec, Ulm, Germany) equipped with a cw diode laser (Toptica Photonics, Gräfelingen, Germany) providing an excitation wavelength of 785 nm. The heated setup was placed on the scan stage and tuned to a temperature of 37 °C inside the medium. A Nikon water immersion objective ($\times 60$ magnification, NA = 1.00) was used and the provided laser power was approximately 60 mW. Raman images of the same cell were obtained over several hours at an interval of 15 min starting from the time point of adding d_{31} -palmitic acid to the medium. The laser focus was adjusted to the middle of the cell. A grating of

300 grooves/mm, an integration time of 85 ms and a step size of $0.5 \mu\text{m}$ was chosen. Data analysis was performed in R [53] using the packages hyperSpec, unmixR and cbmodels [54–56]. All spectra were cleared from cosmic spikes [57]. Baseline correction was performed with the extended multiplicative scatter correction (EMSC) method using six components for fitting [58, 59]. Three assigned baseline contributions, containing an offset, a linear function and an uncorrected water spectrum, were subtracted. As cell components a cellular protein spectrum and two cellular lipid spectra with and without deuterium signal were used. The N-FINDR spectral unmixing algorithm with output of three endmember spectra was implemented to distinguish different cellular components [60, 61]. A spectral region from 500 cm^{-1} to 3100 cm^{-1} was thereby analyzed. Abundance maps were plotted based on the endmember spectra corresponding to lipids. To evaluate the uptake of d_{31} -palmitic acid, the spectra were area normalized and the intensity value of the lipid endmember spectrum at 2101 cm^{-1} , corresponding to the highest CD stretching vibration, of each Raman image was plotted over time.

2.3 SRS imaging

Coherent Raman imaging experiments were performed using a compact fiber laser pumped OPO (picoEmerald S, APE, Berlin, Germany). The OPO is pumped by the frequency doubled fundamental of an Yb-fiber laser emitting at a pulse repetition rate of 80 MHz a train of pulses of 2 ps duration at 1032 nm. The Yb-fiber laser also serves as the Stokes beam. The OPO provides wavelength tunable signals and idler outputs of more than 500 mW or 400 mW output power, respectively. The signal is used as pump beam. The signal wavelength is tunable from 700 nm to 960 nm providing in combination with the Yb-fundamental a tuning range from 720 cm^{-1} to 4500 cm^{-1} for coherent Raman scattering. Pulse overlap and wavelength tuning are completely computer controlled providing spectral tuning as fast as 5 s per wavelength step. Furthermore, also the temporal walk-off between pump and Stokes beam within the microscope optics can be precompensated by the laser across the whole tuning range. For stimulated Raman scattering imaging the laser is equipped with an electrooptic modulator modulating the Yb-laser at 20 MHz. A combined large area Si-photodiode (10 mm^2) and fast analog lock-in amplifier is used for detecting SRS signals (APE, Berlin, Germany). The lock-in amplifier operates in the frequency range from 8 MHz to 20 MHz. The amplification can be chosen from -4.5 dB to 43.5 dB with an additional 12 dB post amplification

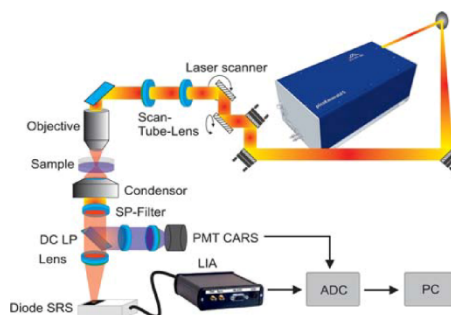


Figure 1 Scheme of the setup used for CRS imaging. For excitation a fully automated ps-OPO-laser (picoEmerald S, APE, Germany) has been coupled to a custom build laser scanning microscope to investigate the lipid uptake of cells. The CARS and SRS signals were detected in forward direction using a condenser. The modulated Stokes beam was blocked by a short pass filter. SRS and CARS signals were separated using a dichroic beam splitter. The SRS signal was detected by a photodiode and fast lock-in amplifier and the CARS signal by a photomultiplier tube (PMT). Afterwards the signals were digitized by an analog to digital converter and the data was sent to the computer for data acquisition.

stage offering video rate signal acquisition by time constants as small as 100 ns.

For coherent Raman imaging, the CRS laser has been coupled into a home-built laser scanning microscope, which has been described in detail previously [62]. A scheme of the setup is shown in Figure 1. For live cell imaging a high-NA $25\times$ water immersion objective with long working distance of 2 mm has been used (CFI 75 Apochromat $25\times$ W MP, NA = 1.1, Nikon, Japan). For imaging the CD stretch vibration, the pump laser has been tuned to 846.8 nm, while the Stokes laser was fixed at 1032.4 nm corresponding to 2125 cm^{-1} . During the measurements, the living cells have been placed in a heated setup as described above. CARS and SRS signals were detected in forward direction using a longpass dichroic beam splitter at 735 nm (Semrock, USA). For detecting the CARS signals, a 770 nm short pass filter and a bandpass filter at 720 nm (both filters from Semrock, USA) have been used in front of the detector. For the detection of the SRS signal, two short pass filters were used in front of the photodiode (short pass 1000 nm Thorlabs, USA, short pass 1010 nm, Semrock, USA). The total power at the sample was 33 mW in the course of the measurement in order to prevent phototoxic effects.

The incubation was started before SRS imaging to achieve better contrast since the signals of the CD vibrations were weak in the early incubation process.

An image of the same area with a spatial resolution of $1.3\ \mu\text{m}$ and an axial resolution of $7.5\ \mu\text{m}$ was taken every 30 min providing an overview of several cells ranging from 17 h to 37 h of incubation. For investigating the uptake of d_{31} -palmitic acid into macrophages, SRS pixel values were summed over the area of each cell and time point. Graphs were plotted in OriginPro 8 (OriginLab, Northampton, MA).

3. Results

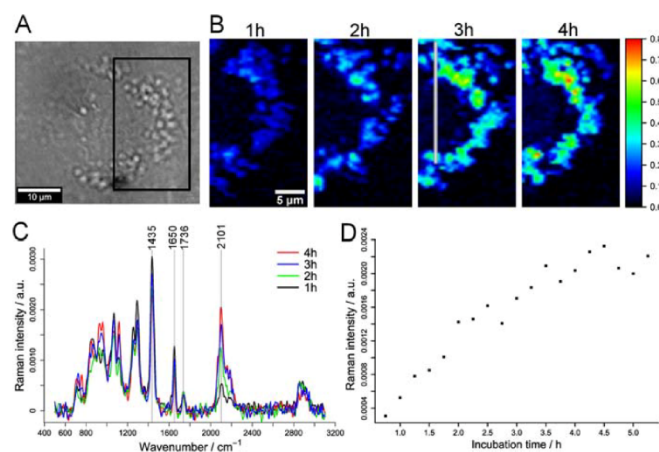
3.1 Raman imaging

Fast spontaneous Raman imaging was employed to image living THP-1 macrophages during the incubation process with d_{31} -palmitic acid. Several aspects require fast imaging as for instance possible photo-damage caused by the excitation laser as well as changes in cellular morphology. Lipid droplets are dynamic organelles and undergo diffuse or even active motion [27]. A compromise between spectral and image quality is needed since long integration times per image point may lead to image artifacts if the acquisition times are longer than cellular processes. With a short integration time of only 85 ms, it was possible to image representative regions of a cell within 4 min.

Figure 2 displays the results obtained by Raman imaging of a living macrophage. The area indicated with a black rectangle as seen in the bright field image in Figure 2A is the chosen measurement area. Lipid droplets can be noticed around the ER close to the nucleus. As discussed above, the area was chosen, because lipid droplets most likely form with-

in the ER and later bud off from the ER membrane leaflets. Figure 2B shows the lipid endmember abundance maps after the N-FINDR analysis. The N-FINDR algorithm searches for the highest spectral differences in the dataset. The output spectra are referred to as endmembers and represent the spectral information associated with the cellular components. By applying the algorithm, mainly three endmembers are obtained corresponding to lipids, proteins and the surrounding aqueous background of the cell. In Figure 2B the lipid droplets are visualized by plotting the representative endmember. Over the time frame of 4 hours, changes within the ring-shaped arrangement in the perinuclear region were observed due to a diffuse mobility of the droplets in the cytoplasm. The pixel intensity of the abundance maps increases reflecting the increase of the intensities of Raman lipid spectra. An overall increase of lipid droplets can be noticed especially in the upper right side corner of the image frame. Figure 2C displays the lipid endmember spectra which correspond to the abundance maps in Figure 2B. In the fingerprint region between $600\ \text{cm}^{-1}$ and $1800\ \text{cm}^{-1}$ a typical lipid band structure can be seen. The C=O band of ester groups at $1736\ \text{cm}^{-1}$ provides evidence for high amount of triglycerides. The band at $1650\ \text{cm}^{-1}$ can be assigned to C=C stretching vibrations, which cannot originate from the saturated d_{31} -palmitic acid. This indicates the presences of non-deuterated, unsaturated lipids in the droplets. The signal between $2000\ \text{cm}^{-1}$ and $2300\ \text{cm}^{-1}$ originates from CD vibrations of d_{31} -palmitic acid, proving that the cell stored d_{31} -palmitic acid within the lipid droplets. D_{31} -palmitic acid is fully deuterated and hence exhibits a very prominent band at $2101\ \text{cm}^{-1}$ which is associated with the symmetric CD_2 stretching vibrations. A

Figure 2 (A) Bright field image of a sampled human macrophage with black rectangle marking the measured area. (B) Raman abundance maps of the lipid endmember spectrum for time points indicated on top. Spectra in the vertical, white line at 3 h were taken out due to detector features which did not originate from the cell. (C) Normalized lipid spectra corresponding to abundance maps in (B). A time-dependent increase of the CD vibration band between $2000\ \text{cm}^{-1}$ and $2300\ \text{cm}^{-1}$ is visible. (D) Normalized Raman intensity values at $2101\ \text{cm}^{-1}$ plotted over the incubation time show an increase of the CD vibration band.



smaller maximum at 2196 cm^{-1} can be attributed to less abundant symmetric CD_3 stretching vibrations. The bands corresponding to CD vibrations are clearly increasing over time, demonstrating that the cell was viable and continued to take up d_{31} -palmitic acid during the measurement. This is also shown in Figure 2D, where the normalized Raman intensity value of the lipid endmember spectra at 2101 cm^{-1} is plotted over time for the entire measurement series. The intensity is increasing continuously but seems to slow down after 3 h. The distribution of d_{31} -palmitic acid inside the image frame is homogeneous. Each droplet stored d_{31} -palmitic acid in a similar concentration. As also seen in previous studies, d_{31} -palmitic acid is exclusively stored in and esterified during the incorporation into lipid droplets [49].

3.2 SRS imaging

SRS imaging provides the possibility to rapidly image a set of multiple cells during the incubation process. The Raman intensity at 2125 cm^{-1} was chosen to monitor the uptake of d_{31} -palmitic acid. Due to the unique deuterated bond vibration, it is ensured that the signal can only originate from the fatty acid. Figure 3 is comprised of CARS (A), SRS (B) and composite images (C) of a macrophage incubated for 24 h and subsequently fixed with formaldehyde. Local information can be obtained directly from the lipid droplets where d_{31} -palmitic acid is exclusively stored. The lipid droplets are located around the nucleus and are highly abundant. In Figure 3A the non-resonant background of CARS generates a low contrast between lipid droplets and the surrounding medium. High background contributions originate especially from the aqueous environment. Furthermore, interference artifacts falsify the information (marked with red arrows) [63]. Figure 3B shows the corresponding SRS image. Only within the lipid droplets, signal is generated (white) while outside no signal is observed (black). The storage of the incor-

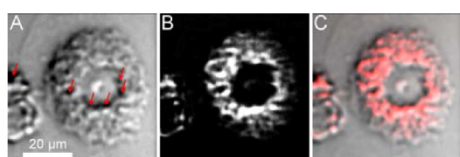


Figure 3 Image of a fixed human macrophage incubated for 24 h with d_{31} -palmitic acid measured at 2125 cm^{-1} . (A) CARS signal with non-resonant background, (B) SRS signal, (C) composite image of SRS (red) and CARS (grey) signal. The contrast of the SRS compared to the CARS image is significantly improved and no interference artifacts are visible (marked with red arrows in (A)).

porated deuterated fatty acids is therefore directly visible without the need of processing of the image. The signal is directly proportional to the concentration of d_{31} -palmitic acid due to the absence of non-resonant background contributions as explained before. Figure 3C shows the composite image of the CARS (grey) and SRS (red) signal. After 24 h the cell has not reached foam cell formation yet.

Figure 4 displays the SRS signal of four individual cells measured during live cell experiments for time points between 17 h and 33 h. In the two cells of row A and B, a clear increase of the SRS signal intensity can be seen as well as changes in the position of the lipid droplets. During the incubation, macrophages change their morphology, which was also observed by Raman imaging. These changes happen on a relatively fast time scale. The cell of row A changes its morphology in less than 30 min from a tilted towards a horizontal axis of the lipid droplet structure. Since SRS is a fast modality, visual artifacts of lipid droplet translocation is not as problematic as in Raman imaging. Small morphological changes are also visible in the two cells of Figure 4C and D, but it is difficult to evaluate the uptake visually. In order to gain more information about the concentration of d_{31} -palmitic acid inside each cell, SRS pixel values were summed over the cell areas for the different time points. The results are presented in Figure 5.

Two different sets of cells were found. Few cells have high concentration of d_{31} -palmitic acid as indi-

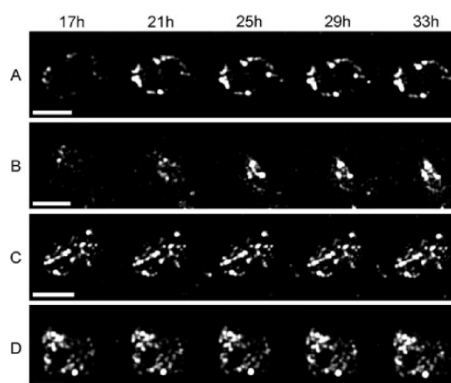


Figure 4 SRS signal originating from four individual cells at different time points ranging from 17 h to 33 h (scale bar: $30\text{ }\mu\text{m}$). The images are taken from a long time series imaging several cells simultaneously using the following image acquisition parameters: image size 2048×2048 pixels, which corresponds to $300\text{ }\mu\text{m} \times 300\text{ }\mu\text{m}$, power at the sample 13 mW pump at 846.8 nm , 20 mW Stokes at 1032.4 nm , Lock-In Amplifier $20\text{ }\mu\text{s}$ filter time constant, pixel dwell time $8\text{ }\mu\text{s}$, averaging of 2 frames, image acquisition 67 s.

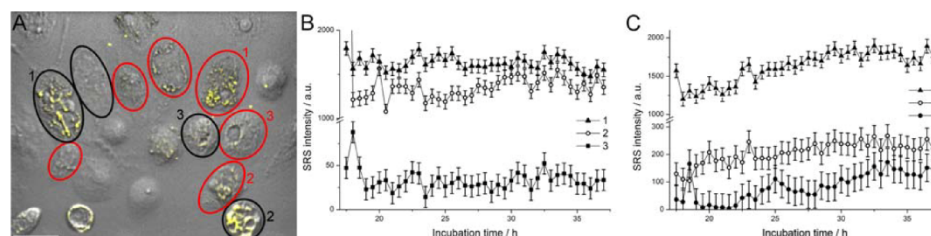


Figure 5 (A) Overview of cells after 17 h incubation overlaid with their SRS signal in yellow (scale bar: 50 μm). Cells circled in black show a stable pixel value, cells marked in red show an increase. (B) Summed SRS intensity for stable cells marked by black circles in (A). (C) Summed SRS intensity for cells with uptake as circled in red in (A).

rectly seen through high SRS intensity pixel values. The majority of the cells show much lower SRS intensity pixel values (ca. $50\times$) having stored less d_{31} -palmitic acid since the beginning of the experiment. Interestingly, most cells with high SRS signal did not show an increase over time. We conclude that these cells have already exhausted their capacity of storing d_{31} -palmitic acid in the first 17 h of incubation. Cells marked with a black circle in Figure 5A show cells which exhibited a stable signal. In Figure 5B the steady signal intensity associated with 2125 cm^{-1} is plotted for three corresponding cells. From previous studies, it is known that d_{31} -palmitic acid is not biochemically degraded or transported out of the cell which would result in a decrease of SRS intensity [49]. No overall decrease has been observed in any cell. For the majority of the cells, pixel values increase and therefore d_{31} -palmitic acid is continuously taken up by cells (marked with red circles in Figure 5A). The uptake is plotted in Figure 5C, again for three cells. The cells apparently take up d_{31} -palmitic acid at different rates. For example, the uptake in cell 3 is noticeably enhanced only after 24 h, while cell 1 shows a much higher concentration. The uptake in a single cell seems to be not constant and can exhibit changes in the uptake rate. Due to the mobility of the macrophages, artifacts of cells moving in and out of the focus cannot be avoided but are easily discerned. It can be seen in the intensity plot for cell 3 of Figure 5C by the sudden increase and decrease of signal at 18 h. During the experiment, only two cells moved completely out of the focus.

4. Discussion and conclusion

Fast spontaneous Raman and SRS imaging enabled the detection of d_{31} -palmitic acid uptake by human THP-1 macrophages under live cell conditions. Due to the employed fast and molecular specific imaging

techniques, cellular processes in real-time for single cells were followed. With an integration time of 85 ms, spontaneous Raman spectra of lipid droplets were obtained and followed within the same cell for more than 5 h. 85 ms is rather fast compared to common integration times for biological samples which are often on the order of seconds. Despite the short integration times, the noise level is well below the signal intensity which therefore allows fast spontaneous Raman imaging. Spectral analysis showed a strong increase of d_{31} -palmitic acid over time and revealed information of other lipids stored in the droplets as for example unsaturated fatty acids. In the course of the first 5 h of incubation, the number of lipid droplets was increasing. The accumulation of the droplets around the ER is in good agreement with the current knowledge of lipid droplet biogenesis.

Most live cell studies do not repeatedly measure the same cells and thus lack the possibility to trace metabolic processes. Furthermore, the progression of cell-to-cell variability cannot be assessed. Imaging of the same cell over time is challenging due to the repeated laser exposure of the same area. To minimize the phototoxicity an excitation wavelength of 785 nm was chosen. Laser power of 60 mW and a short acquisition time of 85 ms did not affect the viability of the measured cells. Tests with wavelengths lower than 785 nm were performed but led to cell death after one hour of incubation at the latest. This was clearly visible by dramatic morphological changes and intensity degradation of the overall Raman spectra of the sample. These observations are supported by a study about the wavelength dependency of radiation-induced damages in living cells [64]. In another study, living lung cells were irradiated for 40 min with 785 nm at a power of 115 mW [65]. No changes in Raman spectra were observed and cell viability tests proved that the cells were alive after irradiation. Same experiments with 488 nm and 514 nm at a power of just 5 mW showed dramatic changes in morphology after just 5 min and

consequently cell death. An excitation wavelength of 785 nm is therefore highly suited for live cell imaging. Even over long periods of time with rather high laser power, cells are unaffected. This is especially important for incubation or proliferation studies of cells. Although higher wavelengths would reduce the phototoxicity even more, the drop in Raman signal intensity due to the ω^4 dependence in addition to low quantum yields of silicon-based CCDs above 1 μm hinders the feasibility. For Raman imaging 785 nm offers the most efficient trade-off between signal intensity and cell viability.

SRS imaging provided information on a whole cell population rather than single cells like in Raman imaging. For SRS imaging either the pump or the Stokes laser needs to be amplitude-modulated and the modulation transfer towards the other laser is detected. In the configuration employed, the Stokes laser at 1030 nm was modulated and the pump beam at ~ 850 nm was detected. Hence, in comparison to Raman and CARS, higher wavelengths are detected, which are less phototoxic and improve the penetration depth for potential applications in tissue. As evident from Figure 3, SRS is more suitable for live cell imaging than CARS, which suffers from the enhanced non-resonant background in aqueous solutions. By investigating deuterated molecules instead of the CH groups, a significantly improved contrast and lower detection limit is realized, since there are practically no Raman resonances in the spectral region around 2100 cm^{-1} , whereas CH groups are virtually present in any organic molecule.

The results obtained by SRS imaging demonstrate for the first time that the uptake kinetics of d_{31} -palmitic acid by macrophages differ between individual cells. While some cells exhausted their storage capacity of d_{31} -palmitic acid within the first 17 h, the majority of the cells showed clear continuing uptake. An explanation for this finding might be that macrophages exhibit varying amounts of lipid droplets after differentiation of monocytes and before incubation with d_{31} -palmitic acid. The pathway of incorporating fatty acids into existing lipid droplets is faster than building of new lipid droplets, hence cells with initially more lipid droplets might exhaust their storage capacity of palmitic acid faster than others leading to the observed heterogeneity in the cell population.

The uptake rate differed between cells and was not constant over time within a cell. In previous studies, heterogeneity in the number and size of lipid droplets was observed [5]. This effect is considered as a mechanism that protects cells from lipotoxicity. While the overall lipid droplet accumulation depends on lipid availability, the distribution of lipids between cells of a population differs. Compared to the average lipid accumulation, only few cells exhibit high-lipid storage within a population [5]. But these

cells play a crucial role for the population by mediating toxic metabolites and even supplying lipids to cells with low lipid content. This difference in lipid accumulation was observed in the presented SRS images as well. The cells could be classified into two sets depending on the amount of stored d_{31} -palmitic acid. Thereby the majority of the cells have stored less of the fatty acid. In general, macrophages have high storage efficiency for d_{31} -palmitic acid. Even for incubation times over 24 h continuing uptake of d_{31} -palmitic acid was detected in most cells. In agreement to the live cell results, Matthäus et al. have previously shown in fixed THP-1 macrophages that the overall uptake of d_{31} -palmitic acid does not saturate when covering a time frame of up to 36 h [49].

By combining results from Raman and SRS imaging, we are able to present a complete overview of the incubation and uptake behaviors of living macrophages ranging from 45 min up to 37 h. Individual cells as well as ensembles of cells were investigated. For the first time, clear cell-to-cell heterogeneity in the uptake kinetics of d_{31} -palmitic acid was observed.

Acknowledgements We gratefully acknowledge financial support of the European Union via the Europäischer Fonds für Regionale Entwicklung (EFRE) and the "Thüringer Ministerium für Wirtschaft, Wissenschaft und Digitale Gesellschaft (TMWWDG)" (project 2015FOR-0001), from the German Ministry for Science and Education (BMBF) for endoCARS (FKZ 13N13805) and for nutriCARD (FKZ 01EA1411A), and by the Carl Zeiss Stiftung.

References

- [1] World Health Organization, Global status report on noncommunicable diseases 2014. Geneva, 2014.
- [2] K. Eberhardt, C. Stiebing, C. Matthäus, M. Schmitt, and J. Popp, *Expert Rev Mol Diagn* **15**, 773–787 (2015).
- [3] K. J. Moore and M. W. Freeman, *Arterioscler Thromb Vasc Biol* **26**, 1702–1711 (2006).
- [4] S. Xu, Y. Huang, Y. Xie, T. Lan, K. Le, J. Chen, S. Chen, S. Gao, X. Xu, X. Shen, H. Huang, and P. Liu, *J Cytol* **62**, 473–481 (2010).
- [5] A. Herms, M. Bosch, N. Ariotti, B. J. N. Reddy, A. Fajardo, A. Fernández-Vidal, A. Alvarez-Guaita, M. A. Fernández-Rojo, C. Rentero, F. Tebar, C. Enrich, M.-I. Geli, R. G. Parton, S. P. Gross, and A. Pol, *Curr Biol* **23**, 1489–1496 (2013).
- [6] X. Xu, A. Zhang, N. Li, P.-L. Li, F. Zhang, *Cell Physiol Biochem* **37**, 419–431 (2015).
- [7] A. S. Haka, V. C. Barbosa-Lorenzi, H. J. Lee, D. J. Falcone, C. A. Hudis, A. J. Dannenberg, and F. R. Maxfield, *J Lipid Res* **57**, 980–992 (2016).
- [8] A. Zumbusch, W. Langbein, and P. Borri, *Prog Lipid Res* **52**, 615–632 (2013).

- [9] W. J. Tipping, M. Lee, A. Serrels, V. G. Brunton, and A. N. Hulme, *Chem Soc Rev* **45**, 2075–2089 (2016).
- [10] K. Yen, T. T. Le, A. Bansal, S. D. Narasimhan, J.-X. Cheng, and H. A. Tissenbaum, *PLoS ONE* **5**, e12810 (2010).
- [11] C. Cao, D. Zhou, T. Chen, A. M. Streets, and Y. Huang, *Anal Chem* **88**, 4931–4939 (2016).
- [12] R. Smith, K. L. Wright, and L. Ashton, *Analyst* **141**, 3590–3600 (2016).
- [13] H. Wolinski, M. Paar, C. Jüngst, N. A. Steiner, D. Kolb, A. Lass, R. Zimmermann, A. Zumbusch, and S. D. Kohlwein, *FASEB J* **26**, 597 (2012).
- [14] Y. Yu, P. V. Ramachandran, and M. C. Wang, *Biochim Biophys Acta* **1841**, 1120–1129 (2014).
- [15] I. W. Schie, L. Nolte, T. L. Pedersen, Z. Smith, J. Wu, I. Yahiatène, J. W. Newman, and T. Huser, *Analyst* **138**, 6662–6670 (2013).
- [16] H. A. Rinia, K. N. J. Burger, M. Bonn, and M. Müller, *Biophys J* **95**, 4908–4914 (2008).
- [17] S. Daemen, M. A. van Zandvoort, S. H. Parekh, and M. K. Hesselink, *Mol Metab* **5**, 153–163 (2015).
- [18] B. G. Saar, C. W. Freudiger, J. Reichman, C. M. Stanley, G. R. Holtom, and X. S. Xie, *Science* **330**, 1368–1370 (2010).
- [19] I. W. Schie, C. Krafft, and J. Popp, *Analyst* **140**, 3897–3909 (2015).
- [20] T. Gottschall, T. Meyer, M. Schmitt, J. Popp, J. Limpert, and A. Tünnermann, *Opt Express* **23**, 23968–23977 (2015).
- [21] K. Nose, Y. Ozeki, T. Kishi, K. Sumimura, N. Nishizawa, K. Fukui, Y. Kanematsu, and K. Itoh, *Opt Express* **20**, 13958–13965 (2012).
- [22] A. Enejder, C. Brackmann, and F. Svedberg, *IEEE J Sel Top Quantum Electron* **16**, 506–515 (2010).
- [23] T. T. Le, H. M. Duren, M. N. Slipchenko, C.-D. Hu, and J.-X. Cheng, *J Lipid Res* **51**, 672–677 (2010).
- [24] C. Di Napoli, F. Masia, I. Pope, C. Otto, W. Langbein, and P. Borri, *J Biophotonics* **7**, 68–76 (2014).
- [25] N. Billecke, G. Rago, M. Bosma, G. Eijkel, A. Gemmink, P. Leproux, G. Huss, P. Schrauwen, M. K. C. Hesselink, M. Bonn, and S. H. Parekh, *Histochem Cell Biol* **141**, 263–273 (2013).
- [26] Y.-H. Yi, C.-H. Chien, W.-W. Chen, T.-H. Ma, K.-Y. Liu, Y.-S. Chang, T.-C. Chang, and S. J. Lo, *J Biomed Opt* **19**, 011011 (2013).
- [27] C. Jüngst, M. J. Winterhalder, and A. Zumbusch, *J Biophotonics* **4**, 435–441 (2011).
- [28] A. Folick, W. Min, and M. C. Wang, *Curr Opin Genet Dev* **21**, 585–590 (2011).
- [29] L. J. den Hartigh, J. E. Connolly-Rohrbach, S. Fore, T. R. Huser, and J. C. Rutledge, *J Immunol* **184**, 3927–3936 (2010).
- [30] R. S. Lim, A. Kratzer, N. P. Barry, S. Miyazaki-Anzai, M. Miyazaki, W. W. Mantulin, M. Levi, E. O. Potma, and B. J. Tromberg, *J Lipid Res* **51**, 1729–1737 (2010).
- [31] C. Matthäus, G. Bergner, C. Krafft, B. Dietzek, S. Lorkowski, and J. Popp, *Proc SPIE* **7715**, 771511–771518 (2010).
- [32] W.-W. Chen, C.-H. Chien, C.-L. Wang, H.-H. Wang, Y.-L. Wang, S.-T. Ding, T.-S. Lee, and T.-C. Chang, *Anal Bioanal Chem* **405**, 8549–8559 (2013).
- [33] T. T. Le, S. Yue, and J.-X. Cheng, *J Lipid Res* **51**, 3091–3102 (2010).
- [34] D. Fu, Y. Yu, A. Folick, E. Currie, R. Farese, T.-H. Tsai, X. S. Xie, and M. C. Wang, *J Am Chem Soc* **136**, 8820–8828 (2014).
- [35] Y. Ozeki, W. Umemura, Y. Otsuka, S. Satoh, H. Hashimoto, K. Sumimura, N. Nishizawa, K. Fukui, and K. Itoh, *Nat Photonics* **6**, 845–851 (2012).
- [36] D. Zhang, M. N. Slipchenko, D. E. Leaird, A. M. Weiner, and J.-X. Cheng, *Opt Express* **21**, 13864 (2013).
- [37] C.-S. Liao, M. N. Slipchenko, P. Wang, J. Li, S.-Y. Lee, R. A. Oglesbee, and J.-X. Cheng, *Light Sci Appl* **4**, e265 (2015).
- [38] C. H. Camp Jr, Y. J. Lee, J. M. Heddleston, C. M. Hartshorn, A. R. Hight Walker, J. N. Rich, J. D. Lathia, and M. T. Cicerone, *Nat Photonics* **8**, 627–634 (2014).
- [39] C. Krafft, I. W. Schie, T. Meyer, M. Schmitt, and J. Popp, *Chem Soc Rev* **45**, 1819–1849 (2016).
- [40] T. Weeks, S. Wachsmann-Hogiu, and T. Huser, *Opt Express* **17**, 17044–17051 (2009).
- [41] Z. Chen, D. W. Paley, L. Wei, A. L. Weisman, R. A. Friesner, C. Nuckolls, and W. Min, *J Am Chem Soc* **136**, 8027–8033 (2014).
- [42] S. Hong, T. Chen, Y. Zhu, A. Li, Y. Huang, and X. Chen, *Angew Chem Int Ed* **53**, 5827–5831 (2014).
- [43] L. Wei, F. Hu, Y. Shen, Z. Chen, Y. Yu, C.-C. Lin, M. C. Wang, and W. Min, *Nat Meth* **11**, 410–412 (2014).
- [44] G. Bergner, C. R. Albert, M. Schiller, G. Bringmann, T. Schirmeister, B. Dietzek, S. Niebling, S. Schlücker, and J. Popp, *Analyst* **136**, 3686–3693 (2011).
- [45] Y. Shen, F. Xu, L. Wei, F. Hu, and W. Min, *Angew Chem Int Ed* **53**, 5596–5599 (2014).
- [46] L. Wei, Y. Shen, F. Xu, F. Hu, J. K. Harrington, K. L. Targoff, and W. Min, *ACS Chem Biol* **10**, 901–908 (2015).
- [47] J. Li and J.-X. Cheng, *Sci Rep* **4**, 6807 (2014).
- [48] C. Stiebing, C. Matthäus, C. Krafft, A.-A. Keller, K. Weber, S. Lorkowski, and J. Popp, *Anal Bioanal Chem* **406**, 7037–7046 (2014).
- [49] C. Matthäus, C. Krafft, B. Dietzek, B. R. Brehm, S. Lorkowski, and J. Popp, *Anal Chem* **84**, 8549–8556 (2012).
- [50] M. N. Slipchenko, T. T. Le, H. Chen, and J.-X. Cheng, *J Phys Chem B* **113**, 7681–7686 (2009).
- [51] A. Alfonso-Garcia, S. G. Pfisterer, H. Riezman, E. Ikonen, and E. O. Potma, *J Biomed Opt* **21**, 061003 (2015).
- [52] F. Wilfling, J. T. Haas, T. C. Walther, and R. V. Farese, *Curr Opin Chem Biol* **29**, 39–45 (2014).
- [53] R Core Team, R: A Language and Environment for Statistical Computing, 2015.
- [54] C. Beleites and V. Sergo, hyperSpec: a package to handle hyperspectral data sets in R, 2015.
- [55] C. McManus, unmixR: Spectral Unmixing Methods, 2013.
- [56] C. Beleites, cbmodels: Collection of “combined” models: PCA-LDA, PLS-LDA, PLS-LR as well as EMSC, 2015.
- [57] O. Ryabchykov, T. Bocklitz, A. Ramoji, U. Neugebauer, M. Foerster, C. Kroegel, M. Bauer, M. Kiehn-

- topf, and J. Popp, *Chemometr Intell Lab* **155**, 1–6 (2016).
- [58] H. Martens, J. P. Nielsen, and S. B. Engelsen, *Anal Chem* **75**, 394–404 (2003).
- [59] N. K. Afseth, and A. Kohler, *Chemometr Intell Lab* **117**, 92–99 (2012).
- [60] M. Hedegaard, C. Matthäus, S. Hassing, C. Krafft, M. Diem, and J. Popp, *Theor Chem Acc* **130**, 1249–1260 (2011).
- [61] M. E. Winter, *Proc SPIE* **3753**, 266–275 (1999).
- [62] T. Meyer, M. Baumgartl, T. Gottschall, T. Pascher, A. Wuttig, C. Matthaues, B. F. M. Romeike, B. R. Brehm, J. Limpert, A. Tuennermann, O. Guntinas-Lichius, B. Dietzek, M. Schmitt, and J. Popp, *Analyst* **138**, 4048–4057 (2013).
- [63] J.-X. Cheng, Y. K. Jia, G. Zheng, and X. S. Xie, *Biophys J* **83**, 502–509 (2002).
- [64] G. J. Puppels, J. H. F. Olminkhof, G. M. J. Segers-Nolten, C. Otto, F. F. M. de Mul, and J. Greve, *Exp Cell Res* **195**, 361–367 (1991).
- [65] I. Notingher, S. Verrier, H. Romanska, A. Bishop, J. Polak, and L. Hench, *Spectroscopy* **16**, 43–51 (2002).

6.3 Raman spectroscopic imaging of human macrophages incubated with triglyceride-enriched oxLDL visualizes translocation of lipids between endocytic vesicles and lipid droplets [CS3]

Clara Stiebing, Lisa Schmölz, Maria Wallert, Christian Matthäus, Stefan Lorkowski⁺, Jürgen Popp⁺ (2017)

J Lipid Res. 58(5): 876–883.

⁺gleichwertige Autorenschaft

Der Nachdruck der folgenden Publikation erscheint mit freundlicher Genehmigung von der American Society for Biochemistry and Molecular Biology.

Erklärung zu den Eigenanteilen der Promovendin sowie der weiteren Doktoranden/ Doktorandinnen als Koautoren an den Publikationen und Zweitpublikationsrechten bei einer kumulativen Dissertation.

| Doktoranden | Clara Stiebing | Lisa Schmölz |
|--|----------------|--------------|
| Konzeption des Forschungsansatzes | x | |
| Planung der Untersuchungen | x | x |
| Datenerhebung | x | x |
| Datenanalyse und –interpretation | x | |
| Schreiben des Manuskripts | x | |
| Vorschlag Anrechnung Publikationsäquivalente | 1,0 | |



Raman imaging of macrophages incubated with triglyceride-enriched oxLDL visualizes translocation of lipids between endocytic vesicles and lipid droplets

Clara Stiebing,^{*,†} Lisa Schmölz,^{§,**} Maria Wallert,^{§,††} Christian Matthäus,^{*,†}
Stefan Lorkowski,^{1,§,**} and Jürgen Popp^{1,2,*,†}

Leibniz Institute of Photonic Technology (IPHT),* 07745 Jena, Germany; Institute of Physical Chemistry and Abbe Center of Photonics,[†] Institute of Nutrition and Abbe Center of Photonics,[§] and Competence Cluster of Nutrition and Cardiovascular Health (nutriCARD), Halle-Jena-Leipzig,** Friedrich Schiller University Jena, 07743 Jena, Germany; and Baker IDI Heart and Diabetes Institute,^{††} Melbourne, Australia

Abstract Raman spectroscopic imaging was used to investigate the uptake of oxidized LDLs (oxLDLs) by human macrophages. To better understand the endocytic pathway and the intracellular fate of modified lipoproteins is of foremost interest with regard to the development of atherosclerotic plaques. To obtain information on the storage process of lipids caused by oxLDL uptake, Raman spectroscopic imaging was used because of its unique chemical specificity, especially for lipids. For the present study, a protocol was established to incorporate deuterated tripalmitate into oxLDL. Subsequently, human THP-1 macrophages were incubated for different time points and their chemical composition was analyzed using Raman spectroscopic imaging. β -Carotene was found to be a reliable marker molecule for the uptake of lipoproteins into macrophages. In addition, lipoprotein administration led to small endocytic vesicles with different concentrations of deuterated lipids within the cells. For the first time, the translocation of deuterated lipids from endocytic vesicles into lipid droplets over time is reported in mature human THP-1 macrophages.—Stiebing, C., L. Schmölz, M. Wallert, C. Matthäus, S. Lorkowski, and J. Popp. Raman imaging of macrophages incubated with triglyceride-enriched oxLDL visualizes translocation of lipids between endocytic vesicles and lipid droplets. *J. Lipid Res.* 2017. 58: 876–883.

Supplementary key words Raman spectroscopy • β -carotene • tripalmitate • endocytosis • atherosclerosis • oxidized low density lipoprotein

Understanding the mechanisms behind lipoprotein metabolism is important for the assessment of cardiovascular disease risk and the development of new therapeutic ap-

proaches. Lipids are transported by lipoproteins, especially LDLs, and can enter the arterial walls at sites of endothelial dysfunction. Intraluminal accumulation and oxidation of LDL, namely oxidized LDL (oxLDL), is usually accompanied by an immigration of blood monocytes, which differentiate into macrophages. The uncontrolled uptake of oxLDL by macrophages results in the formation of foam cells (1). Because modified LDLs are a key factor that triggers atherosclerosis, the interaction between modified LDLs and macrophages is of particular interest. The uptake and subsequent processing of incorporated lipids into macrophages therefore gain high attention in lipid research.

State of the art lipid analysis is mostly performed by various mass spectrometric and chromatographic methods (2, 3). Combinations of these techniques are very powerful in separating and identifying lipids from cells and tissues, thus providing valuable information about the biochemistry of lipid metabolism. The methodologies are based on bulk measurements and, with the exception of MS-based imaging techniques, do not provide spatial information. Optical approaches are needed to investigate cellular structures (4). To obtain information on the single cell level, flow cytometry and fluorescence microscopy are often used. By staining lipids of interest with specific labels, as for instance Nile red, their intracellular distribution can be monitored (5–7). However, no information about individual types of lipids or the composition of lipids within intracellular compartments or membranes can be retrieved because staining protocols used for lipids are not antibody-based and, therefore, not specific to different types of lipids (8). Furthermore, it is unclear how the often bulky

This work was supported by the Carl Zeiss Stiftung and the German Federal Ministry for Education and Research (nutriCARD, FKZ 01EA1411A).

Manuscript received 21 September 2016 and in revised form 15 January 2017.

Published, JLR Papers in Press, January 31, 2017

DOI <https://doi.org/10.1194/jlr.M071688>

¹S. Lorkowski and J. Popp contributed equally to this work.

²To whom correspondence should be addressed.
e-mail: juergen.popp@leibniz-ipht.de



labels influence the chemical integrity of the lipids of interest and the associated cellular processes. A very attractive alternative to study intracellular lipids spatially resolved at the single cell level is provided by combining vibrational spectroscopy techniques with microscopy.

Raman spectroscopy has great potential in single cell analysis due to its high chemical specificity originating from exciting chemical bond vibrations, which are unique for particular molecular structures and functionalities. Lipids, especially, have a high Raman scattering cross-section and therefore give rise to high scattering intensities. Different types of lipids can be easily distinguished, such as unsaturated and saturated fatty acids, due to the presence of C=C double bond vibrations, which feature spectral bands different from C-C bond vibrations. Although Raman spectroscopy has high specificity, stable isotopic labeling with deuterium can improve the spectral specificity as well as sensitivity. The exchange of hydrogen by deuterium does not alter the chemical properties of a molecule. However, the associated chemical vibrations change in energy and, therefore, their spectral appearances. The resulting CD bond vibrations are at significantly lower wavenumbers and appear in the so-called silent wavenumber region of Raman spectra of biological samples. By adding deuterated fatty acids to cell culture medium, their uptake can be easily traced and the deuterated fatty acids can be distinguished from the naturally occurring lipids inside the cell (9–11). Excitation wavelengths in the visible to near-infrared range provide the possibility to image cells with a resolution of around 0.5 μm . Raman imaging is therefore a highly suitable technique for the investigation of biological samples, especially cells (12–14).

Lipoproteins are the main carrier of lipids inside the blood stream. They consist of a phospholipid monolayer with embedded proteins and a lipid core containing cholesterol esters, triglycerides, and lipophilic vitamins, such as β -carotene. LDLs arise in the blood from VLDLs via IDLs by the action of lipases and are transported through the blood stream. Eventually, LDLs enter tissue sides and are taken up by cells through endocytosis to provide cholesterol. In the arterial wall, LDL can be modified by oxidation or enzymatic means prior to its uptake. The modification of LDLs is an important step in the early stages of atherosclerotic plaque development because their pathway into macrophages gets altered. While native LDL is taken up by the LDL receptor, uptake of modified LDL is mediated by scavenger receptors like CD36 and LOX-1 (15). In contrast to the LDL receptor pathway, the scavenger receptor pathway is not subjected to negative feedback regulation so that lipid uptake and efflux are not equally controlled. Modified LDL, especially aggregated LDL, can also be taken up via receptor-independent endocytic pathways (16). LPL, which is secreted by macrophages, can bind to LDL and proteoglycans on the cell membrane, which triggers the endocytic uptake of LDL particles as well (17, 18). In the case of high concentrations of modified LDL, macrophages transform into foam cells because the macrophages are overwhelmed with their lipid storage and the whole cytoplasm is filled with cytosolic lipid droplets. By reaching toxic lipid levels, foam cells undergo cell death and leave their lipid-rich

content inside the arterial wall, which contributes to the development of atherosclerotic plaque (19).

Optical techniques are often focused on investigating the composition and vulnerability of plaques (20–22). But for the characterization of early plaque development, the cellular level of lipid metabolism is also of foremost interest. The standard cell culture protocol for the uptake of fatty acids into cells often uses the complexation of free fatty acids to serum albumin. However, another relevant pathway is based on lipoprotein uptake. Until now, only a few publications have dealt with the visualization of cellular processes after the exposure to lipoproteins. A study of the uptake of labeled oxLDL under the influence of different chemical agents by mouse macrophages with fluorescence imaging has been reported (23). An automated high-throughput chemical screening was developed to study the efficiency of agents to block oxLDL-induced foam cell formation. Furthermore, living macrophages incubated with acetylated LDL were imaged using coherent anti-Stokes Raman spectroscopy to measure their lipid content (24). Different image analysis methods were implemented for automated evaluation of the intracellular lipid droplet accumulation. Lipolysis products of VLDLs were also used to incubate THP-1 monocytes (8). Raman spectroscopy revealed that free fatty acids from lipolysis products mediated lipid droplet formation, where more saturated fatty acids were present in cells treated with postprandial VLDL isolated from human blood. VLDL lipolysis products were also used to investigate the motility and composition of lipid droplets in living hepatocytes (25). However, due to the lipolysis, the actual pathway of lipoproteins into cells was not followed.

We present here, for the first time, imaging of the endocytic uptake of oxLDL and the distribution of LDL-associated fatty acids by human macrophages using Raman spectroscopy. In previous studies, uptake and storage of fatty acids by human THP-1 macrophages was investigated using serum albumin-complexed fatty acids (9, 10). To investigate another physiologically relevant pathway, namely endocytosis of lipoproteins, we developed a protocol to incorporate deuterated tripalmitate (d-TP) into isolated LDL. The deuteration allows tracing of the lipids inside the cells due to unique CD bond vibrations. We used oxLDL to mimic the unregulated uptake of lipids into macrophages and found β -carotene as a Raman marker for the uptake of oxLDL into THP-1 macrophages. The storage pattern of d-TP and β -carotene is presented for incubation times up to 72 h. Endocytic vesicles were found that confirm the translocation of the deuterated lipids from the vesicles toward cytosolic lipid droplets over time.

MATERIAL AND METHODS

Preparation and loading of oxLDL

All mentioned chemicals were purchased from Sigma-Aldrich (St. Louis, MO) if not specified otherwise. LDLs were isolated from plasma of healthy humans with normal lipid profile through density gradient ultracentrifugation using NaBr solution. The solution was sent over a PD-10 column (GE Healthcare Europe,



Freiburg, Germany) for desalting using PBS. The protein concentration was determined by Lowry assay following the manufacturer's operating instructions (Bio-Rad Laboratories, Hercules, CA). LDLs (2 mg/ml) were moderately oxidized for 6 h in a 10 μ M CuSO_4 solution at 37°C. Afterwards, the solution was again sent over a PD-10 column to stop oxidation by separating LDL from Cu^{2+} . Subsequently, the concentration was again determined by Lowry assay. Agarose gel electrophoresis was performed to verify the oxidation of LDL particles, as previously described (26). Dynamic light scattering measurements revealed a hydrodynamic radius of approximately 9 nm for the native LDL as well as oxLDL particles. Loading of LDL with radiolabeled lipids was previously described (27, 28). Based on these publications the following protocol was developed to load oxLDL with d-TP. Egg phosphatidylcholine (1 μ mol), 20 nmol butylated hydroxytoluene, and 5 μ mol d-TP were dissolved in chloroform and mixed with an additional 20 μ l of chloroform in a glass tube. After evaporating the chloroform under a N_2 stream, 2 ml of Tris-HCl buffer containing 1 mg/ml EDTA and 0.1 M DTT with pH 7.4 were added. The mixture was flushed with N_2 and sonicated for 6 h in a bath-type sonicator. The hydrodynamic radius of d-TP-loaded liposomes was, on average, 18 nm. oxLDLs (2.5 mg) were mixed with the sonicated lipids and RPMI 1640 medium containing 0.1 mg/ml penicillin/streptomycin/L-glutamine. The final concentration of oxLDL was 300 μ g/ml and the mixture was incubated for about 17 h at 37°C. Compared with oxLDL and liposomes, the hydrodynamic radius of d-TP-loaded oxLDL was clearly separated from both. However, variations in the radius between batches occurred, which might be caused by different endogenous lipid contents of the prepared oxLDL. No effects on incubated cells of different batches were found.

Cell culture

Human THP-1 monocytes (DSMZ, Braunschweig, Germany) were cultured and differentiated into macrophages as previously described (9). Macrophages were grown on calcium fluoride slides (Crystal, Berlin, Germany) and incubated with either 50 μ g/ml unloaded oxLDL for 24 h or d-TP-loaded oxLDL for up to 72 h in RPMI 1640 medium supplemented with 0.1 mg/ml penicillin/streptomycin/L-glutamine. After incubation the cells were washed with PBS and fixed with 4% (w/v) paraformaldehyde for 20 min at room temperature.

Raman measurements and data analysis

A confocal Raman microscope alpha 300 R (WITec, Ulm, Germany) combined with a Nikon water immersion objective (60 \times magnification, NA = 1.00) was used to acquire Raman images. A CW diode laser (Toptica Photonics, Gräfelingen, Germany) provided an excitation wavelength of 785 nm. Raman images of macrophages were taken at a step size of 1 μ m with an integration time of 1 s and a grating of 300 grooves/mm. Single spectra of β -carotene powder were recorded with an integration time of 0.2 s. All data analyses were performed in R (29) using the packages hyperSpec, cbmodels, unmixR, and ggplot2 (30–33). All spectra were cleared from cosmic spikes (34), interpolated, and simultaneously smoothed. Baseline correction was performed with the extended multiplicative scatter correction (EMSC) method (35). Thereby, seven components were fitted to the spectra and assigned baseline contributions were subtracted. An offset, a linear function, and an uncorrected water spectrum were used as baseline contributions, also leading to water subtraction from the spectra. As cell components, a cellular protein spectrum, a spectrum of pure d-TP, and two cellular lipid spectra with and without deuterium signal were implemented. Raman images were further analyzed by the N-FINDR spectral unmixing algorithm to evaluate cellular components (36, 37). A wavenumber region from 500 to 3,100 cm^{-1} was used. False-color images were reconstructed based on the abundances of the output endmember spectra.

RESULTS

To evaluate the composition of the used LDL particles, Raman spectra of native LDL isolated from serum and Cu^{2+} -modified oxLDL were measured (Fig. 1A, B). There is no distinct difference in the appearance of the main bands of the spectra. In first approximation the spectra can be interpreted as a superposition of Raman bands associated with lipids as well as some proteins. The Raman bands at 1,735, 1,660, and 1,442 cm^{-1} are associated with stretching vibrations of carboxyl and carbonyl C=O and C=C bonds, as well as CH_2 scissoring vibrations, respectively. The band

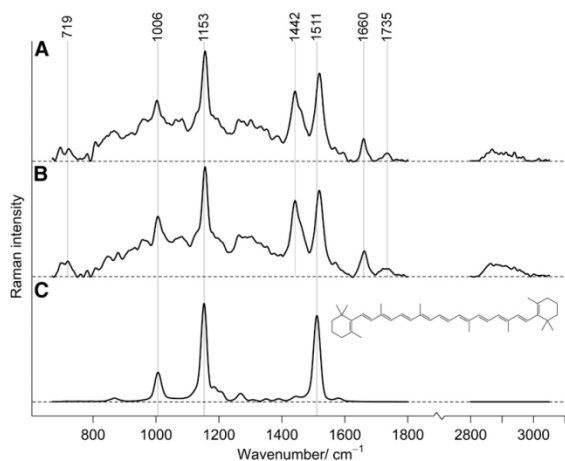


Fig. 1. Spectra of isolated oxLDL (A), LDL (B), and pure β -carotene with its chemical structure (C) are presented. β -Carotene-specific bands can be found in the lipoprotein spectra.

at $1,735\text{ cm}^{-1}$ can be specifically assigned to carboxyl bond vibrations of triglycerides as well as phospholipids. The small band at 719 cm^{-1} can be attributed to the C-N stretch vibrations of the head groups of phosphatidylcholine (38), which is the main constituent of the LDL phospholipid monolayer. Figure 1C shows the Raman spectrum of pure β -carotene, which is a known antioxidant that protects unsaturated fatty acids from oxidation (39). The two main bands are located at $1,511$ and $1,153\text{ cm}^{-1}$ and can be assigned to C=C and C-C stretching vibrations, respectively. The signal observed at $1,006\text{ cm}^{-1}$ originates from a combination of C=CH₃ methyl in-plane rocking and C-H out-of-plane bending vibrations (40). β -Carotene is incorporated into LDL, depending on the diet of the serum donor. Here, the three very prominent bands of β -carotene can be clearly seen in the lipoprotein spectra. They are slightly shifted, most likely due to the different conformations of β -carotene in LDL compared with the crystalline form. Because β -carotene is located inside the LDL particle, it is likely protected from oxidation. The band at $1,511\text{ cm}^{-1}$ corresponding to the double bond vibration would be expected to decrease in case of oxidation.

THP-1 macrophages were incubated with oxLDL for 24 h. Figure 2A depicts Raman spectra of an incubated cell, which represent the highest spectral differences in the dataset. These, so-called, endmember spectra are one outcome of the applied data analysis and depend on the different compositions inside the cell. The spectrum in cyan shows typical protein bands at $1,660$, $1,450$, and $1,003\text{ cm}^{-1}$. In the Raman images in Fig. 2B, the nucleus and nucleolus can be seen in more intense color due to the higher protein concentration resulting in a stronger Raman signal. The lipid distribution within the cell in the form of lipid droplets is shown in red. The band at $1,741\text{ cm}^{-1}$ corresponds to the ester group of lipids, clearly indicating the presence of triglycerides. Band intensities at $1,657\text{ cm}^{-1}$ originate from C=C stretching and at $1,444\text{ cm}^{-1}$ from CH₂ deformation vibrations. A mixture of saturated and unsaturated lipids is therefore present. Also, Raman bands at $1,519$ and $1,155\text{ cm}^{-1}$ can be found, which reveals the storage of β -carotene in lipid droplets. Because cultured THP-1 macrophages normally do not contain β -carotene (data not shown), corresponding Raman bands can be used as a marker for the uptake of oxLDL. No

contributions of β -carotene were found in the protein component. Figure 2B also shows the composite Raman image based on the abundances of lipids and proteins inside the cell. The diameters of the lipid droplets are in the region of $1\text{ }\mu\text{m}$. In agreement with previous studies, most cells did not show clear foam cell transformation (41, 42).

To investigate the storage of lipids that get incorporated into cells following the uptake of lipoproteins, oxLDL was loaded with d-TP and macrophages were afterwards incubated with the loaded oxLDLs for up to 72 h. Figure 3A displays the spectrum of d-TP along with its chemical structure. All hydrogens of the palmitic acid chains are replaced by deuterium, whereas the glycerol backbone is not deuterated. The most prominent bands originate from symmetric CD₂ stretching vibrations at $2,103\text{ cm}^{-1}$ and less pronounced symmetric CD₃ stretching vibrations at $2,193\text{ cm}^{-1}$. The carboxyl ester group vibrations are observed at $1,734\text{ cm}^{-1}$. After incubation for 24 h with d-TP-loaded oxLDL, contributions from deuterium are clearly detected inside the macrophages. Figure 3B presents the four main spectral components for a representative cell. The corresponding single and composite Raman abundance images are shown in Fig. 3C. The spectrum in cyan represents the protein distribution as explained above. The spectrum associated with the lipid droplets is shown in red and features a small band in the CD vibration area, proving the uptake of d-TP and storage of deuterated lipids in lipid droplets. Again, contributions of saturated and unsaturated lipids can be found between 600 and $1,800\text{ cm}^{-1}$. Hence, the exogenously provided deuterated lipids are present next to endogenous lipids. Two additional highly interesting components were found, which did not appear in previous incubation studies with fatty acids complexed to serum albumin (9). The orange spectrum exhibits high contributions derived from d-TP with similar band structure as the reference component. In addition, the presence of β -carotene at $1,519\text{ cm}^{-1}$ is distinctly noticeable, while the band at $1,155\text{ cm}^{-1}$ is most likely overlaid by d-TP bands in the same area. The bands at $1,735$, $1,658$, and $1,442\text{ cm}^{-1}$ highlight further lipid contributions. The vesicle associated with the spectrum depicted in orange is located in only a small area of around $2\text{ }\mu\text{m}$, as seen in Fig. 3C. We assume that this is an endocytic vesicle, which was built upon the uptake of oxLDL containing d-TP. The blue spectrum

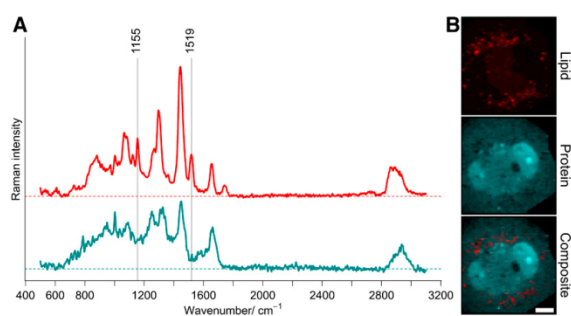


Fig. 2. A: Endmember spectra of a cell incubated with oxLDL for 24 h. Spectra can be assigned to proteins (cyan) and lipids (red). β -Carotene contributions can be seen in the lipid component at $1,519$ and $1,155\text{ cm}^{-1}$. B: Single and composite Raman abundance images corresponding to the spectra shown in (A). Scale bar: $10\text{ }\mu\text{m}$.

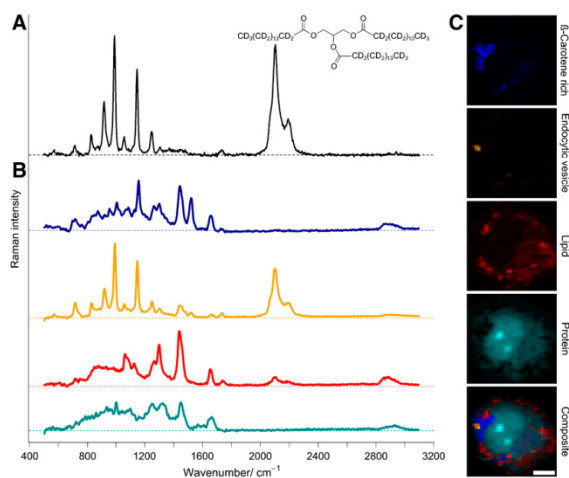


Fig. 3. A: Chemical structure and spectrum of d-TP featuring CD vibration bands between 2,000 and 2,300 cm^{-1} . B: Endmember spectra of a cell incubated with d-TP-loaded oxLDL for 24 h. Spectra can be assigned to protein (cyan), lipid (red), endocytic vesicle (orange), and β -carotene-rich component (blue). C: Single and composite Raman abundance images corresponding to endmember spectra in (B). Scale bar: 8 μm .

represents a high β -carotene-rich component, which is localized within the perinuclear region. The spectrum also shows band features similar to the oxLDL spectrum, with additional lipid bands that might indicate early endosomal formation before the incorporated oxLDL particles are metabolized.

At incubation times of 24 h, not all cells had endocytic vesicles containing incorporated oxLDL with deuterated lipids. This changed for longer incubation times, where almost all cells exhibited these inclusions. The associated spectral information is very interesting, as the d-TP concentration changes during the incubation time. The spectra of vesicles at early time points show high contributions of d-TP, as seen in Fig. 4A, for 24 h. Toward longer incubation times, a clear decrease of CD bond vibrations between 2,000 and 2,300 cm^{-1} is observed (marked area). Also the band shape in the wavenumber region between 600 and 1,800 cm^{-1} changes significantly. While for 24 h the spectrum resembles d-TP (see Fig. 3A), the spectrum for 72 h shows only small contributions if any. In contrast, the β -carotene band at 1,519 cm^{-1} is found to be independent from the incubation time. All spectra feature a band at 719 cm^{-1} , which is the most prominent band at 72 h.

Again, 719 cm^{-1} can be assigned to C-N vibrations of choline head groups. Apparently, the endocytic vesicles get depleted of d-TP over time. Most likely, d-TP is metabolized in the endocytic vesicles and thereby cleaved. Upon release from the endosomal/lysosomal compartment, the concentration of d-TP is decreasing and the deuterated palmitic acid molecules can be stored in lipid droplets, again through esterification. The storage of deuterated lipids is supported by the simultaneous increase of the CD signals in lipid droplets, as seen in Fig. 4B. Here, lipid droplet spectra of the same cells shown in Fig. 4A are plotted. The higher the incubation time, the more deuterated lipids are stored, clearly noticeable by the increased band intensity around 2,100 cm^{-1} and different band shapes in the lower wavenumber region. The deuterated signal observed in the lipid droplet spectra is most likely not originating from d-TP, but from de novo formed triglycerides that incorporated deuterated palmitic acid. The esterification of deuterated lipids into triglycerides can be seen based on the increasing band intensity at 1,735 cm^{-1} . In conclusion, the results demonstrate a translocation of deuterated lipids from endocytic vesicles toward lipid droplets over time.

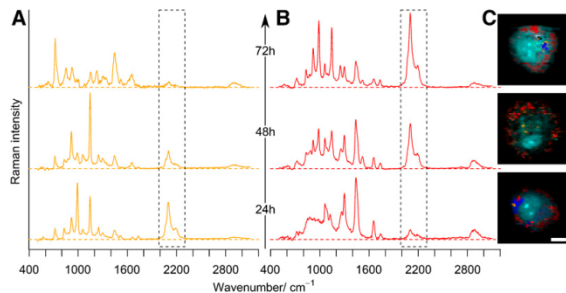


Fig. 4. Raman spectra of endocytic vesicles (A) and lipid droplets (B) of the same cells after incubation with d-TP-loaded oxLDL for 24, 48, and 72 h. C: Composite images of cells associated with the spectra in (A) and (B). Scale bar: 10 μm . A translocation of deuterated lipids from the endocytic vesicle toward lipid droplets over time is clearly visible. While the CD band intensity decreases in the marked region between 2,000 and 2,300 cm^{-1} in endocytic vesicles, it increases in lipid droplets.



In all investigated cells, the deuterated lipid was present alongside β -carotene. The distribution of both components inside lipid droplets of one cell was homogeneous. However, the intracellular concentration of cells of the same time point varied to a great extent. The amount of oxLDLs taken up by the cells appears to differ despite identical exposure times. Furthermore, some cells did not exhibit the β -carotene-rich component. An overview of the heterogeneity between cells is shown in Fig. 5 with the same color-coding as in Fig. 3.

DISCUSSION

The uptake of d-TP-loaded oxLDL and subsequent storage of deuterated fatty acids by human macrophages was demonstrated using Raman spectroscopic imaging. Along with the presence of esterified deuterated palmitic acids, β -carotene was found as a constituent. Cultured THP-1 macrophages normally do not contain β -carotene and the only source in our model was the provided lipoproteins. The β -carotene band at $1,519\text{ cm}^{-1}$ can be easily distinguished from other bands of, for example, proteins or lipids and can be seen as a marker band for the uptake of LDL by macrophages.

The intense Raman bands of β -carotene were used for the investigation of potential drug-delivery applications of polymeric nanoparticles (43). In another study, β -carotene was found colocalized with lipid moieties in plaque depositions of aortic valves (44). The authors assumed that β -carotene derived from LDLs taken up by the macrophages in the arterial wall, a concept that is supported by our results. Utilizing resonance Raman effects, β -carotene in LDL was reported as early as 1984 (45). The authors stated that β -carotene is most likely inside the lipid core of the LDL particles. This is evident from the Raman spectra of LDL presented in our study, because the C=C double bond vibration did not change after

oxidization with Cu^{2+} . Along with the storage of β -carotene in lipid droplets, localized compartments close to the nucleus and endoplasmic reticulum were found. These compartments were found in both cells incubated with d-TP-loaded oxLDL and cells incubated with unloaded oxLDL, which served as controls, but were not present in every cell. The origin and role need to be further investigated, but the compartments might represent early endosomes. The spectral features are similar to the recorded oxLDL spectrum with additional lipid-associated bands. Hence, it is possible that the oxLDL was not metabolized and the deuterated lipids were not released at the time of analysis. Carotenoids are also known biomarkers for mycobacteria in cells. Due to β -carotene bands in the Raman spectra, the mycobacteria could be identified in macrophages (46). To exclude mycobacterial infection, cells used in our study were tested by a mycoplasma detection kit (Jena Bioscience, Germany) and were negative for mycobacteria.

Compared with the commonly used model of serum albumin-complexed fatty acids, longer incubation times are obviously needed to take up lipoproteins and to accumulate the fatty acids inside cytosolic lipid droplets. Albumin-complexed fatty acids can immediately be stored in droplets because they are free fatty acids and are not taken up by a time-consuming endocytic pathway. In our previous studies using the albumin model, deuterated palmitic acid was detected after just 15 min in cytosolic lipid droplets. The CD band intensity increased exponentially, but no clear saturation was reached even after 36 h. Esterification of the fatty acids to triglycerides upon storage in lipid droplets was observed with Raman spectroscopy and enzymatic assays estimating the triglyceride concentration. With the endocytic pathway of lipoproteins, uptake and release of lipids inside the cell is more complex. Intracellular incorporation of deuterated palmitic acid derived from d-TP was detected only after 24 h. Both pathways resulted in a homogeneous storage of fatty acids in lipid droplets as triglycerides. Features correlating to cholesteryl ester formation at, for example, 700 cm^{-1} were not found in the obtained spectra, suggesting that the nascent lipid droplets consisted mostly of triglycerides. Cells showed higher variations in intracellular concentrations when incubated with oxLDL than in the model using albumin-complexed fatty acids. The most interesting difference is the detection of endocytic vesicles, which are observed upon the uptake of oxLDL. A depletion of d-TP from these vesicles over time was demonstrated. Furthermore, β -carotene and contributions from other lipids were found in the vesicles. A main constituent of the depleted vesicles was, thereby, phosphatidylcholine, which originates to a significant extent from the phospholipid monolayer of the incorporated lipoproteins. Most likely, different endocytic pathways of oxLDL into macrophages have been imaged. Though the scavenger pathway is dominating the oxLDL uptake, LPL-mediated endocytosis or phagocytosis of aggregated particles could have occurred as well, but size measurements of oxLDL after 72 h under cell culture condition showed no aggregation of the oxLDL particles. Further investigations using specific inhibition of certain endocytic pathways, for example, are required and planned.

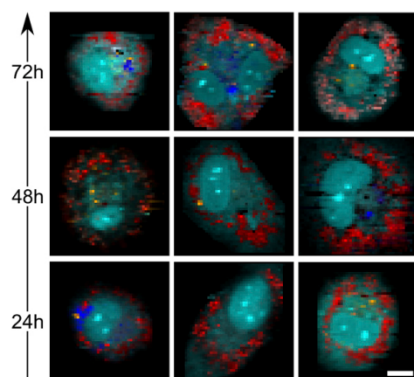



Fig. 5. Raman images of THP-1 macrophages incubated with d-TP-loaded oxLDL for 24, 48, and 72 h. Protein (cyan) lipid droplets containing deuterated lipids (red), endocytic vesicles (orange), and high β -carotene-rich components (blue) are depicted. Scale bar: 10 μm .



In conclusion, β -carotene was found to serve as a potential marker for the uptake of oxLDL by human macrophages. The storage of fatty acids released from triglycerides in oxLDL can be followed using Raman imaging. Derived from the endocytic uptake, vesicles were found. For the first time, the exchange of lipids between these vesicles and lipid droplets has been demonstrated by imaging at the subcellular level. The transfer into a microfluidic setup with a dynamic flow of lipoproteins over adherent macrophages can be another interesting step toward conditions better simulating the situation in vivo. 

REFERENCES

- Di Pietro, N., G. Formoso, and A. Pandolfi. 2016. Physiology and pathophysiology of oxLDL uptake by vascular wall cells in atherosclerosis. *Vascul. Pharmacol.* **84**: 1–7.
- Zhao, YY., H. Miao, X.-L. Cheng, and F. Wei. 2015. Lipidomics: novel insight into the biochemical mechanism of lipid metabolism and dysregulation-associated disease. *Chem. Biol. Interact.* **240**: 220–238.
- Li, L., J. Han, Z. Wang, J. Liu, J. Wei, S. Xiong, and Z. Zhao. 2014. Mass spectrometry methodology in lipid analysis. *Int. J. Mol. Sci.* **15**: 10492–10507.
- Fukuta, M., A. Ono, Y. Nawa, W. Inami, L. Shen, Y. Kawata, and S. Terekawa. Cell structure imaging with bright and homogeneous nanometric light source. *J. Biophotonics*. Epub ahead of print. June 8, 2016; doi:10.1002/jbio.201500308.
- Haka, A. S., V. C. Barbosa-Lorenzi, H. J. Lee, D. J. Falcone, C. A. Hudis, A. J. Dannenberg, and F. R. Maxfield. 2016. Exocytosis of macrophage lysosomes leads to digestion of apoptotic adipocytes and foam cell formation. *J. Lipid Res.* **57**: 980–992.
- Zhang, H., Z. Zhai, H. Zhou, Y. Li, X. Li, Y. Lin, W. Li, Y. Shi, and M.-S. Zhou. 2015. Puerarin inhibits oxLDL-induced macrophage activation and foam cell formation in human THP1 macrophage. *BioMed Res. Int.* **2015**: 403616.
- Hermes, A., M. Bosch, N. Ariotti, B. J. N. Reddy, A. Fajardo, A. Fernández-Vidal, A. Alvarez-Guaita, M. A. Fernández-Rojo, C. Rentero, F. Tebar, et al. 2013. Cell-to-cell heterogeneity in lipid droplets suggests a mechanism to reduce lipotoxicity. *Curr. Biol.* **23**: 1489–1496.
- den Hartigh, L. J., J. E. Connolly-Rohrbach, S. Fore, T. R. Huser, and J. C. Rutledge. 2010. Fatty acids from very low-density lipoprotein lipolysis products induce lipid droplet accumulation in human monocytes. *J. Immunol.* **184**: 3927–3936.
- Stiebing, C., C. Matthäus, C. Krafft, A.-A. Keller, K. Weber, S. Lorkowski, and J. Popp. 2014. Complexity of fatty acid distribution inside human macrophages on single cell level using Raman microspectroscopy. *Anal. Bioanal. Chem.* **406**: 7037–7046.
- Matthäus, C., C. Krafft, B. Dietzek, B. R. Brehm, S. Lorkowski, and J. Popp. 2012. Noninvasive imaging of intracellular lipid metabolism in macrophages by Raman microscopy in combination with stable isotopic labeling. *Anal. Chem.* **84**: 8549–8556.
- van Manen, H.-J., Y. M. Kraan, D. Roos, and C. Otto. 2005. Single-cell Raman and fluorescence microscopy reveal the association of lipid bodies with phagosomes in leukocytes. *Proc. Natl. Acad. Sci. USA.* **102**: 10159–10164.
- Eberhardt, K., C. Stiebing, C. Matthäus, M. Schmitt, and J. Popp. 2015. Advantages and limitations of Raman spectroscopy for molecular diagnostics: an update. *Expert Rev. Mol. Diagn.* **15**: 773–787.
- Kochan, K., E. Maslak, C. Krafft, R. Kostogryś, S. Chlopicki, and M. Baranska. 2015. Raman spectroscopy analysis of lipid droplets content, distribution and saturation level in non-alcoholic fatty liver disease in mice. *J. Biophotonics.* **8**: 597–609.
- Silge, A., T. Bocklitz, R. Ossig, J. Schnekenburger, P. Röscher, and J. Popp. 2016. The interaction of an amino-modified ZrO₂ nanomaterial with macrophages—an in situ investigation by Raman microspectroscopy. *Anal. Bioanal. Chem.* **408**: 5935–5943.
- Dai, Y., G. Condorelli, and J. L. Mehta. 2016. Scavenger receptors and non-coding RNAs: Relevance in atherogenesis. *Cardiovasc. Res.* **109**: 24–33.
- Moore, K. J., F. J. Sheedy, and E. A. Fisher. 2013. Macrophages in atherosclerosis: a dynamic balance. *Nat. Rev. Immunol.* **13**: 709–721.
- Goldberg, I. J. 1996. Lipoprotein lipase and lipolysis: central roles in lipoprotein metabolism and atherogenesis. *J. Lipid Res.* **37**: 693–707.
- Makoveichuk, E., S. Castel, S. Vilaró, and G. Olivecrona. 2004. Lipoprotein lipase-dependent binding and uptake of low density lipoproteins by THP-1 monocytes and macrophages: Possible involvement of lipid rafts. *Biochim. Biophys. Acta.* **1686**: 37–49.
- Lorkowski, S., and P. Cullen. 2007. Atherosclerosis: Pathogenesis, Clinical Features and Treatment. eLS. John Wiley & Sons, Ltd., Chichester, UK.
- Melzer, S., R. Ankri, D. Fixler, and A. Tamok. 2015. Nanoparticle uptake by macrophages in vulnerable plaques for atherosclerosis diagnosis. *J. Biophotonics.* **8**: 871–883.
- Dochow, S., H. Fatakdawala, J. E. Phipps, D. Ma, T. Bocklitz, M. Schmitt, J. W. Bishop, K. B. Margulies, L. Marcu, and J. Popp. 2016. Comparing Raman and fluorescence lifetime spectroscopy from human atherosclerotic lesions using a bimodal probe. *J. Biophotonics.* **9**: 958–966.
- Cicchi, R., E. Baria, C. Matthäus, M. Lange, A. Lattermann, B. R. Brehm, J. Popp, and F. S. Pavone. 2015. Non-linear imaging and characterization of atherosclerotic arterial tissue using combined SHG and FLIM microscopy. *J. Biophotonics.* **8**: 347–356.
- Etzion, Y., A. Hackett, B. M. Proctor, J. Ren, B. Nolan, T. Ellenberger, and A. J. Muslin. 2009. An unbiased chemical biology screen identifies agents that modulate uptake of oxidized LDL by macrophages. *Circ. Res.* **105**: 148–157.
- Chen, W.-W., C.-H. Chien, C.-L. Wang, H.-H. Wang, Y.-L. Wang, S.-T. Ding, T.-S. Lee, and T.-C. Chang. 2013. Automated quantitative analysis of lipid accumulation and hydrolysis in living macrophages with label-free imaging. *Anal. Bioanal. Chem.* **405**: 8549–8559.
- Schie, I. W., J. Wu, T. Weeks, M. A. Zern, J. C. Rutledge, and T. Huser. 2011. Label-free imaging and analysis of the effects of lipolysis products on primary hepatocytes. *J. Biophotonics.* **4**: 425–434.
- Al Gadban, M. M., K. J. Smith, F. Soodavar, C. Piansay, C. Chassereau, W. O. Twal, R. L. Klein, G. Virella, M. F. Lopes-Virella, and S. M. Hammad. 2010. Differential trafficking of oxidized LDL and oxidized LDL immune complexes in macrophages: Impact on oxidative stress. *PLoS One.* **5**: e12534.
- Morton, R. E., and D. B. Zilversmit. 1981. A plasma inhibitor of triglyceride and cholesteryl ester transfer activities. *J. Biol. Chem.* **256**: 11992–11995.
- Groener, J. E., R. W. Pelton, and G. M. Kostner. 1986. Improved estimation of cholesteryl ester transfer/exchange activity in serum or plasma. *Clin. Chem.* **32**: 283–286.
- R Core Team. 2015. R: A language and environment for statistical computing. Vienna, Austria. Available from: <https://www.R-project.org/>
- Beleites, C., and V. Sergio. 2015. hyperSpec: a package to handle hyperspectral data sets in R. R package version 0.98-20150911. Available from: <http://hyperspec.r-forge.r-project.org/>
- Beleites, C. 2015. cbmodels: Collection of “combined” models: PCA-LDA, PLS-LDA, PLS-LR as well as EMSC. R package version 0.5-20150729.
- McManus, C. 2013. unmixR: Spectral unmixing methods. R package version 1.0.
- Wickham, H. 2009. ggplot2: Elegant Graphics for Data Analysis. Springer, New York. Available from: <http://ggplot2.org>
- Ryabchykov, O., T. Bocklitz, A. Ramoji, U. Neugebauer, M. Foerster, C. Kroegel, M. Bauer, M. Kiehnopf, and J. Popp. 2016. Automatization of spike correction in Raman spectra of biological samples. *Chemometr. Intell. Lab. Syst.* **155**: 1–6.
- Martens, H., J. P. Nielsen, and S. B. Engelsen. 2003. Light scattering and light absorbance separated by extended multiplicative signal correction. Application to near-infrared transmission analysis of powder mixtures. *Anal. Chem.* **75**: 394–404.
- Winter, M. E. 1999. N-FINDR: An algorithm for fast autonomous spectral end-member determination in hyperspectral data. *Proc. SPIE.* **3753**: 266–275.
- Hedegaard, M., C. Matthäus, S. Hassing, C. Krafft, M. Diem, and J. Popp. 2011. Spectral unmixing and clustering algorithms for assessment of single cells by Raman microscopic imaging. *Theor. Chem. Acc.* **130**: 1249–1260.
- Krafft, C., L. Neudert, T. Simat, and R. Salzer. 2005. Near infrared Raman spectra of human brain lipids. *Spectrochim. Acta A Mol. Biomol. Spectrosc.* **61**: 1529–1535.



39. Rimm, E. B., and M. J. Stampfer. 2000. Antioxidants for vascular disease. *Med. Clin. North Am.* **84**: 239–249.
40. Marshall, C. P., and A. Olcott Marshall. 2010. The potential of Raman spectroscopy for the analysis of diagenetically transformed carotenoids. *Philos. Trans. A Math. Phys. Eng. Sci.* **368**: 3137–3144.
41. Cox, B. E., E. E. Griffin, J. C. Ullery, and W. G. Jerome. 2007. Effects of cellular cholesterol loading on macrophage foam cell lysosome acidification. *J. Lipid Res.* **48**: 1012–1021.
42. Loughheed, M., E. D. W. Moore, D. R. L. Scriven, and U. P. Steinbrecher. 1999. Uptake of oxidized LDL by macrophages differs from that of acetyl LDL and leads to expansion of an acidic endolysosomal compartment. *Arterioscler. Thromb. Vasc. Biol.* **19**: 1881–1890.
43. Matthäus, C., S. Schubert, M. Schmitt, C. Krafft, B. Dietzek, U. S. Schubert, and J. Popp. 2013. Resonance Raman spectral imaging of intracellular uptake of β -carotene loaded poly(D,L-lactide-co-glycolide) nanoparticles. *ChemPhysChem.* **14**: 155–161.
44. Bonetti, A., A. Bonifacio, A. D. Mora, U. Livi, M. Marchini, and F. Ortolani. 2015. Carotenoids co-localize with hydroxyapatite, cholesterol, and other lipids in calcified stenotic aortic valves. Ex vivo Raman maps compared to histological patterns. *Eur. J. Histochem.* **59**: 2505.
45. Verma, S. P., J. R. Philippot, B. Bonnet, J. Sainte-Marie, Y. Moschetto, and D. F. Wallach. 1984. Resonance Raman spectra of beta-carotene in native and modified low-density lipoprotein. *Biochem. Biophys. Res. Commun.* **122**: 867–875.
46. Silge, A., E. Abdou, K. Schneider, S. Meisel, T. Bocklitz, H-W. Lu-Walther, R. Heintzmann, P. Rösch, and J. Popp. 2015. Shedding light on host niches: Label-free in situ detection of mycobacterium *gordonae* via carotenoids in macrophages by Raman microspectroscopy. *Cell. Microbiol.* **17**: 832–842.

6.4 Advantages and limitations of Raman spectroscopy for molecular diagnostics: an update [CS4]

Katharina Eberhardt*, Clara Stiebing*, Christian Matthäus, Michael Schmitt, Jürgen Popp (2015)

Expert Rev Mol Diagn. 15(6): 773–787.

* geteilte Erstautorenschaft

Der Nachdruck der folgenden Publikation erscheint mit freundlicher Genehmigung von Taylor & Francis.

Erklärung zu den Eigenanteilen der Promovendin sowie der weiteren Doktoranden/ Doktorandinnen als Koautoren an den Publikationen und Zweitpublikationsrechten bei einer kumulativen Dissertation

| Doktoranden | Katharina Eberhardt | Clara Stiebing |
|--|---------------------|----------------|
| Schreiben des Manuskripts | x | x |
| Vorschlag Anrechnung Publikationsäquivalente | | 0,5 |

EXPERT
REVIEWS

Advantages and limitations of Raman spectroscopy for molecular diagnostics: an update

Expert Rev. Mol. Diagn. 15(6), 773–787 (2015)

Katharina Eberhardt^{1,2,‡},
Clara Stiebing^{1,2,‡},
Christian Matthäus^{1,2},
Michael Schmitt² and
Jürgen Popp^{*1,2}

¹Leibniz Institute of Photonic
Technology (IPHT),
Albert-Einstein-Straße 9,
07745 Jena, Germany

²Institute of Physical Chemistry and
Abbe Center of Photonics, Friedrich
Schiller University Jena, Helmholtzweg
4, 07743 Jena, Germany

*Author for correspondence:
Tel.: +49 3641 206 300
Fax: +49 3641 206 399
juergen.popp@ipht-jena.de

‡Authors contributed equally

Over the last decade, Raman spectroscopy has gained more and more interest in research as well as in clinical laboratories. As a vibrational spectroscopy technique, it is complementary to the also well-established infrared spectroscopy. Through specific spectral patterns, substances can be identified and molecular changes can be observed with high specificity. Because of a high spatial resolution due to an excitation wavelength in the visible and near-infrared range, Raman spectroscopy combined with microscopy is very powerful for imaging biological samples. Individual cells can be imaged on the subcellular level. *In vivo* tissue examinations are becoming increasingly important for clinical applications. In this review, we present currently ongoing research in different fields of medical diagnostics involving linear Raman spectroscopy and imaging. We give a wide overview over applications for the detection of atherosclerosis, cancer, inflammatory diseases and pharmacology, with a focus on developments over the past 5 years. Conclusions drawn from Raman spectroscopy are often validated by standard methods, for example, histopathology or PCR. The future potential of Raman spectroscopy and its limitations are discussed in consideration of other non-linear Raman techniques.

KEYWORDS: atherosclerosis • cancer diagnostics • cell imaging • disease recognition • infectious diseases • Raman spectroscopy

Spectroscopic methodologies are commonly used to support medical diagnostics. The well-established ones are absorption techniques for colorimetric assays to determine the concentrations of biomolecules in body fluids. Also widespread are the fluorescence-based techniques for qualitative and quantitative analysis. More recently, analytical methods that have been routinely used in natural sciences have drawn attention as potential tools for medical diagnostics. Among these are, for instance, mass spectrometry or vibrational spectroscopy. In mass spectrometry, the molecular weight is probed and the profile allows conclusions to be made about chemical changes associated with diseases. The concept of the approach is to use the very rich spectroscopic information as a basis for an improved diagnosis or, in other words, to combine classical chemical analysis with modern diagnostics. FIGURE 1 shows an overview of commonly used techniques to

characterize cellular metabolism or changes in intracellular composition. Often the application of just one technique is not nearly sufficient to prove a hypothesis about metabolic pathways. Raman micro-spectroscopy is unique in a sense that it offers direct spectroscopic information about the biomolecular composition of the sample without or with minimal preparation. As a consequence, various intracellular activities, such as cell death, apoptosis, proliferation, etc., can be monitored.

Raman spectroscopy as a variant of vibrational spectroscopy has become very popular for characterizing the biochemical changes associated with diseases. The methodology probes molecular vibrations which can be used for the identification of functional groups or compositional analysis. Meanwhile, there are hundreds of publications demonstrating that Raman spectroscopy can support gold standard techniques and may substantially improve

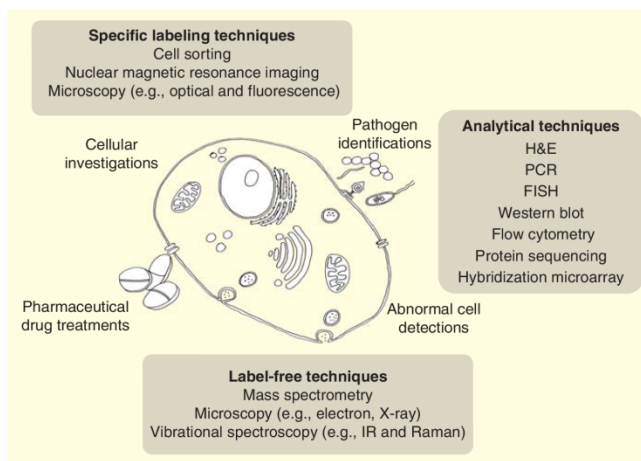


Figure 1. Common optical and biochemical methodologies for the analysis of biological samples with and without labels.
H&E: Hematoxylin and eosin; IR: Infrared.

clinical diagnostics in respect of time and cost reduction. Advances in modern optical technology have made it possible that Raman spectroscopy can be applied macroscopically and microscopically to study bulk samples as well as samples on the cellular level. Tissue sections or biopsies have been investigated for virtually every organ. Body fluids as well as single cells can be easily investigated. It is important to notice at this point that Raman spectroscopy as a label-free technique is not *per se* a methodology that searches for certain marker molecules. This may be possible in a few cases, where the disease-associated molecules have very specific spectral properties. Instead Raman spectroscopy is able to detect minute changes in the diseased cell or tissue due to the alteration in biochemistry, and is thus related to molecular biochemistry. These spectral changes are often very small and not distinguishable by the naked eye. Therefore, very often, multivariate data analysis is required.

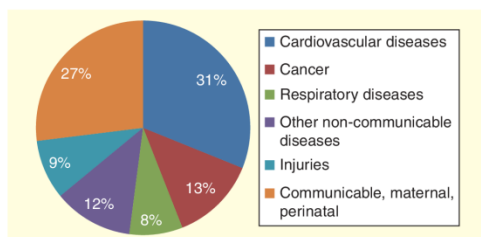


Figure 2. Global causes of deaths.
Adapted with permission from [1].

Principally, there are two complementary approaches possible that sort the data sets mathematically according to similarity or dissimilarity. The results can then set the basis for a classification into diseased and normal species.

There are numerous detection techniques and the advances in medicine have been tremendous, especially with the development of the life sciences since the 90s. However, every analytical technique suffers from certain drawbacks, such as low sensitivity or specificity. Often the analytical routines are time consuming or expensive. The review will attempt to address in what particular diagnostic situation Raman spectroscopy can be applied to improve the diagnosis. Diseases are usually grouped according to their causes and pathological symptoms. Today, the most common causes of death worldwide are predominantly related to either cardiovascular dysfunction or the development of cancer, as shown in Figure 2 [1].

The third largest group, which accounts especially for developing countries, is infectious diseases. Because of the dominance of these types of diseases, the following subsections will focus on the latest development or experimental achievements of Raman spectroscopy in these areas.

The first section will concentrate on intravascular imaging and review the potential of Raman spectroscopy to detect atherosclerotic plaques and differentiate between different plaque types. The second section will review several recent approaches in Raman spectroscopy to diagnose cancer, and along with that will introduce the concept and importance of multivariate data analysis. Finally we will address the latest advances of Raman spectroscopy on the single-cell level. Here, the amount of publications is extremely numerous and the addressed subjects range from, for example, single-cell imaging and cell differentiation to cell sorting. The section will first introduce the subject of Raman spectroscopy of cells in general and in comparison with other established techniques, and then review the different Raman methodologies according to their application. The possibility to investigate metabolic changes on the cellular level using Raman spectroscopy overlaps with different areas of biology, medicine and pharmacology, which is illustrated in Figure 3.

Atherosclerosis

Atherosclerosis is one of the most common cardiovascular diseases, usually caused as a consequence of energy storage excess and aging. Due to aging and oxidative stress, the arterial membranes become susceptible to deposition and permeation of various lipids circulating through the bloodstream, as well as crystalline calcium, usually in the form of calcium apatite. This process is followed by an accumulation of monocytes, a type of

white blood cells that differentiate into macrophages, which are responsible for lipid decomposition within tissues. If these cells are overwhelmed with metabolic stress, the subsequent cell death and cellular debris contributes to the arterial swelling. Continuous swelling can lead to the rupture of these plaque depositions, with often fatal consequences such as heart attack or stroke. The inner arterial plaque composition can vary according to the various risk factors, for instance, hypertension, hyperlipidemia, insulin resistance, smoking or obesity. Furthermore, different types of medication will also have an influence on the composition and evolution of these depositions. To correlate the composition of plaque depositions with certain disease patterns, long-term studies of plaque biopsies may offer potential insight for diagnostic strategies and applications. One of the greatest challenges in cardiology is the differentiation between different types of plaques. As mentioned, the biochemical composition of these plaques can vary to a great extent and can range from lipids with or without structure, such as cholesterol, to inorganic material, such as crystalline calcium. Also, the above-described cellular debris from mainly white blood cells is an important contributor. From post-mortem studies, cardiologists can rank the plaque morphology and compositional parameters according to the associated risk of a plaque rupture. However, this is so far not possible for *in vivo* diagnostics.

Currently, the diagnostic instrumentation used to detect and image the formation of atherosclerotic plaques involves invasive catheter-based techniques that also accompany intravascular surgery. The most common method is X-ray monitoring supported by contrast agents that visualize the blood flow against the surrounding tissue. The contrast agent is needed in rather large concentrations and has to be administered at the site of interest through a catheter, usually inserted into the arteria femoralis of the lower part of the groin. These catheters can also serve as a channel to insert probes for intravascular imaging. Today two methodologies are available. Intravascular ultrasound (IVUS) delivers already a better contrast of the plaque topography and morphology than the X-ray contrast. More recently, optical coherence tomography based on interferometry has become popular. Optical coherence tomography exhibits so far the best optical resolution with a penetration depth of about 1 mm. In the event that a person is diagnosed with atherosclerosis, it is possible to reintroduce a better blood flow by widening the affected areas by introducing high pressure through a balloon. A more permanent solution is an implantation of a stent, which usually consists of a metal, often coated with biodegradable polymers to prevent inflammation.

All three imaging techniques are invaluable for an onsite detection and diagnosis of atherosclerotic plaque depositions. However, they mainly deliver black and white images and provide no information about the biochemical composition of the plaques. To diagnose the biochemistry of plaques would not only be of great value in order to estimate the risk factor of a cardiovascular event associated with the plaque stability, but would also offer the possibility of a more personalized

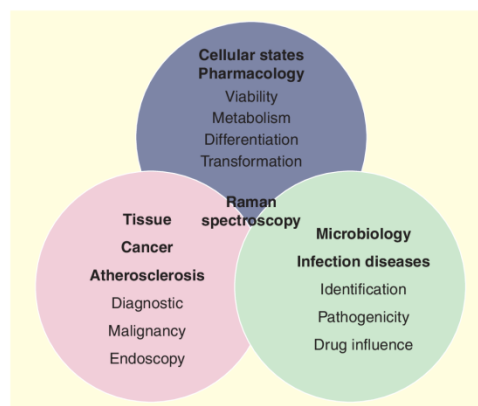


Figure 3. Biological, medical and pharmacological applications for Raman spectroscopy.

medication. Today patients are often treated with up to a dozen drugs, which can cause side effects. The possibility to use Raman spectroscopy coupled to modern fiber optics, introduced in a similar way as IVUS and optical coherence tomography probes, offers a great opportunity to investigate the biochemical composition at the plaque site through the guidance of a catheter.

The first successful attempts to obtain Raman signals from atherosclerotic plaque formations date back to the year 2000 and were reported by Buschman *et al.* Puppels and colleagues, well known for their experience in the field, carried out Raman probe based measurements on lamb and sheep *in vivo* [2]. The probes were facilitated mostly through a catheter (only in one case the probe was directly introduced through the heart). Spectra were obtained from the carotid artery, the femoral artery and the aortic arch. All Raman spectra were recorded using a near-infrared 830 nm excitation at an estimated power of 100 mW and an illumination time of 10 s. The spectra were compared with *ex vivo* data from human samples. The study showed for the first time the possibility to measure directly in the blood flow, without dominating fluorescence that one would expect from the blood itself. The group also experimented with a combined analysis of IVUS and Raman spectroscopy *ex vivo*, by first performing IVUS imaging and then subsequently collecting the Raman spectra through a microscopic setup, slicing the aorta along the blood flow for accessing the plaque.

The first *in vivo* Raman probe application of human atherosclerosis was published in 2006 by Motz *et al.* [3]. The experiments were performed during femoral bypass operations by insertion of the probe into the proximal anastomosis site of an artery flushed with saline. Spectra were acquired in contact with the artery wall directly at the incision, with the probe held perpendicular to the plaque. After a surgical incision along the length of the artery, Raman spectra were taken from the

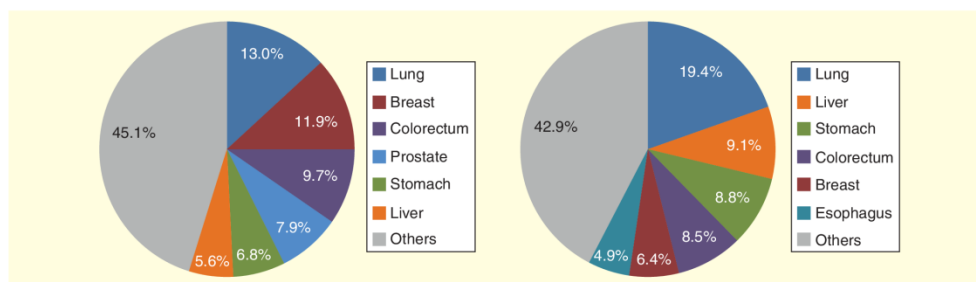


Figure 4. Estimated cancer incidence and mortality rate for both sexes worldwide in 2012 excluding non-melanoma skin cancer. Adapted from [11].

intimal surface prior to excision. During data acquisition, the room light was turned off. A 4-m-long optical fiber bundle, consisting of 16 fibers with a filter at the distal end and an optical ball lens, resulting in a spatial resolution of about 1 mm was used. The excitation wavelength was 830 nm, the excitation power was around 100 mW and the integration time varied from 1 to 10 s. After the removal of the plaque, the tissue was subjected to standard histopathological examination. In order to quantify the spectral contributions of the different plaque components, a least-squares fitting algorithm, developed by Buschman *et al.*, was employed which allowed for a quantitative characterization of normal, non-calcified, calcified, vulnerable and non-vulnerable plaques [4].

The next remarkable step for potential applications of Raman probe spectroscopy in humans was a multimodal approach published by Šćepanović *et al.* in 2011 [5]. Feld *et al.* developed a probe design that allows the combination of intrinsic fluorescence, diffuse reflectance and Raman spectroscopy. The studies were performed during femoral bypass and carotid endarterectomy surgeries. The experimental conditions for the Raman measurements were similar to the ones previously reported. For both types of surgery, the front viewing multimodal probe was inserted through the proximal anastomosis site for direct perpendicular contact. The artery was again flushed with saline. In total, 40 spectra were recorded from nine patients. After surgery, the biopsies were investigated *ex vivo* and compared with standard histopathology. Aim of the *ex vivo* study was to test the potential to differentiate between vulnerable and non-vulnerable plaques. The spectral correlation with the plaque morphology resulted in a sensitivity of 93% and a specificity of 72%.

The multimodal approach has recently gained popularity. Atherosclerotic plaque formations have been studied, for example, using two-photon fluorescence, second harmonic generation or coherent anti-Stokes scattering (CARS) spectroscopy. For examples of studies, see the following citations and references therein [6–9]. These imaging techniques may be potentially combined with Raman spectroscopy. We have recently shown the potential for the detection and characterization of

atherosclerotic plaques combining Raman and CARS spectroscopy [10]. The *in vivo* Raman studies were conducted on a White New Zealand rabbit model that was especially developed to study plaque formation *in vivo* by introducing a high cholesterol diet. The front viewing probe was inserted through a wire-guided catheter at the carotid artery of the animal. Several positions were measured within the aorta and the positioning was monitored by standard X-ray angiography. The experiment was repeated on the extracted and formalin-fixed aortas after perfusion. The positions at which the Raman spectra exhibited distinct lipid features were sectioned for histopathology. For the *ex vivo* CARS microscopy experiments, the lipid-rich regions were cut vertically along the blood flow in order to record $500 \times 500 \times 50 \mu\text{m}^3$ 3D depth profiles. Lipid-rich regions were compared with aorta sections with no plaque formations by recording the images in resonance with the CH stretching maxima for lipids and proteins around 2850 and 2930 cm^{-1} , respectively.

Cancer

Starting with the mutation of a single cell, cancer develops in multiple stages and leads to a tumor which can occur everywhere in the body. Tumors can be classified into different types:

- non-malignant or benign (non-cancerous),
- premalignant (precancerous) and
- malignant (cancerous).

The main risk factors are use of alcohol and tobacco, unhealthy food and physical inactivity. Also infections, for example, with hepatitis C virus, or radiation exposure can be activators. Even age plays a role since cellular repair mechanism works less efficiently with age. The survival rate depends on the type and place of the cancer and significantly on the time of diagnosis. Metastases are the major cause of death by cancer.

The most common cancer is lung cancer with an incidence of 13%, which as well has the highest mortality rate of 19.4% for all cancer-related deaths excluding non-melanoma skin cancer (FIGURE 4). Following this are breast and colorectal cancer,

but they less often lead to death (fifth and fourth highest mortality rate, respectively). Liver cancer has the second highest mortality rate (9.1%) [11].

Cancer cells and later tissue regions are different in their chemical composition and morphology, compared to healthy tissue. The so-called tumor markers, which are overexpressed or exclusively built by the affected cells, have been discovered by molecular diagnostic techniques. Until now, these markers only help to diagnose existing tumors and trace the progress of the disease. They do not exist for all types and it is not possible to diagnose cancerous lesions in early stages. Tumor markers can be found in body fluids or tissue sections. Nowadays, the main goal is to identify tumor markers and/or genetic mutations to implement personalized therapy. Examples of diagnostic techniques which examine genetic mutations are PCR and FISH.

The gold standard for cancer diagnostics is histopathology, which is based on the visual investigation of tissue biopsies, and is therefore invasive. Through specific staining, for example, with hematoxylin and eosin, certain areas or molecules get highlighted and a pathologist can diagnose the sample. In immunohistopathology, specific antibodies for known tumor markers are used and often combined with dyes for better visualization. Disadvantages of histopathology, in general, are the invasiveness of the procedure, the time-consuming sample preparation and the subjectivity of the pathologists.

Raman spectroscopy is gaining more popularity in the research field of cancer diagnostics. It adds the possibility to measure biological samples non-destructively without labeling and *in vivo* depending on the location of the tumor. The potential to investigate instantly without the need of biopsies is a huge advantage compared to histopathology. The lapse of time until the final diagnosis can be shortened significantly. Of great importance is the diagnosis of premalignant stages for early treatment. Raman spectroscopy is also promising as an assisting tool for the pathologist. *Ex vivo* Raman measurements on biopsies could help the pathologist to identify the tumor margins fast and more precise. Many studies involve the comparison of Raman spectra with histology [12–16]. Since biochemical changes only lead to subtle changes in the Raman spectra, statistical methods are necessary to extract diagnostic information [17,18].

FIGURE 5 shows the typical processing pathway of Raman spectra and examples of statistical methods used for cancer diagnostics. While unsupervised methods only use the spectra, supervised methods use additional information obtained by gold standards.

Principal Component Analysis (PCA) is a frequently used unsupervised method. The output spectra are called principal

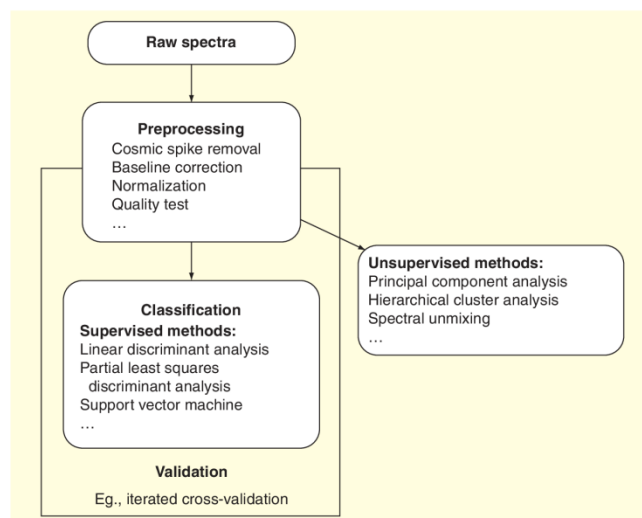


Figure 5. Typical processing pathway of Raman spectra during statistical analysis in cancer diagnostics.

components, which display the variance in the dataset where the first component accounts for the highest variability in the data. PCA is often used to reduce the number of variables and get a first estimation of the data. As a second step, a supervised method with the input of the principal components and the histopathological results can lead to a classification of the tissue or cells in question.

Next to statistical tools, there are also so-called biochemical tools which are based on the fitting of reference or pure component spectra to the tissue or cell spectra in question [19–22]. The goal is to determine the change in concentration of the components between malignant and non-malignant stages. Least-squares fitting models are used to reconstruct spectra through linear combinations of various pure component spectra. Development of cancer from non-malignant to malignant stages can then be interpreted through the increase or decrease of certain components, or tumor markers, in the cell or tissue. Since biochemical changes are thought to be continuous, the detection of premalignant stages could be improved. Stone *et al.* demonstrated the potential of this fitting technique by investigating gross biochemical changes to quantify the process of carcinogenesis in the bladder and the prostate gland [19]. Representative constituents, for example, actin, collagen I and III, triolein, DNA, cholesterol and more, were purchased and the Raman spectra fitted to the mean tissue spectra of each pathology obtained from *ex vivo* biopsies with an ordinary least-squares fitting algorithm. Within the bladder and the prostate gland, they identified an increase in DNA, nuclear to cytoplasm ratio, cholesterol and triolein from normal to

malignant tissue. Cholesterol was chosen as an indication of necrosis, which was found to align with the results. The authors found that not only from benign to malignant stages, but also with increased severity of the disease, the concentration of cholesterol increased, hinting that more necrotic areas were present. Collagen was found to decrease in the bladder tissue during the progression to malignant stages. These findings show the strong potential for Raman spectroscopy as a fast *in vivo* diagnostic tool. It should not be neglected that a drawback of this method is the decision of which pure components are used as representatives for the tissue type in question. Only the components which were decided upon can be detected. Different Raman cross sections of the pure components should be considered as well, since they lead to different intensities in the Raman spectrum. Hence, the concentration values are only estimations and should not be treated as real concentration values.

Cancer research using Raman spectroscopy has mostly been focused on statistical methods where the obtained spectral range is used completely to discriminate between different pathologies, rather than using specific bands fitted to pure components. In the following text, we present research on cancer in hollow organs, solid and less-accessible cancer, and skin cancer.

A main focus of research is on the design of fiber-optic Raman probes that can be implemented during endoscopy and enables the introduction of *in vivo* measurements of cancer in hollow organs [23–25]. Short *et al.* designed a Raman probe for *in vivo* detection of lung cancer during autofluorescence imaging [26]. Their goal was to implement Raman spectroscopy to white light and autofluorescence bronchoscopy. Special filter arrangements were necessary to block the generation of second-order spectra due to the blue excitation light necessary for autofluorescence imaging, since it is important to give the physician the possibility to see the lung tissue at all times. A 785 nm diode laser was used for Raman excitation, which also caused autofluorescence originating from the lung tissue, most likely due to hemoglobin or other fluorophores. The autofluorescence introduced problems for the detection mainly in the fingerprint region. The contributions were much lower in the high-frequency range from 1500 to 3400 cm^{-1} . Although the higher region features fewer bands, the potential of this Raman approach was demonstrated for *in vivo* diagnosis of lung cancer by reducing the false positives of autofluorescence bronchoscopy in a pilot study published few years later [27].

In 2014, Bergholt *et al.* published results obtained during an *in vivo* diagnostic trial to classify dysplasia in Barrett's esophagus [28]. Raman spectra had been collected during a study involving 450 patients undergoing endoscopy in the upper gastrointestinal tract. A beveled fiber-optic Raman probe setup with a 785 nm diode laser was used to record spectra from suspicious, epithelial lesions, with an integration time between 0.1 and 0.5 s in a range from 800 to 1800 cm^{-1} with a resolution of 9 cm^{-1} . After the Raman measurements, biopsies were taken and sent to histopathology for assessment. A partial least-squares discriminant analysis gave a sensitivity of 87% and

specificity of 84.7% for the discrimination of normal columnar-lined epithelium, non-dysplastic Barrett's esophagus and high-grade dysplasia in Barrett's esophagus. Through implemented software, data processing can be performed and the results displayed in real time on the computer screen. Through an audio guidance, the operator knows if the Raman probe is in proper contact with the epithelium. The authors state that the Raman setup is easy to use, and experienced as well as novice clinicians are routinely using the device to gather more data.

During *in vivo* experiments, a high autofluorescence background of the tissue causes problems in the spectral analysis. The autofluorescence contribution is high for near-infrared excitation at 785 or 830 nm, which, on the other hand, allows safe laser exposure for the patient. Raman signal of fused silica due to the fiber probe itself is also contribution to the spectral background. Raman probes are often designed for either the fingerprint region between 600 and 1800 cm^{-1} or the high wavenumber region from ca. 1500 to 3600 cm^{-1} to overcome these problems with special filtering and gratings for the chosen region. A combination of the low and high wavenumber range was achieved by Huang and colleagues. Bergholt *et al.* developed a Raman probe which is capable of measuring both regions simultaneously with a spectral resolution ranging from 3 to 6 cm^{-1} [29]. Through the combination of customized volume phase holographic dual-transmission gratings, which are tilted against each other, the two wavenumber regions get focused on two vertical segments on the charge-coupled device camera. Hence, a simultaneous readout from 800 to 3600 cm^{-1} is achieved and through implemented software, real-time processing of the obtained spectra is possible. The authors tested their development *in vivo* on epithelial tissue of the head and neck and received a signal-to-noise ratio of 25 for the CH_2 deformation band of lipids and proteins at 1440 cm^{-1} with an integration time of 1 s.

Taketani *et al.* conducted a study on colon cancer with mice [30]. A miniaturized Raman endoscope system was developed to monitor tumor progression within the same mice over several weeks. The group identified changes in the lipid composition and collagen type I concentration, indicating that the molecular composition of the tumors changes as they progress. A PCA-linear discriminant analysis model was able to correctly discriminate tumor from healthy tissue in 86.8% of the cases. The main goal of this study was the investigation of therapeutic effects of anticancer drugs and medical treatment in general, and not necessarily the early detection of cancer which is not possible with this approach. Drawbacks of the employed experimental setup are the long exposure time of 60 s and a complex background correction procedure which is an important task to overcome for *in vivo* studies. Only mice with specific tumor configurations were chosen. Others with large tumors which did not allow the use of the endoscope were excluded.

Lloyd *et al.* investigated non-consensus tissue sections with a Raman fiber approach of *ex vivo* esophagus tissue [31]. As mentioned earlier, histopathological results depend on the pathologist evaluating the tissue section. Often, difficult cases where

the pathologist cannot make an assessment about the disease stage or is not in agreement with other pathologists, the so-called non-consensus pathologies, are excluded from testing Raman models. In most experiments, only samples with a consensus are evaluated and used for developing a statistical model. But often, these uncertain cases are the ones important for early detection and treatment since they mostly are in between two pathologies. As stated by Lloyd *et al.*, not only is using all collected samples more cost efficient, but implementing non-consensus pathology measurements can also improve the diagnostic performance of Raman spectroscopy.

Apart from cancer in hollow organs, which can be easily reached by fiber probes, Raman spectroscopy has also been applied to less-accessible cancers, for example, in breast, brain or liver, although most of this research has been performed on cancer cell lines or *ex vivo* tissue sections [32–36].

In 1996, Hawi *et al.* first discriminated normal and malignant human hepatocytes by Raman micro-spectroscopy [37]. Hepatocytes are the most abundant cells in liver and hepatocellular carcinoma (HCC) is the most common primary liver cancer. HCC cell line (HepG2) and tissue imprints were measured with a Raman micro-spectrometer and the intensity ratios evaluated. Main differences between healthy and cancerous samples were found in protein contributions. Over the years, not many studies have been published about liver cancer and Raman spectroscopy. In 2013, Taleb *et al.* investigated blood serum of cirrhotic patients to discriminate patients with and without HCC [38]. Through the application of a support vector machine, a sensitivity of 95% and specificity of 88% was reached for the freeze-dried serum drop preparation protocol. An overall accuracy of 92% was obtained. Also, in 2013, Gaggini *et al.* correlated the METAVIR scores for liver biopsies with the results obtained by Raman measurements [39]. The METAVIR scoring system grades liver lesions caused by hepatitis C infection based on histopathological assessment. Infection with hepatitis C virus is the leading cause of HCC development or liver cirrhosis. Raman spectra with an excitation of 830 nm in the range of 800–1800 cm^{-1} were collected at five points for each biopsy. Metabolic products of liver (e.g., quinone and porphyrin) and the fibrotic stage (e.g., concentration of collagen) allowed a discrimination of the biopsies based on the correlation of their METAVIR score with the Raman spectra.

Improvements have to be done to better implement Raman spectroscopy for the diagnosis of liver cancer, especially on tissue sections. A major disadvantage of liver tissue is the fluorescence background produced by it.

Raman micro-spectroscopy is a useful tool to investigate suspicious skin lesions. A clinical study of 453 patients was performed and published in 2012 by Lui *et al.* to investigate different types of skin cancer by a home-built Raman setup [40]. The instrumentation allowed an acquisition time of approximately 1 s and software was implemented to preprocess the spectra immediately. This gives the possibility to investigate skin lesions in real time. The results obtained by Raman

spectra and statistical analyses were compared with standard diagnosis of histopathology or visual inspection by a dermatologist. Various skin lesions with different disease stages were investigated and discriminated by multivariate analysis tools, as for instance, partial least squares. The differentiation of malignant from benign skin lesions was the focus of their study to improve the *in vivo* diagnosis of skin lesions and reduce the number of necessary biopsies. At a sensitivity of 90%, the specificity in all investigated cases was higher than 63%.

Since skin pigmentation has not just an effect on light scattering but also on biochemical composition (mainly melanin concentration), malignant carcinoma and basal cell carcinoma (BCC) from patients with different skin types were investigated [41]. No differences in the obtained Raman spectra were detected after appropriate preprocessing.

Distinguishing between tumoral and peritumoral regions in tissue sections is important to improve the surgical accuracy while removing cancerous tissue. The morphological changes in peritumoral regions are only marginal, which makes the assessment through histopathology difficult. Resected tissue from cancer patients are evaluated by pathologists to check whether the cancer has been removed completely or another surgery has to be done. Thereby, they follow guidelines on how much healthy tissue has to surround the cancerous lesion. Although the morphological changes are barely visible, biochemical changes occur in peritumoral tissue sites. Raman spectroscopy may make it possible to detect these changes and help the physician during surgery to better assess the tumor margins to reduce the risk of a follow-up surgery. In 2010, Ly *et al.* demonstrated the capabilities of polarization-sensitive Raman micro-spectroscopy in regard to tumoral and peritumoral tissue sites [42]. Additional information about ordered biomolecules like collagen can be obtained by measuring perpendicular and parallel polarized Raman spectra. Depolarization ratios at specific bands showed significant differences not only between tumor and healthy epidermis, but also between peritumoral and healthy dermis. Differences in parallel polarized Raman spectra were found in peritumoral regions depending on the distance from the tumor. Collagen seems to degrade on getting closer to the tumor and changes of the Amid III band at ca. 1300 cm^{-1} hint at modifications in the secondary structure of proteins. The authors, therefore, claim that they can distinguish peritumoral dermis in superficial and nodular BCC from healthy dermis and early detection of BCC would be possible. Furthermore, a better classification between tumor and healthy tissue was achieved by parallel polarized Raman spectra compared to conventional Raman spectroscopy.

A promising approach was followed by Kong *et al.* where autofluorescence was combined with Raman spectroscopic point measurements on skin tissue containing BCC [43]. To reduce the long measuring time necessary for acquiring Raman spectra of whole tissue sections, the group segmented the tissue by autofluorescence images taken at excitation wavelengths of 377 and 292 nm corresponding to collagen and tryptophan excitation. BCC exhibits more intense bands corresponding to

DNA, while normal dermis is dominated by collagen. By computing the ratio of these images, segments were applied and evaluated by an automated algorithm which sets Raman measuring points for suspicious regions. For the detection of BCC in tissue, a sensitivity of 95% and specificity of 94% was reached. In total, 500–1500 Raman spectra for a $1 \times 1 \text{ cm}^2$ tissue section with an integration time of 2 s were recorded, leading to a diagnosis time between 20 and 60 min. The authors also demonstrated the feasibility of this technique on tissue blogs, which makes long-lasting section procedures unnecessary. Future application during tissue-conserving surgery for quick assessment of tumor margins is planned.

This multimodal imaging approach yields high potential for cancer diagnostics by Raman spectroscopy. Other Raman applications like surface-enhanced Raman spectroscopy (SERS) [44], spatially offset Raman spectroscopy [45] and CARS [46–48] have been successfully applied for cancer diagnosis, but are not discussed in this review.

***In vitro* Raman spectroscopy on individual cells**

Raman spectroscopy at cellular and subcellular resolution has become a popular modality with widespread applications. Although the review focuses on *in vitro* applications concerning molecular diagnostics, a thorough overview, is challenging. Because Raman micro-spectroscopy offers a label-free imaging modality at the spatial resolution of conventional and even confocal microscopy, it has become an accepted technique also among biologists.

Cell morphology & intracellular investigations

The combination of optical microscopy with Raman spectroscopy allows for the visualization of intracellular components or organelle structures merely based on their biochemical composition. Although the spectral changes are minute, multivariate algorithms are able to discern the overall spectral patterns and translate them into an image. Thus, it is possible to visualize cellular organelles such as the nucleus, nucleoli, the perinuclear region, mitochondria or lipid droplets without the use of any external labels or dyes [49]. Changes in cellular organelles, for instance, in size, number, chemical composition or shape, can be used to discriminate individual cells at various cellular states or stages under the influence of stress. The analysis of morphometric changes by Raman spectroscopy can be useful to study the function and subcellular organization of organelles which can be relevant for drug and experimental evaluation, clinical diagnostics or prognosis. Recently, Schulze *et al.* have monitored morphological changes of nuclei and nucleoli simply based on univariate intensities of Raman features associated with proteins and nucleic acids [50]. Observing the distribution of proteins by plotting the intensities of a phenylalanine ring vibration at 1003 cm^{-1} against the intensities of nucleic acid vibrations for DNA and RNA at 783 and 809 cm^{-1} revealed that nucleoli of cancer cells were larger and more defined in contrast to embryonic stem cells. Imaging combined with PCA allowed identification of high intranuclear RNA clusters and

additionally nucleolar protein distribution. Ratios relative to nucleoli and nucleus may potentially be indicative to assess the drug influence of rRNA-induced blocking during clinical chemotherapy due to nucleolar integrity and extranuclear RNA levels. Stem cell research is also promising for potential drug discovery, proof-of-principles experiments in clinical studies and cell-based therapy [51,52]. Tan *et al.* investigated the potential of Raman spectroscopy to distinguish pluripotent cells, differentiated cells and embryonic stem cells, in order to understand reprogramming and dedifferentiation processes [53]. Comparing these cells with differentiated embryonic stem cell progeny demonstrated that induced stem cells were similar to pluripotent embryonic stem cells, based on their measured peak intensity profiles. Differentiated cells were distinguished from induced and embryonic stem cells based on the reduction of protein to nucleic acid ratio and determined by PCA. This implies that neither reprogramming nor genetic instabilities nor epigenetic differences lead to changes in protein expression levels. Subtle spectral differences were noted in induced pluripotent stem cells. Therefore, it is useful to elucidate these causes during various external conditions and the correlations with genetic and epigenetic factors.

The intensities of DNA-specific Raman bands are apparently correlated with the degree of DNA packing within the chromatin [54]. The chromatin is more condensed during cellular mitosis compared to all other phases of the cell cycle. Huser *et al.* utilized this phenomenon to investigate the DNA packing in individual human sperm cells, which correlates with their shape [55]. Cells from a healthy donor were analyzed non-destructively by Raman spectroscopy with 488 nm excitation wavelength, demonstrating excellent reproducibility of the spectral intensity variations from differently shaped heads for *in vitro* fertilization. A homogenous distribution of protein content within the nucleus and spatial efficiency of DNA packaging were observed whereby peak intensities of protein–DNA ratios varied between normally shaped heads. The findings indicate that Raman spectroscopy may be a valuable methodology to improve the evaluation of the quality of sperm cells for *in vitro* fertilization.

Apart from studies focusing on the molecular composition or organization of the nucleus, changes within the cytoplasm may as well be monitored. Konorov *et al.* reported Raman micro-spectroscopy of living cells under autophagy-inducing conditions [56]. Autophagy as a recycling mechanism of nutrients, protein aggregates, decomposition of organelles and pathogens is physiological relevant for cell survival under stress [57,58]. Studying the response of amino acid starvation in living cancer cells as a condition that triggers autophagy, the intensity ratio of 718 cm^{-1} Raman band associated with phospholipids was related to the 784 cm^{-1} band, which was suggested as a useful spectral marker of autophagy [56]. Recovery dynamics were monitored by Raman spectroscopy using a 785 nm excitation; additionally, the heterogeneity of starvation response was observed and further cellular processes such as apoptosis may influence the cellular composition.

Principally, Raman micro-spectroscopy can be coupled to microfluidic setups in order to analyze especially non-adherent cells spectroscopically. Subsequently, cells can be sorted according to their intrinsic biomolecular characteristics and stored for additional investigations. For recent proof-of-principle studies, refer [36,59–63].

Cellular analyses during infectious diseases

Apart from the non-communicable diseases that were the subject of earlier chapters, communicable or infectious diseases are of high importance, especially in developing countries. FIGURE 6 shows the years of life lost as a parameter of premature mortality rate by the frequency of death and the ages at which deaths occurred per 100,000 inhabitants for different WHO regions for the year 2012 [64]. In particular, there is a distinct difference in mortality caused by communicable diseases between Africa and the other regions. Comparing to an older WHO statistics report, the incidence of these diseases is approximately halved for Africa, from 80% in the year 2004 to ca. 45% in the latest report, but the incidence is still high [65].

Communicable diseases are caused by infectious agents such as viruses, bacteria and macro-parasites, for instance, nematodes or fungi. Among the most common transmissible diseases in developing countries are malaria, hepatitis, cholera, influenza and meningitis. Although the detection of these diseases is not always the greatest challenge, there are many disease-associated questions with regard to the spread or treatment of infections. Raman spectroscopy usually in combination with microscopy has shown great potential to investigate diseases caused by organisms on the tissue and cellular level. Malaria is one of the most devastating infectious diseases. One of the reasons is the resistance against common antimalarial drugs developed by the parasites. Therefore, it is important to understand the associated mechanisms of resistance on the molecular level. The group of McNaughton and Wood carried out a substantial amount of research studying the changes in red blood cells caused by the *Plasmodium falciparum* parasite. They investigated the interaction between quinoline antimalarial drugs and ferriprotoporphyrin IX which is hypothesized to hinder the formation of free heme aggregation within the red blood cells, essential for the parasite survival [66]. Binding of the drug with ferriprotoporphyrin, which is important for the efficiency of the quinoline derivatives, was investigated with Raman spectroscopy supported by density-functional calculations commonly performed to assist the interpretation of spectral changes. The findings showed formation of a salt bridge between the tertiary amino nitrogen of chloroquine and

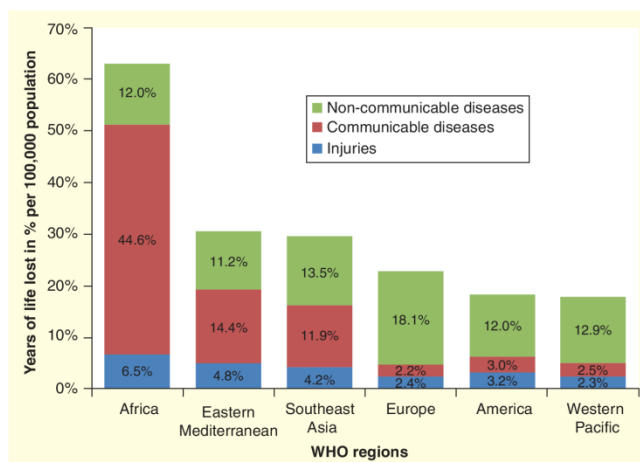


Figure 6. Premature mortality rates depicted as years of life lost in percentage caused by non-communicable, communicable diseases and injuries per 100,000 population in the year 2012 by WHO regions.

Adapted with permission from [64].

quinacrine and a propionate group of heme and different mechanisms of action of the different quinoline derivatives. In order to study the formation of the heme aggregation non-invasively within the natural environment, the group developed a setup in which single red blood cells are acoustically levitated [67]. The Raman spectra are then excited directly inside the single cells. Also, Kang *et al.* observed hemozoin (1374 cm^{-1}) distribution inside trophozoite stages in malaria-infected erythrocytes by Raman images [68]. Quantitative morphological and chemical sample information are provided by the combination of quantitative phase microscopy with confocal Raman microscopy, and thus, further cell developments and interactions in respect of blood disorders can be monitored.

Another possibility to generate Raman spectra with an enhanced spatial resolution is to utilize plasmon resonance effects at the surface of metals. One version of these surface-enhanced resonance Raman effects is tip-enhanced resonance Raman spectroscopy. The setup employs small cantilevers commonly used for atomic force microscopy and enables resolutions on the nanometer scale. Wood *et al.* utilized tip-enhanced resonance Raman spectroscopy to study heme aggregation or hemozoin formation in sectioned erythrocytes [69]. The spectral features observed were consistent with a five-coordinate high-spin ferric heme complex associated with the hemozoin formation. The technique has generally great potential as a new independent drug screening modality for detection of drugs binding to the hemozoin surface within the digestive vacuole of the malarial trophozoite. Furthermore, the group suggested a combination of Raman micro-spectroscopy with partial dark-field microscopy as a new modality for the detection of malaria [70]. The partial

dark-field effect improved the identification of potential parasites in thick blood films that may be overlaid by other cells and thus obscured using conventional bright-field microscopy. The Raman modality shows in addition potential to detect low-pigmented phases of the parasite's life cycle.

Another widespread bacterial infection is meningitis. Although there are treatment protocols available, a timely diagnosis and microbial examination is very important in order to initiate an efficient therapy. Harz *et al.* analyzed single bacterial cells from cerebrospinal fluids, which were examined to diagnose diseases or infections of the central nervous system [71]. By generating single-point Raman spectra using a microscope setup, the group was able to differentiate five meningitis pathogens. Subsequently, a meningococcal patient sample was used to prove that a diagnosis is possible on the basis of that reference database.

A great challenge in the molecular diagnosis of pathogens is to avoid time-consuming cell cultivation. Usually cellular subcultivation and identification by biological assays, like PCR-based techniques, take about 24 h, which can delay the correct medication and treatment substantially. Raman micro-spectroscopy in combination with sophisticated multivariate data analysis offers the possibility to characterize and identify bacteria on the single-cell level. One way of subcultivating bacterial pathogens is by isolation from body fluids. Kloß *et al.* used Raman micro-spectroscopy to identify infectious pathogens from the urinary tract [72]. Usually, a diagnosed infection is immediately followed by an antimicrobial treatment. However, this procedure could lead to rising antibiotic resistances due to selection pressure. Based on a reference database of 11 types of bacteria and a support vector machine algorithm, infections of 10 patients were identified correctly with an accuracy ranging from 66.7 to 97.8%. The overall time frame for the analysis was 2 h, which is a great improvement not only in terms of time but also with respect to costs. Another approach utilizing Raman micro-spectroscopy for the identification of pathogens recovered from the urinary tract involved its combination with dielectrophoresis [73]. Neugebauer and colleagues designed a dielectrophoresis setup which allowed for the direct translational manipulation of bacteria in suspension by electrical fields. Again in combination with multivariate data analysis, the group demonstrated a possible differentiation of different types of bacteria taking *Escherichia coli* and *Enterococcus faecalis* as examples. In principle, these microfluidic setups in combination with microscopy can be automated to a great extent for routine clinical applications.

A very severe and life-threatening infectious disease, which has become a major problem in intensive care units in hospitals, is sepsis. Sepsis is a potentially fatal whole body inflammation with subsequent overwhelming immune response, also referred to as systemic immune response syndrome. However, systemic immune response syndrome cannot only be induced by pathogens, but also by several other sterile, non-infectious stimuli such as invasive surgery, trauma or burns. For adequate and correct treatment, a differentiation is very important. Here,

the time aspect or, in other words, a rapid diagnosis is essential in most of the cases, as the survival rate and the chance for a positive treatment decrease within a few hours. Because of this, alternative diagnostic modalities would greatly improve the therapeutic success. Neugebauer *et al.* demonstrated the feasibility of Raman micro-spectroscopy to differentiate sepsis from systemic immune response syndrome on blood plasma samples from 70 intensive care unit patients [74]. Based on a PCA-linear discriminant analysis classification model, patients were diagnosed correctly with a sensitivity of 1.0 and a specificity of 0.89. The results were subsequently confirmed on an independent dataset with a prediction accuracy of 80%.

Furthermore, the increased occurrence of nosocomial infections induced by several multi-antibiotic resistant bacterial strains is of great concern worldwide. Reliable and cost-effective typing methods are, therefore, mandatory. With a custom-built Raman setup, Puppels, Maquelin and colleagues demonstrated a rapid, easy-to-handle and reliable alternative compared to the gold standard technique in bacterial typing (pulsed-field gel electrophoresis) used in clinical laboratories [75–77]. With high correlation to pulsed-field gel electrophoresis (96%), high discrimination power (D value = 0.989), as well as good reproducibility (95%) and correct classifications (96% true negative), these studies demonstrated the advantage of Raman typing for continuous monitoring in hospitals and usage in outbreak settings. Isolates were independently clustered against the presence of certain β -lactamase genes, like the CTX-M-15 resistance gene. Whereas several unique isolates belonged to the same repetitive sequence-based PCR type, suggested that a common source can be identified by Raman spectroscopy. The competence of Raman spectroscopy to identify the presence of a predominant clone and, thus, a suggested common source was discussed.

Raman spectroscopy has also been employed to non-invasively investigate intracellular metabolites within intact *Chlamydia*-infected cancer cells. The associated intracellular pathogens that reside in eukaryotic host cells within membrane-bound parasitophorous vacuoles were spectroscopically characterized. The analysis by conventional methods is usually complicated since the inclusion membranes are non-permeable to fluorescent tracers. The high spatial resolution of Raman micro-spectroscopy allows a monitoring of microbial and host activity during the intracellular infection [78].

With a spatial resolution of around half a micron, Raman spectroscopy is especially suited for the diagnosis of bacterial infections. For the direct characterization of single viruses, the resolution is generally not sufficient. However, by utilizing the above-mentioned plasmon resonance effect on metal surfaces, surface-enhanced Raman spectroscopy spectra of very good quality may be obtained. For examples of the identification of viruses using surface-enhanced Raman spectroscopy, refer the following articles and the references therein [79–82].

Characterization of drug interaction on single-cell level

Understanding the biochemical processes inside cells and the impact of pharmaceutically active compounds and their

interactions is of major importance for future personalized medicine. Common biological analytical techniques offer invaluable insight into the mode of potential drug actions. However, the associated sample preparation causes cell damages and unwanted effects can occur because of the introduction of external dyes or fluorescent labels. In order to obtain cellular information during pharmaceutical drug treatments without labeling or extensive and time-consuming preparation steps or biological sample destruction, Raman spectroscopy has been widely successfully applied in recent years. Time-related molecular changes have been measured during chemotherapeutic drug-induced apoptosis in breast cancer cells by Zoladek *et al.* using confocal Raman spectroscopy with near-infrared excitation wavelength (785 nm) [83]. Spectral images of etoposide-treated cells were obtained for different incubation times over 6 h. High accumulation of membrane phospholipids inside the lipid bodies was indicated by a characteristic band (719 cm^{-1}) and highly unsaturated non-membrane lipids were observed by the intensities of the C = C stretching vibrations (1659 cm^{-1}). Increased signal intensities of a typical DNA band (788 cm^{-1}) during apoptosis were attributed to chromatin condensation. In comparison, Buckmaster *et al.* monitored over 48 h apoptotic response of etoposide on cell-based biosensor applications utilizing patterned single-cell arrays [84].

Another example for significant changes in Raman band intensities was observed in brain tumor cells [85]. Within 36 h, a drastic reduction by 87.5% of Raman peak intensities typical for proteins and DNA, at 1005 and 1342 cm^{-1} , respectively, was observed. These sharp isolated peak intensities can be used as biomarkers for cell death and it was found that surviving cells are capable to resist or recover from the drug treatment, as indicated by little or no peak reductions. Other biochemical changes related to cellular death were observed in real time by Raman spectroscopy in combination with support vector machine as a classification algorithm. Within minutes, biochemical changes were discriminated by toxin-induced apoptosis and necrosis caused by inoculation with etoposide and Triton X-100. The drug efficiency was compared for high and low temperature conditions.

Because of the high spatial resolution, which is comparable to confocal microscopy, subcellular organelles inside cells were monitored, assuming that variances in Raman spectra occur at local molecular level. DNA damages induced by vincristine exposure (0.01 – $10\text{ }\mu\text{M}$) were observed in lung adenocarcinoma cells, along with an upregulation of the bcl-2 protein [86]. Raman spectra indicated that vincristine intercalates with cellular DNA and the expressed anti-apoptotic protein promotes resistance to apoptosis at low doses ($<5\text{ }\mu\text{M}$). The IC_{50} analyzed by cell viability assays (MTT) was significantly lower and cell death mechanisms at low doses was ascribed by microtubule binding and associated dynamic changes [87].

Information of the cells' total molecular content can also be indicative for biomolecular changes occurring during drug exposure. Schie *et al.* compared local and global molecular information before and after doxorubicin exposure ($1\text{ }\mu\text{M}$) by

line-scanning Raman spectroscopy [88]. Major macromolecules of Jurkat T cells were identified by Vertex Component Analysis, indicating that relative local abundances of nucleic acid decreased, proteins remained constant and lipids increased within drug exposure time. In contrast, global to total nucleic acid content stayed relatively constant, whereas the protein and lipid content increased more than double in the drug-treated cells. Therefore, spectral information obtained from the entire cell is very useful to observe biochemical changes that can be missed by observing local cell regions.

Another study monitoring the apoptotic response induced on Jurkat T cells by doxorubicin indicated exposure time- and concentration-dependent changes in lipids, DNA and proteins of over 72 h [89]. In order to acquire Raman spectra of these non-adherent cells, laser tweezers were utilized. Similar results were observed by Lin *et al.* [90]. The study also indicated that the cytotoxicity of paclitaxel for lymphoma cells increased with drug dose. Fragmentation effects induced by docetaxel (2.5 – 100 nM) have also been measured on dried breast cancer cells [91]. Within the nucleus, a significant treatment-induced difference was assigned to DNA/RNA and amide I vibrations, at 785 and 1658 cm^{-1} , respectively, with an accuracy of 99.2%. The minimal detection limit of drug-induced spectral changes was determined to be 7.5 nM . Both studies demonstrate the ability of Raman spectroscopy combined with modern chemometrics to monitor ongoing chemotherapy, especially to measure quantitatively the quality of cytostatic drug treatments.

In summary, *in vitro* toxicological and pharmaceutical studies as well as time-dependent cellular processes of molecular changes can be analyzed in real time by Raman spectroscopy combined with modern chemometric approaches. As a control tool in the ongoing drug treatment therapy, the visualization and detection of drug effects on real patient samples allows for an optimization of personalized medicine. Raman spectroscopy can deliver useful spectroscopic information on the cellular and subcellular level. By implementing biosensor-Raman platforms, a quick and simple modality to assess cell responses of biochemical agents with high throughput can be developed. The obtained spectroscopic information can be very useful for biomedical applications in drug discovery or toxicology tests.

Expert commentary & five-year view

Over the past 5–10 years, Raman spectroscopy coupled with either microscopy or an optical setup that allows for fiber probe-based technology has developed beyond the proof of principle. The previous sections attempted to illustrate the state of the art in terms of both technical development as well as medical applications. Among the cited work by many research groups, there are numerous examples where the experimental level has left the academic environment and has now reached the clinics. Spectroscopically established molecular markers are used nowadays to identify premature changes in patient samples *in vitro* and *in vivo* to diagnose and treat at an early stage as well as to enhance recovery. TABLE 1 lists the general

Table 1. Advantages and disadvantages of Raman spectroscopy for molecular diagnostics.

| Advantages | Disadvantages |
|--|---|
| <ul style="list-style-type: none"> • Non-destructive, non-invasive (wavelength and power dependent) • Minimal sample preparation • Label free, no dyes and toxic waste products • High specificity • Simultaneous detection of macromolecules • Compatible with physiological measurements due to weak water interferences • <i>In vivo</i> fiber-optic applications (for hollow organs, blood vessels) • Suitable for chemical analysis, quantification, classification and imaging of biological samples | <ul style="list-style-type: none"> • Autofluorescence (sample dependent) • Low sensitivity • Weak Raman signals leads to long acquisition times • Slow imaging by point scanning • Video rate imaging almost impossible due to low scattering efficiency and long measurement times • Sophisticated data analysis often necessary |

advantages and disadvantages of Raman spectroscopy for the application of molecular diagnosis.

Most of the disadvantages of Raman spectroscopy are associated with the weakness of the effect, which results usually in rather long measurement times. The potential of damaging the sample due to the laser exposure, which depends on the excitation wavelength, has to be taken into account during the planning of the measurements. Biological samples, especially in case of *in vivo* measurements, are often investigated using the low-energy near-infrared wavelength for excitation (mainly 785 or 830 nm). Otherwise, typical Raman resonance effects, for instance, for Cytochrome *c*, can only be observed by using energy-rich 532 nm excitation. To prevent damages, for example, burning, decrease of the excitation power and setups with water immersion objectives are advised. Subsequently, the degree of damage can be investigated before and after the measurement by optical microscopy or with several viability assays, for example, by staining with fluorescent dyes like propidium iodide to differentiate apoptosis and necrosis against cell viability. The obtained spectral information one can acquire with Raman spectroscopy is beyond the reach of most other techniques, especially if applied under *in vivo* conditions. Therefore, clinical applications as well as upcoming commercialization have been observed over the last few years. Particularly considering the increasing number of nosocomial infections, Raman spectroscopy-based products are starting to be successfully used in clinical diagnostic laboratories. Rapid and reliable real-time

bacterial strain characterizations were done, for example, with the Bio Particle Explorer (rap.ID Particle Systems, Berlin, Germany) or SpectraCell RA[®] Analyzer (River Diagnostics, Rotterdam, The Netherlands).

Testing the potential of Raman spectroscopy for molecular diagnostics further will be the major scope for the next 5–10 years. The authors believe that if Raman spectroscopy finds its way into clinical settings, further issues such as instrument development and profitable marketing will have the chance to succeed. This involves larger studies that aim beyond 'the proof of principle'. In the case of intravascular characterization of atherosclerotic plaques, the main focus should now be the development of cost-efficient probes that fulfill the technical requirements for applications in humans. The main aspects are the probe length as well as its bending flexibility. For the diagnosis of cancer, again larger studies are needed in order to test the reliability of the statistical data evaluated, which is essential for diagnostic analysis. These clinical tests involving a sufficient number of patients are very rare to find. This is generally true for testing the potential in the diagnosis of infectious diseases. Here, the amount of basic academic research to study intracellular changes associated with the occurrence of diseases and subsequent drug treatment is by far not exhausted. For direct clinical applications, the fact that a reliable diagnosis can potentially be reached within a few hours, if not faster, is the greatest advantage over established culture-dependent protocols. To summarize, the application of Raman spectroscopy for molecular and medical diagnosis has reached a very crucial state and the next 10 years will show whether the technique will advance into routine clinical settings.

Financial & competing interests disclosure

The authors gratefully acknowledge the financial support by the Carl Zeiss Stiftung and the Jenaer Biochip Initiative 2.0 (JBCI 2.0). The project JBCI 2.0 (03IPT513Y) within the framework InnoProfile-Transfer – Unternehmen Region is supported by the Federal Ministry of Education and Research (BMBWF), Germany. The authors have no other relevant affiliations or financial involvement with any organization or entity with a financial interest in or financial conflict with the subject matter or materials discussed in the manuscript apart from those disclosed.

No writing assistance was utilized in the production of this manuscript.

Key issues

- Raman spectroscopy in combination with modern optical developments is a powerful tool for potential applications in molecular diagnostics.
- Raman spectroscopy provides unique and specific information about the biochemical composition of samples.
- Through development of fiber-optic probes, Raman spectroscopy can be combined with endoscopy.
- The potential of the diagnostic applications ranges from cardiovascular diseases to cancer diagnosis and diseases on single-cell level.
- Raman spectroscopy is a non-invasive or minimally invasive technique that can be applied *in vivo* and is especially suited for clinical applications.

References

Papers of special note have been highlighted as:

• of interest

•• of considerable interest

1. WHO. Global atlas on cardiovascular disease prevention and control. 2011. Available from: www.world-heart-federation.org/fileadmin/user_upload/documents/Publications/Global_CVD_Atlas.pdf [Last accessed 18 September 2014]
2. Buschman HP, Marple ET, Wach ML, et al. In vivo determination of the molecular composition of artery wall by intravascular Raman spectroscopy. *Anal Chem* 2000;72:3771-5
3. Motz J, Fitzmaurice M, Miller A, et al. In vivo Raman spectral pathology of human atherosclerosis and vulnerable plaque. *J Biomed Opt* 2006;11(2):021003
4. Buschman H, Motz J, Deinum G, et al. Diagnosis of human coronary atherosclerosis by morphology-based Raman spectroscopy. *Cardiovasc Pathol* 2001;10(2):59-68
5. Šćepanović O, Fitzmaurice M, Miller A, et al. Multimodal spectroscopy detects features of vulnerable atherosclerotic plaque. *J Biomed Opt* 2011;16(1):011009
6. Sowa M, Mostaco-Guidolin L, Smith M, et al. Nonlinear Optical Measurements of the Artery Wall: Parameters Related to the Progression of Atherosclerosis. *Meas Sci Rev* 2009;9(4):93-4
7. Wang H, Langohr I, Sturek M, Cheng J. Imaging and quantitative analysis of atherosclerotic lesions by CARS-based multimodal nonlinear optical microscopy. *Arterioscler Thromb Vasc Biol* 2009;29(9):1342-8
8. Ko A, Ridsdale A, Smith M, et al. Multimodal nonlinear optical imaging of atherosclerotic plaque development in myocardial infarction-prone rabbits. *J Biomed Opt* 2010;15(2):020501
9. Cicchi R, Matthäus C, Meyer T, et al. Characterization of collagen and cholesterol deposition in atherosclerotic arterial tissue using non-linear microscopy. *J Biophotonics* 2013;7(1-2):135-43
10. Matthäus C, Dochow S, Bergner G, et al. In vivo characterization of atherosclerotic plaque depositions by Raman-probe spectroscopy and in vitro coherent anti-stokes Raman scattering microscopic imaging on a rabbit model. *Anal Chem* 2012;84(18):7845-51
- **In vivo study on a rabbit model which demonstrates the potential of a fiber-optical approach with Raman spectroscopy to detect and characterize atherosclerotic lesions.**
11. Ferlay J, Soerjomataram I, Ervik M, et al. Cancer Incidence and Mortality Worldwide: IARC CancerBase No. 11. International Agency for Research on Cancer. Lyon, France. 2013. Available from: <http://globocan.iarc.fr> [Last accessed 19 July 2014]
12. Guze K, Pawluk HC, Short M, et al. Pilot study: Raman spectroscopy in differentiating premalignant and malignant oral lesions from normal mucosa and benign lesions in humans. *Head Neck* 2015;37(4):511-17
13. Mavarani L, Petersen D, El-Mashtoly SF, et al. Spectral histopathology of colon cancer tissue sections by Raman imaging with 532 nm excitation provides label free annotation of lymphocytes, erythrocytes and proliferating nuclei of cancer cells. *Analyst* 2013;138(14):4035-9
14. Lloyd GR, Wood J, Kendall C, et al. Histological imaging of a human colon polyp sample using Raman spectroscopy and self organising maps. *Vib Spectrosc* 2012;60(0):43-9
15. Patel II, Trevisan J, Evans G, et al. High contrast images of uterine tissue derived using Raman microspectroscopy with the empty modelling approach of multivariate curve resolution-alternating least squares. *Analyst* 2011;136(23):4950-9
16. Beljebbar A, Bouché O, Diebold MD, et al. Identification of Raman spectroscopic markers for the characterization of normal and adenocarcinomatous colonic tissues. *Crit Rev Oncol Hematol* 2009;72(3):255-64
17. Beleites C, Bonifacio A, Codrich D, et al. Raman Spectroscopy and Imaging: Promising Optical Diagnostic Tools in Pediatrics. *Curr Med Chem* 2013;20(17):2176-87
18. Esbensen KH, Geladi P. Principles of Proper Validation: use and abuse of re-sampling for validation. *J Chemometr* 2010;24(3-4):168-87
19. Stone N, Hart Prieto M, Crow P, et al. The use of Raman spectroscopy to provide an estimation of the gross biochemistry associated with urological pathologies. *Anal Bioanal Chem* 2007;387(5):1657-68
- **Interesting article detailing the application of biochemical analysis tools comparing tissue and pure component spectra to quantify the process of bladder and prostate cancer.**
20. Silveira JL, Silveira FL, Bodanese B, et al. Discriminating model for diagnosis of basal cell carcinoma and melanoma in vitro based on the Raman spectra of selected biochemicals. *J BioMed Opt* 2012;17(7):077003
21. Bodanese B, Silveira L Jr, Albertini R, et al. Differentiating normal and basal cell carcinoma human skin tissues in vitro using dispersive Raman spectroscopy: a comparison between principal components analysis and simplified biochemical models. *Photomed Laser Surg* 2010;28(Suppl 1):S119-27
22. Marro M, Nieva C, Sanz-Pamplona R, Sierra A. Molecular monitoring of epithelial-to-mesenchymal transition in breast cancer cells by means of Raman spectroscopy. *Biochim Biophys Acta* 2014;1843(9):1785-95
23. Day JCC, Bennett R, Smith B, et al. A miniature confocal Raman probe for endoscopic use. *Phys Med Biol* 2009;54(23):7077
24. Duraipandian S, Zheng W, Ng J, et al. Simultaneous fingerprint and

- high-wavenumber confocal raman spectroscopy enhances early detection of cervical precancer in vivo. *Anal Chem* 2012; 84(14):5913-19
25. Wood JJ, Kendall C, Hutchings J, et al. Evaluation of a confocal Raman probe for pathological diagnosis during colonoscopy. *Colorectal Dis* 2014;16(9):732-8
26. Short MA, Lam S, McWilliams A, et al. Development and preliminary results of an endoscopic Raman probe for potential in vivo diagnosis of lung cancers. *Opt Lett* 2008;33(7):711-13
27. Short MA, Lam S, McWilliams AM, et al. Using laser Raman spectroscopy to reduce false positives of autofluorescence bronchoscopies: a pilot study. *J Thorac Oncol* 2011;6(7):1206-14
28. Bergholt MS, Zheng W, Ho KY, et al. Fiber-optic confocal raman spectroscopy for real-time in vivo diagnosis of dysplasia in Barrett's esophagus. *Gastroenterology* 2014; 146(1):27-32
- **In vivo study demonstrating the performance of a fiber-optic Raman probe during endoscopy of the upper gastrointestinal tract during a clinical trial.**
29. Bergholt MS, Zheng W, Huang Z. Development of a multiplexing fingerprint and high wavenumber Raman spectroscopy technique for real-time in vivo tissue Raman measurements at endoscopy. *J Biomed Opt* 2013;18(3):030502
30. Taketani A, Hariyani R, Ishigaki M, et al. Raman endoscopy for the in situ investigation of advancing colorectal tumors in live model mice. *Analyst* 2013;138(14): 4183-90
31. Lloyd GR, Almond LM, Stone N, et al. Utilising non-consensus pathology measurements to improve the diagnosis of oesophageal cancer using a Raman spectroscopic probe. *Analyst* 2014;139(2): 381-8
32. Krishna CM, Kurien J, Mathew S, et al. Raman spectroscopy of breast tissues. *Expert Rev Mol Diagn* 2008;8(2):149-66
33. Nieva C, Marro M, Santana-Codina N, et al. The lipid phenotype of breast cancer cells characterized by raman microspectroscopy: towards a stratification of malignancy. *PLoS One* 2012;7(10): e46456
34. Bergner N, Krafft C, Geiger K, et al. Unsupervised unmixing of Raman microspectroscopic images for morphochemical analysis of non-dried brain tumor specimens. *Anal Bioanal Chem* 2012; 403(3):719-25
35. Kast R, Tucker S, Killian K, et al. Emerging technology: applications of Raman spectroscopy for prostate cancer. *Cancer Metastasis Rev* 2014;33(2-3):673-93
36. Dochow S, Beleites C, Henkel T, et al. Quartz microfluidic chip for tumour cell identification by Raman spectroscopy in combination with optical traps. *Anal Bioanal Chem* 2013;405(8):2743-6
37. Hawi SR, Campbell WB, Kajdacsy-Balla A, et al. Characterization of normal and malignant human hepatocytes by Raman microspectroscopy. *Cancer Lett* 1996; 110(1):35-40
38. Taleb I, Thieffin G, Gobinet C, et al. Diagnosis of hepatocellular carcinoma in cirrhotic patients: a proof-of-concept study using serum micro-Raman spectroscopy. *Analyst* 2013;138(14):4006-14
39. Gaggini MCR, Navarro RS, Stefanini AR, et al. Could near-infrared Raman spectroscopy be correlated with the METAVIR scores in liver lesions induced by hepatitis C virus? *Proc. of SPIE, Optical Biopsy XI* 2013;8577:85770F-85779
40. Lui H, Zhao J, McLean D, Zeng H. Real-time Raman Spectroscopy for In Vivo Skin Cancer Diagnosis. *Cancer Res* 2012; 72(10):2491-500
- **Clinical study to improve in vivo diagnosis of skin lesions. Implemented software enables to process the spectra and diagnose the lesion in real time in the patient.**
41. Philipsen PA, Knudsen L, Gniadecka M, et al. Diagnosis of malignant melanoma and basal cell carcinoma by in vivo NIR-FT Raman spectroscopy is independent of skin pigmentation. *Photochem Photobiol Sci* 2013;12(5):770-6
42. Ly E, Durlach A, Antonicelli F, et al. Probing tumor and peritumoral tissues in superficial and nodular basal cell carcinoma using polarized Raman microspectroscopy. *Exp Dermatol* 2010;19(1):68-73
43. Kong K, Rowlands CJ, Varma S, et al. Diagnosis of tumors during tissue-conserving surgery with integrated autofluorescence and Raman scattering microscopy. *Proc Natl Acad Sci USA* 2013; 110(38):15189-94
- **Multimodal approach to diagnose basal cell carcinoma. A significant reduction of measuring time was achieved by combining autofluorescence imaging with Raman spectroscopy.**
44. Vendrell M, Mairi KK, Dhaliwal K, Chang Y-T. Surface-enhanced Raman scattering in cancer detection and imaging. *Trends Biotechnol* 2013;31(4):249-57
45. Matousek P, Stone N. Recent advances in the development of Raman spectroscopy for deep non-invasive medical diagnosis. *J Biophotonics* 2013;6(1):7-19
46. Vogler N, Meyer T, Akimov D, et al. Multimodal imaging to study the morphochemistry of basal cell carcinoma. *Journal of Biophotonics* 2010;3(10-11): 728-36
47. Gao L, Wang Z, Li F, et al. Differential diagnosis of lung carcinoma with coherent anti-stokes raman scattering imaging. *Arch Pathol Lab Med* 2012;136(12):1502-10
48. Meyer T, Bergner N, Bielecki C, et al. Nonlinear microscopy, infrared, and Raman microspectroscopy for brain tumor analysis. *J Biomed opt* 2011;16(2):021113-0
49. Miljković M, Chernenko T, Romeo M, et al. Label-free imaging of human cells: algorithms for image reconstruction of Raman hyperspectral datasets. *Analyst* 2010; 135(8):2002-13
50. Schulze HG, Konorov SO, Piret JM, et al. Label-free imaging of mammalian cell nucleoli by Raman microspectroscopy. *Analyst* 2013;138(12):3416-23
51. McNeish J. Embryonic stem cells in drug discovery. *Nat Rev Drug Discov* 2004;3(1): 70-80
52. Lerou PH, Daley GQ. Therapeutic potential of embryonic stem cells. *Blood Rev* 2005;19(6):321-31
53. Tan Y, Konorov SO, Schulze HG, et al. Comparative study using Raman microspectroscopy reveals spectral signatures of human induced pluripotent cells more closely resemble those from human embryonic stem cells than those from differentiated cells. *Analyst* 2012;137(19): 4509-15
54. Matthäus C, Boydston-White S, Miljković M, et al. Raman and infrared microspectral imaging of mitotic cells. *Appl Spectrosc* 2006;60(1):1-8
55. Huser T, Orme CA, Hollars CW, et al. Raman spectroscopy of DNA packaging in individual human sperm cells distinguishes normal from abnormal cells. *J Biophotonics* 2009;2(5):322-32
56. Konorov SO, Jardon MA, Piret JM, et al. Raman microspectroscopy of live cells under autophagy-inducing conditions. *Analyst* 2012;137(20):4662-8

57. Kourtis N, Tavernarakis N. Autophagy and cell death in model organisms. *Cell Death Differ* 2009;16(1):21-30
58. Kroemer G, Mariño G, Levine B. Autophagy and the integrated stress response. *Mol Cell* 2010;40(2):280-93
59. Dyson OF, Ford PW, Chen D, et al. Raman tweezers provide the fingerprint of cells supporting the late stages of KSHV reactivation. *J Cell Mol Med* 2009;13(8B):1920-32
60. Dochow S, Krafft C, Neugebauer U, et al. Tumour cell identification by means of Raman spectroscopy in combination with optical traps and microfluidic environments. *Lab Chip* 2011;11(8):1484-90
61. Chan JW. Recent advances in laser tweezers Raman spectroscopy (LTRS) for label-free analysis of single cells. *J Biophotonics* 2013; 6(1):36-48
62. Bankapur A, Krishnamurthy RS, Zachariah E, et al. Micro-Raman spectroscopy of silver nanoparticle induced stress on optically-trapped stem cells. *PLoS One* 2012;7(4):e35075
63. Dasgupta R, Verma RS, Ahlawat S, et al. Studies on erythrocytes in malaria infected blood sample with Raman optical tweezers. *J Biomed Opt* 2011;16(7):077009
64. WHO. World health statistics 2014 Part III global health indicators. 2014. Available from: www.who.int/gho/publications/world_health_statistics/EN_WHS2014_Part3.pdf [Last accessed 10 December 2014]
65. WHO. World Health Statistics. 2009. Available from: www.who.int/gho/publications/world_health_statistics/EN_WHS09_Full.pdf [Last accessed 10 December 2014]
66. Asghari-Khiavi M, Vongsivut J, Perepichka I, et al. Interaction of quinoline antimalarial drugs with ferriprotoporphyrin IX, a solid state spectroscopy study. *J Inorg Biochem* 2011;105:1662-9
67. Puskar L, Tuckermann R, Frosch T, et al. Raman acoustic levitation spectroscopy of red blood cells and Plasmodium falciparum trophozoites. *Lab Chip* 2007;7:1125-31
68. Kang JW, Lue N, Kong CR, et al. Combined confocal Raman and quantitative phase microscopy system for biomedical diagnosis. *Biomed Opt Express* 2011;2(9):2484-92
69. Wood B, Bailo E, Asghari Khiavi M, et al. Tip-Enhanced Raman Scattering (TERS) from Hemozoin Crystals within a Sectioned Erythrocyte. *Nano Lett* 2011;11:1868-73
70. Wood B, Hermelink A, Lasch P, et al. Resonance Raman microscopy in combination with partial dark-field microscopy lights up a new path in malaria diagnostics. *Analyst* 2009;134:1119-25
71. Harz M, Kiehnopf M, Stöckel S, et al. Direct analysis of clinical relevant single bacterial cells from cerebrospinal fluid during bacterial meningitis by means of micro-Raman spectroscopy. *J Biophotonics* 2009;2(1-2):70-80
72. Kloß S, Kampe B, Sachse S, et al. Culture independent raman spectroscopic identification of urinary tract infection pathogens: a proof of principle study. *Anal Chem* 2013;85:9610-16
- **Direct identification of pathogens from patient samples within 2 h of collection is significant for fast medical treatment.**
73. Schröder UC, Ramoji A, Glaser U, et al. Combined dielectrophoresis-Raman setup for the classification of pathogens recovered from the urinary tract. *Anal Chem* 2013; 85(22):10717-24
74. Neugebauer U, Trenkmann S, Bocklitz T, et al. Fast differentiation of SIRS and sepsis from blood plasma of ICU patients using Raman spectroscopy. *J Biophotonics* 2014; 7(3-4):232-40
75. Willems-Erix DF, Scholtes-Timmerman MJ, Jachtenberg JW, et al. Optical fingerprinting in bacterial epidemiology: Raman spectroscopy as a real-time typing method. *J Clin Microbiol* 2009;47(3):652-9
76. Willems-Erix D, Bakker-Schut T, Slagboom-Bax F, et al. Rapid typing of extended-spectrum β -lactamase- and carbapenemase-producing *Escherichia coli* and *Klebsiella pneumoniae* isolates by use of SpectraCell RA. *J Clin Microbiol* 2012; 50(4):1370-5
77. Wulf MW, Willems-Erix D, Verduin CM, et al. The use of Raman spectroscopy in the epidemiology of methicillin-resistant *Staphylococcus aureus* of human- and animal-related clonal lineages. *Clin Microbiol Infect* 2012;18(2):147-52
78. Szaszák M, Chang JC, Leng W, et al. Characterizing the intracellular distribution of metabolites in intact *Chlamydia*-infected cells by Raman and two-photon microscopy. *Microbes Infect* 2013;15(6-7):461-9
79. Negri P, Dluhy R. Detection of genetic markers related to high pathogenicity in influenza by SERS. *Analyst* 2013;138(17): 4877-84
80. Negri P, Dluhy R. Ag nanorod based surface-enhanced Raman spectroscopy applied to bioanalytical sensing. *J Biophotonics* 2013;6(1):20-35
81. Reyes-Goddard J, Barr H, Stone N. Surface enhanced Raman scattering of herpes simplex virus in tear film. *Photodiagnosis Photodyn Ther* 2008;5(1):42-9
82. Negri P, Choi J, Jones C, et al. Identification of virulence determinants in influenza viruses. *Anal Chem* 2014;86(14): 6911-17
83. Zoladek A, Pascut FC, Patel P, Notingher I. Non-invasive time-course imaging of apoptotic cells by confocal Raman micro-spectroscopy. *J Raman Spectrosc* 2011;42(3):251-8
84. Buckmaster R, Asphahani F, Thein M, et al. Detection of drug-induced cellular changes using confocal Raman spectroscopy on patterned single-cell biosensors. *Analyst* 2009;134(7):1440-6
85. Pyrgiotakis G, Kundakcioglu OE, Finton K, et al. Cell death discrimination with Raman spectroscopy and support vector machines. *Ann Biomed Eng* 2009;37(7):1464-73
86. Nawaz H, Garcia A, Meade AD, et al. Raman micro spectroscopy study of the interaction of vincristine with A549 cells supported by expression analysis of bcl-2 protein. *Analyst* 2013;138(20): 6177-84
87. Wilson L, Jordan MA. Microtubule dynamics: taking aim at a moving target. *Chem Biol* 1995;2(9):569-73
88. Schie IW, Alber L, Gryshuk AL, Chan JW. Investigating drug induced changes in single, living lymphocytes based on Raman micro-spectroscopy. *Analyst* 2014;139(11): 2726-33
- **Interesting paper about the importance of acquiring imaging data versus single-point measurements due to their heterogeneous structure.**
89. Moritz TJ, Taylor DS, Krol DM, et al. Detection of doxorubicin-induced apoptosis of leukemic T-lymphocytes by laser tweezers Raman spectroscopy. *Biomed Opt Express* 2010;1(4):1138-47
90. Lin D, Lin J, Wu Y, et al. Investigation on the interactions of lymphoma cells with paditaxel by Raman spectroscopy. *Spectroscopy* 2011;25:23-32
91. Hartmann K, Becker-Putsche M, Bocklitz T, et al. A study of Docetaxel-induced effects in MCF-7 cells by means of Raman microspectroscopy. *Anal Bioanal Chem* 2012;403(3):745-53

7 Konferenzbeiträge

Vorträge

- 01/2015 **Abbe School of Photonics Seminar**, Jena, Deutschland
Fatty acid distribution inside macrophages on single cell level using Raman micro-spectroscopy
- 09/2014 **11th Symposium Confocal Raman Imaging**, Ulm, Deutschland
Raman imaging of macrophages – Applications to monitor the uptake of lipids (eingeladen)
- 04/2014 **SPIE Photonics Europe**, Brüssel, Belgien
Imaging of macrophages incubated with deuterated fatty acids using Raman microscopy

Posterpräsentationen

- 04/2016 **Jahrestagung der Deutschen Gesellschaft für Arterioskleroseforschung**, Gießen, Deutschland
Imaging the uptake of lipoproteins by macrophages with Raman micro-spectroscopy
- 07/2015 **ICAVS 8**, Wien, Österreich
Imaging the fatty acid distribution inside macrophages on single cell level by Raman micro-spectroscopy
Förderung durch die Konferenzorganisatoren
- 06/2015 **7th International Graduate Summer School: Biophotonics '15**, Ven, Schweden
Single cell analysis of macrophages to investigate the lipid metabolism using Raman micro-spectroscopy
Förderung durch *ProChance Initiative 2015* der Universität Jena

- 08/2014 **SPEC 2014**, Krakau, Polen
Live cell imaging of macrophages using Raman spectroscopic techniques
- 08/2014 **ICORS**, Jena, Deutschland
Fatty acid distribution inside macrophages on single cell level using Raman micro-spectroscopy
- 04/2014 **SPIE Photonics Europe**, Brüssel, Belgien
Imaging of macrophages incubated with deuterated fatty acids using Raman microscopy
- 03/2014 **Jahrestagung der Deutschen Gesellschaft für Arterioskleroseforschung**,
Gießen, Deutschland
Raman microscopic investigation of lipid metabolism in macrophages
- 10/2013 **FT-IR Spectroscopy in Microbiological and Medical Diagnostics**, Berlin,
Deutschland
Live cell imaging of macrophages incubated with deuterated fatty acids
using Raman microscopy

Danksagung

An dieser Stelle möchte ich mich bei allen bedanken, die mich während der Promotion unterstützt haben. Allen voran gilt mein Dank Prof. Dr. Jürgen Popp für die Betreuung während der Promotion. Ich habe viele Möglichkeiten erhalten auf internationale Konferenzen zu fahren und auch in der Gruppe durch Seminare fachlich und persönlich Verbindungen zu knüpfen. Ein besonderer Dank geht auch an Herrn Prof. Dr. Stefan Lorkowski, der stets bereit war biologische Fragen zu beantworten und immer Zeit für ein Gespräch finden konnte. Dr. Christian Matthäus, danke für die gute Anleitung und Führung während meiner Promotion. Ohne deine unermüdliche Gelassenheit wäre vieles sicher nicht so unbeschwert abgelaufen!

Weiterhin möchte ich mich bei Apl. Prof. Dr. Michael Schmitt, der immer ein offenes Ohr für alle Angelegenheiten hatte, und bei PD Dr. Christoph Krafft, für die Diskussion und Anregungen innerhalb seiner Gruppe, bedanken. Bei Dr. Tobias Meyer bedanke ich mich für die geduldige Justage während der CRS-Messungen. Dr. Maria Wallert und Lisa Schmölz gebührt ein spezieller Dank für die wohl nicht immer einfache Unterstützung einer Physikerin in der Zellkultur. Ohne euch wären die Lipoproteine sicherlich nie oxidiert!

Mein Dank geht an alle Gruppenmitglieder aus der FAG 1.4 am IPHT, der AG Popp und der AG Lorkowski. Vielen Dank für die konstruktive Zusammenarbeit, aber auch für die manchmal nötige Ablenkung auf Weihnachtsmärkten, Winterseminaren und Ähnlichem!

Ganz besonders möchte ich mich bei all meinen Bürokollegen aus der 224 und 223 für das harmonische, hilfsbereite, laute, konstruktive, nervige, witzige, musikalische aber vor allem schöne Zusammenwohnen bedanken. Euch alle aufzuzählen würde leider den Rahmen dieser Seite sprengen. Einen speziellen Dank richte ich aber an meine Büroschwester Katharina, mit der ich von Beginn an alles gemeinsam durchleben durfte.

Liebe Dr. Andreea Radu, Dr. Izabella Jahn und Martin Jahn, danke für die gemeinsame Zeit! Ich hätte da noch ein halbes Sandwich im Rucksack.

Besonderer Dank geht an meine Eltern, die mir immer alle Freiheiten gelassen haben, um meinen eigenen Weg zu planen, und an meine Schwester Katharina mit Jan und Aaron.

Erklärungen

Selbständigkeitserklärung

Ich erkläre, dass ich die vorliegende Arbeit selbständig und unter Verwendung der angegebenen Hilfsmittel, persönlichen Mitteilungen und Quellen angefertigt habe.

Jena, den 05.07.2017

Clara Stiebing

Erklärung zu den Eigenanteilen der Promovendin sowie der weiteren Doktoranden/Doktorandinnen als Koautoren an den Publikationen und Zweitpublikationsrechten bei einer kumulativen Dissertation

Für alle in dieser kumulativen Dissertation verwendeten Manuskripte liegen die notwendigen Genehmigungen der Verlage („Reprint permissions“) für die Zweitpublikation vor. Die Co-Autoren der in dieser kumulativen Dissertation verwendeten Manuskripte sind sowohl über die Nutzung, als auch über die oben angegebenen Eigenanteile der weiteren Doktoranden/Doktorandinnen als Co-Autoren an den Publikationen und Zweitpublikationsrechten bei einer kumulativen Dissertation informiert und stimmen dem zu.

Jena, den 05.07.2017

Clara Stiebing

Einverständniserklärung des Betreuers

Ich bin mit der Abfassung der Dissertation als publikationsbasiert, d.h. kumulativ, einverstanden und bestätige die vorstehenden Angaben. Eine entsprechend begründete Befürwortung mit Angabe des wissenschaftlichen Anteils der Doktorandin an den verwendeten Publikationen werde ich parallel an den Rat der Fakultät der Chemisch-Geowissenschaftlichen Fakultät richten.

Jena, den 05.07.2017

Prof. Dr. Jürgen Popp